WARWICK
THE UNIVERSITY OF WARWICK

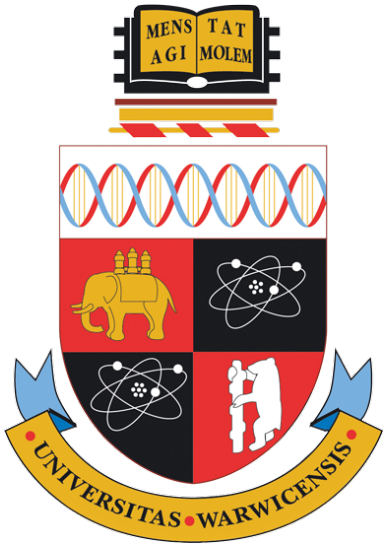

Particle-in-cell simulations of stimulated Raman scattering in the kinetic regime for direct-drive inertial confinement fusion

by

SJ Spencer

Thesis

Submitted to the University of Warwick

in partial fulfilment of the requirements

for admission to the degree of

Doctor of Philosophy

Department of Physics

September 2021

Contents

List of Tables

List of Figures

Declarations

This thesis is submitted to the University of Warwick in support of my application for the degree of Doctor of Philosophy. It has been composed by myself and has not been submitted in any previous application for any degree.

The work presented (including data generated and data analysis) was carried out by the author except in the cases outlined below:

- Figure 6.2 was produced by M. Bailly-Grandvaux (UCSD). It is based on an experiment performed on the LULI laser system by: J. R. Marquès, P. Loiseau, J. Béard, A. Castan, B. Coleman, T. Gangolf, L. Lancia, A. Soloviev, O. Portugall, and J. Fuchs.

Parts of this thesis have been previously published by the author in the following:

- S. J. Spencer, A. G. Seaton, T. Goffrey, and T. D. Arber. Inflationary stimulated Raman scattering in shock-ignition plasmas. *Physics of Plasmas*, 27(12):122705, 2020. doi: 10.1063/5.0022901. URL https://doi.org/10.1063/5.0022901.

The following research was performed in collaboration during the development of this thesis, but does not form part of the thesis:

- A. Higginson, S. Zhang, M. Bailly-Grandvaux, C. McGuffey, K. Bhutwala, B. J. Winjum, J. Strehlow, B. Edghill, M. Dozieres, F. S. Tsung, R. Lee, S. Andrews, S. J. Spencer, N. Lemos, F. Albert, P. King, M. S. Wei, W. B. Mori, M. J.-E Manuel, and F. N. Beg. Electron acceleration at oblique angles via stimulated raman scattering at laser irradiance $> 10^{16}\mathrm{Wcm}^{-2}\mu\mathrm{m}^2$. *Phys. Rev. E*, 103:033203, Mar 2021. doi: 10.1103/PhysRevE.103.033203. URL https://link.aps.org/doi/10.1103/PhysRevE.103.033203
- M. E. Dieckmann, S. J. Spencer, M. Falk, and G. Rowlands. Preferential acceleration of positrons by a filamentation instability between an electron–proton beam and a pair plasma beam. *Physics of Plasmas*, 27(12):122102, 2020. doi: 10.1063/5.0021257. URL https://doi.org/10.1063/5.0021257.

Where figures have been reprinted from other publications, the re-use license appears in Appendix A. ORCID iDs are used to identify collaborators, where their contribution has no associated publication to be referenced.

Abstract

Stimulated Raman scattering (SRS) is a parametric instability of concern to inertial confinement fusion (ICF) schemes; since it scatters light away from the target, and accelerates hot electrons towards the cold fuel. In directly-driven ICF schemes we are concerned with the convective growth of SRS; which can have very large gain in the ICF corona, leading to pump-depletion of the laser ahead of the quarter critical density surface, where it can grow as an absolute instability. Recent shock-ignition experiments [Cristoforetti et al., 2021; Scott et al., 2021], have measured large back-scatter from convective SRS originating from very low plasma densities, where its behaviour is dominated by kinetic effects.

In this thesis we use one-dimensional particle-in-cell simulations to explore convective SRS in three scenarios. First, we consider inflationary SRS (iSRS) in isolation from other coronal laser-plasma instabilities, and study the dependence of the iSRS threshold on the density scale length of the coronal plasma [Spencer et al., 2020]. In the second scenario we study how the inflationary SRS behaviour identified in Spencer et al. [2020] changes when driven by a broadband laser. We model realistic laser and plasma profiles for shock-ignition on Nd : glass and argon fluoride laser systems. The third investigation concerns convective SRS, in both the kinetic and fluid regimes, for magnetised plasmas where it competes with other one-dimensional laser-plasma instabilities such as stimulated Brillouin scattering.

Covid-19 Impact Statement

The University of Warwick advises that "students may choose to submit a Covid-19 impact statement alongside their thesis", and that "Covid-19 statements, not exceeding 600 words, should be submitted to the Doctoral College together with the thesis for examination." https://warwick.ac.uk/services/dc/pgrassessments/covid_impact_statement/ .

The major impact of the Covid-19 pandemic on the preparation of this thesis can be seen in Chapter 5. This project was supposed to use the ARCHER 2 supercomputer, which was planned to be operational from the 6th of May 2020. The computer is still not operational. As a co-investigator on the ARCHER 2 Pioneer Project *Laser-plasma instability simulations in support of the shock-ignition route to inertial fusion*, which was awarded 75 million CPU hours on the new ARCHER 2 system, the plan was for the author to simulate the effect of broadband on inflationary SRS through detailed parameter scans in one dimension, and to investigate particular cases of interest in two dimensions.

In order to be able to complete the thesis on time with the available compute resources, this plan was reduced to investigating the effect of the maximum realistic laser bandwidths on one section of the shock-ignition plasma corona for Nd : glass and Argon Fluoride lasers. The simulations were designed and robustly tested at smaller scales, and with reduced output, to ensure that the simulation campaigns could be completed accurately within the available time and with the available compute. However, there were problems with interpreting the results of the reduced simulations, as can be seen in Section 5.3, since the simulation output was only recorded at the boundaries.

Futhermore, Chapter 6 was supposed to be completed while on placement at UCSD, from January to April 2020. The outbreak of the Covid-19 pandemic in the US and UK in early March 2020 meant that I had to return to the UK and try to complete my part of the project from my parents' home in Gloucestershire. The end of the project was delayed by Covid-19 so far that the post-doc in charge (Adam Higginson) moved to another university in the autumn of 2020, and stopped working on the project.

Acronyms

BAM	Beam-acoustic mode
DBL	Decoupled broadband laser
DT	Deuterium-Tritium
EMW	Electromagnetic wave
EPW	Electron plasma wave
IAW	Ion acoustic wave
ICF	Inertial confinement fusion
iSRS	Inflationary stimulated Raman scattering
LDD	Laser direct-drive
LDI	Langmuir decay instability
LID	Laser indirect-drive
LMJ	Laser Mégajoule
LPI	Laser-plasma interaction
LULI	Laboratoire pour l'Utilisation des Lasers Intenses
NIF	National Ignition Facility
PIC	Particle-in-Cell
SBS	Stimulated Brillouin scattering
SI	Shock ignition
SRS	Stimulated Raman scattering
SSD	Smoothing by spectral dispersion

Chapter 1

Introduction

The material presented in this thesis represents kinetic simulations of laser-plasma interactions (LPI) relevant to direct-drive inertial confinement fusion (ICF). In this introductory chapter, an overview of the goals of, and approaches to, inertial confinement fusion is given; including specific details of the "shock-ignition" (SI) ICF scheme. We then review the previous work concerning laser-plasma interactions in direct-drive ICF, and motivate the use of kinetic modelling throughout this thesis. Finally, we offer an outline of the rest of the thesis.

1.1 Inertial Confinement Fusion

The basic concept of inertial confinement fusion (ICF) is based on the Ulam-Teller design for a thermonuclear weapon (H-bomb), which uses radiation to compress thermonuclear fuel to the point where it undergoes nuclear fusion [Carpintero-Santamaría and Velarde, 2015]. Nuclear fusion is the process by which two light atomic nuclei overcome the electric repulsion between them and combine to form a new, heavier, nucleus and release energy proportional to the mass gap as kinetic energy of the fusion products. The reaction of choice in the thermonuclear weapon, and in most modern ICF designs, is deuterium-tritium (DT) fusion. Equation 1.1 shows the DT reaction; first in the most commonly-presented formula, and then explicitly in terms of the ions and their nucleon (superscript) and proton (subscript) numbers.

$$\begin{aligned} \mathrm{D} + \mathrm{T} &\longrightarrow \mathrm{He}^4 + \mathrm{n} + 17.6\mathrm{MeV} \\ {}^2_1\mathrm{H} + {}^3_1\mathrm{H} &\longrightarrow {}^4_2\mathrm{He}(3.5\mathrm{MeV}) + {}^1_0\mathrm{n}(14.1\mathrm{MeV}). \end{aligned} \tag{1.1}$$

In order for a fusion reaction to be usable on earth, we require that it satisfies certain criteria: uses the lightest possible elements; reaction occurs at "reasonable" temperatures (on the order of 10keV); reactants (fuel) are obtainable. Figure 1.1 shows that the DT reaction has the largest cross section / highest thermal reactivity of the several reactions which satisfy the above conditions.

In a thermonuclear weapon the radiation source is a fission bomb (also known as

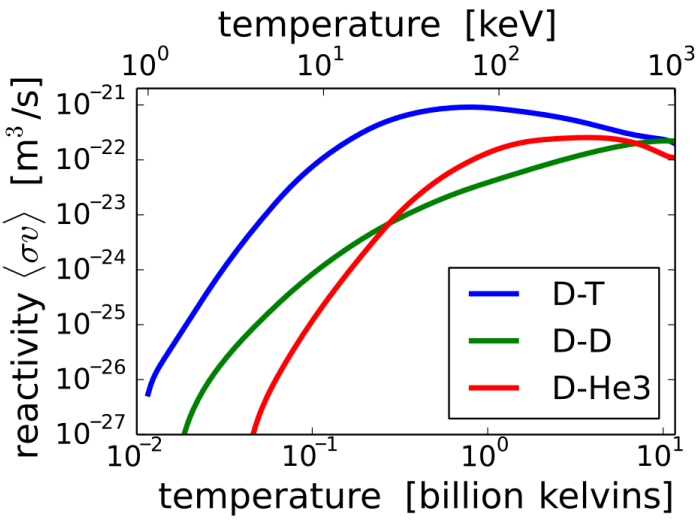

Figure 1.1: Thermal reactivity (product of interaction cross-section and velocity averaged over a Maxwellian) as a function of temperature: for deuterium-tritium, deuterium-deuterium (both interaction branches), and deuterium-helium nuclear reactions. Reprinted from https://commons.wikimedia.org/wiki/File:Fusion_rxnrate.svg under a Creative Commons 2.5 license, via Wikimedia Commons.

an "atom bomb" or "A-bomb"), which detonates and reaches very high temperatures, producing thermal x-rays which are channelled to compress the thermonuclear fuel. The fusion reaction which results from the high density and temperature conditions created in the compressed fuel is unconfined and, therefore, unsuited for energy generation. When lasers were proposed and realised, by Schawlow and Townes [1958] and Maiman [1960] respectively, scientists at Lawrence Livermore National Laboratory realised that lasers had the potential to ignite fusion explosions without using an atomic bomb. In 1972, Nuckolls et al. [1972] published a paper in Nature in which they used the LASNEX computer code to show that high-energy lasers could be used to compress hydrogen to super-high densities. Combined with small target pellets of fusion fuel, which will undergo burn before exploding (due to their inertia), the basic idea of inertial-confinement fusion (ICF) was born. Modern ICF schemes rely on the concept of central hotspot ignition, in which the aim is to ignite fusion reactions at the hot, dense centre of the DT fuel, rather than in the whole fuel capsule at once. The fusion reactions in the central hotspot produce alpha particles which, given a high enough fuel areal density, will heat cold adjacent fuel causing it to fuse.

1.1.1 Direct and indirect drive ICF

Developments to the basic ICF scheme can be categorised by how the laser is used to perform the radiation compression of the fuel. In laser indirect-drive (LID) models, fusion fuel is held inside a hollow chamber made of a high atomic number material.

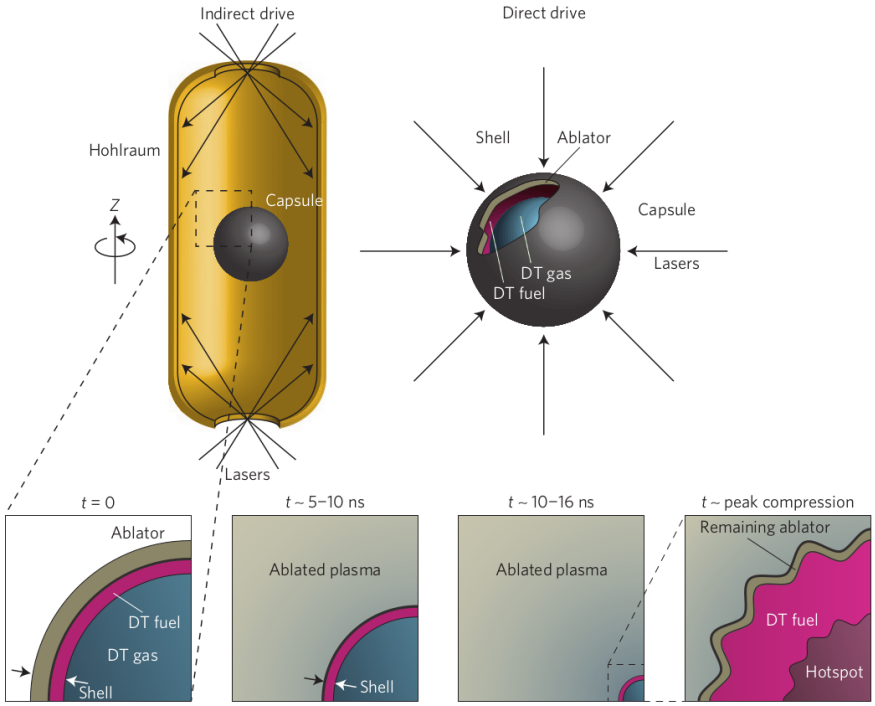

Figure 1.2: **Reprinted with permission from Betti and Hurricane [2016].** Schematics of indirect (top left) and direct-drive (top right) ICF. In both schemes, an ablation plasma is created which drives the implosion by the rocket effect.

This structure is known as the hohlraum, from the German for "hollow space". Lasers are then used to heat the inside walls of the hohlraum until they emit a bath of X-rays which heat the outer layer of the fuel capsule, causing the outer layer of the capsule to ablate and a rocket-effect-like implosion of the inner fuel. An advantage of the indirect-drive technique is that the absorption and re-emission of laser energy by the hohlraum smoothes the radiation which will drive the implosion.

Improvements in laser smoothing technology have made this advantage of LID less obvious, and much research now focuses on laser direct-drive (LDD). In laser direct-drive the laser beams are aimed at the target directly. This allows for a higher conversion efficiency of laser energy to kinetic energy of the imploding fuel; direct-drive ICF couples about five to six times more energy to the fuel than LID [Betti and Hurricane, 2016]. Compared to LID, direct-drive ICF is much more vulnerable to hydrodynamic instabilities, such as the Rayleigh-Taylor instability, which grows from perturbations seeded by inhomogeneous laser illumination. Figure 1.2 is a graphical representation of the indirect- and direct-drive approaches to ICF. This thesis is concerned with energy exchange that happens once the ablated plasma has been created, and while the lasers continue to pass through this ablated plasma towards the DT fuel.

Neither indirect- nor direct-drive inertial confinement fusion has reached the goal of producing more energy than is used to drive the reaction, although the National Ignition Facility (NIF) has recently come close. In late August 2021 (as this thesis was

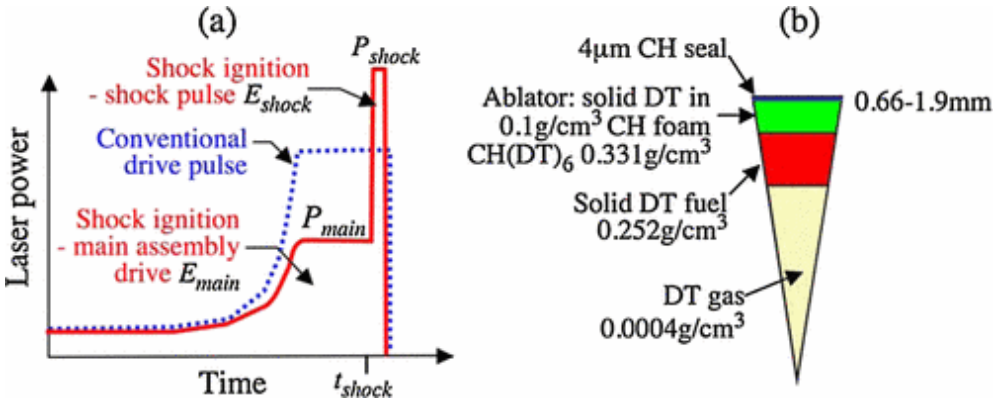

Figure 1.3: **Reprinted with permission from Perkins et al. [2009].** Shock-ignition design for the National Ingition Facility (NIF).

being prepared), it was reported in the international press that 1.3MJ of energy had been produced from fusion, compared to the 1.9MJ of laser energy used to ignite the fuel [Kramer, 2021]. They also reported that thermonuclear burn was achieved: this is the process by which alpha particles produced in the DT fusion reaction heat up the fusion fuel and create more fusion, which creates more heat from alpha particles. These results were produced by indirect-drive ICF, which may not be suitable for power generation. The results have not been peer-reviewed at the time of this thesis.

There have been many proposals for how to improve the performance of direct-drive ICF, each addressing a different issue with the scheme. In this thesis, we consider two avenues: shock-ignition [Betti et al., 2007], which uses low-adiabat low-velocity implosions to reduce Rayleigh-Taylor instabilities; and magnetised ICF, which uses applied magnetic fields to reduce heat loss from the plasma, and to enhance alpha heating in the fuel.

1.1.2 Shock-ignition

Shock-ignition is a directly-driven central ignition scheme boosted by a strong shock. Shock-ignition (SI) separates the fuel assembly/compression from the ignition by using a characteristic laser pulse shape, which can be seen in Figure 1.3. Compared to the conventional drive pulse, the fuel is assembled using a laser drive of low total energy and peak power. This means that the implosion velocity is lower than for conventional drives, which makes the fuel more robust to hydrodynamic instabilities. However, the temperature of the central hotspot is now too low for the fuel to ignite without help. The fuel is ignited by the large high intensity spike at the end of the laser pulse, which drives a strong shock into the target. In a successful shock-ignition experiment, this ignition shock meets the centre of the fuel just as it begins to stagnate and rebound [Perkins et al., 2009], causing it to ignite.

One major disadvantage of the SI approach to ICF is that the laser intensity during the ignition pulse is such that many laser-plasma instabilities will have large gain over

the ablated plasma corona. According to Betti and Hurricane [2016]'s review of inertial confinement fusion "Understanding the laser–plasma interactions at intensities in the 5×10^{15}–10^{16}W/cm^2 range is crucial for assessing the viability of the shock ignition scheme."

1.1.3 Magnetised ICF

Magnetised inertial confinement fusion (also known as magneto-inertial fusion or magnetised-target fusion) is an ICF scheme which uses applied magnetic fields to reduce thermal transport and to enhance alpha heating in the DT fuel [Wurden et al., 2015]. These schemes rely on the "frozen-in-field" assumption from magnetohydrodynamics. In experiments, a magnetic field of the order 10T is embedded in the target and then compressed to many tens of megaGauss (recall 1T = 10^4G) as the DT fuel implodes. Gotchev et al. [2009] demonstrated a magnetised direct-drive platform for the OMEGA laser system, which has an initial (uncompressed) magnetic field of 10T. The first evidence of enhanced ICF performance as a direct result of hot-spot magnetisation came from Chang et al. [2011], who measured an increased fusion yield of 30%. Perkins et al. [2017] suggest that applied magnetic fields of tens of Tesla could also make it easier to reach ignition in LID targets. They find that the optimal applied field would have a magnitude of 50T.

Direct-drive magnetised ICF schemes will still be vulnerable to laser-plasma instabilities in the coronal plasma, but their behaviour will be modified by the magnetic field.

1.2 Laser-plasma instabilities in shock-ignition

In all laser direct-drive ICF schemes, the laser light must travel through the ablated coronal plasma in order to continue to deliver their energy to the target and support the fuel assembly and ignition. Given certain conditions on the laser intensity and the coronal density, temperature, and gradients, the incident laser radiation can transfer some of its energy to plasma waves and scattered light waves. This degrades the uniformity of the laser illumination and reduces the energy delivered to the target. These laser-plasma interactions (LPI) which occur in the coronal plasma are one of the main reasons that the National Ignition Campaign, which took place on the National Ignition Facility (NIF) between 2009 and 2012, failed to achieve ignition [Lindl et al., 2014].

The plasma corona in shock-ignition ICF is characterised by long density scale lengths ($L_n \sim 300 - 1000$µm) and high electron temperatures ($T_e \sim 3 - 6$keV). This wide range of density scale lengths reflects the fact that the shock-ignition design space covers a wide variety of target radii, laser intensities, total laser energies, and pulse lengths. In this section, we provide an overview of the key experiments and simulation

campaigns which have contributed to our understanding of laser-plasma instabilities in shock-ignition.

1.2.1 Experiments

There is little experimental precedent for studying laser plasma interactions at shock-ignition relevant scales. For many years, experiments have been limited to "sub-scale" interactions, which have shorter density scale lengths (defined by $L_n = n_e/(\partial n_e/\partial x)$) and lower plasma temperatures at the quarter critical density surface than those predicted for "ignition-scale" SI. An excellent summary of the laser and plasma parameters used in major shock-ignition experiments, as well as the reported levels of laser-plasma instabilities, can be found in Table I of Seaton and Arber [2020], and we refer the interested reader there. For the purposes of this Introduction, we will summarise two recent shock-ignition experiments, which are not featured in Seaton and Arber [2020]. Further references and summaries, which are relevant to the physics results presented in this thesis, can be found in the introductions of Chapters 4, 5, and 6.

A recent experiment performed by Scott et al. [2021] measured hot electrons from LPI in an ignition scale plasma on the Omega laser facility, for intensities relevant to shock-ignition. In this experiment, the high-intensity ignition pulse interacted with a coronal plasma of peak density scale length 450µm and electron temperature $T_e = 3$keV. They measured SRS from densities in the range $0.04-0.16n_{cr}$, which equates to $k_{\mathrm{EPW}}\lambda_D$ in the range $0.25-0.6$. They measured no SRS or two-plasmon decay (TPD) at the quarter-critical density surface, this suggests that convective SRS below quarter-critical may be more important than has been considered so far. Finally, the measured hot electrons had a relatively flat dependence on intensity, measuring between $35-45$keV and with a total conversion efficiency of $\sim 2.5\%$ [Scott et al., 2021].

Another very recent experiment, by Cristoforetti et al. [2021], measured SRS from a pre-formed, hot ($T_e > 1$keV), and long density scale-length ($275\mu\mathrm{m} < L_n < 450\mu\mathrm{m}$) plasma on the Vulcan laser facility. They found that SRS grew in the strongly kinetic regime and back-scattered between 4% and 20% of the interaction beam energy. Through a combination of coupled-wave and particle-in-cell simulations, they showed that kinetic effects did not contribute to the SRS amplification at the high intensities of the interaction beam ($I_0 > 10^{16}\mathrm{W/cm^2}$), but that they were responsible for large bursts of SRS at intensities close to the inflationary SRS threshold. In agreement with Scott et al. [2021], no SRS or TPD is measured from the quarter-critical density surface. The measured hot-electron temperature ($T_e = 7-12$keV) is fully explained by the very low densities ($n_e < 0.1n_{cr}$) at which SRS grows.

1.2.2 Simulations

Computer simulations were first applied to the then-called "reflective instabilities" (SRS and SBS) by Forslund et al. [1973]. Since then, simulations have been a vital tool for

understanding the role of laser-plasma instabilities in direct-drive ICF. A short and enjoyable historical overview of laser-plasma physics as it relates to ICF can be found in Tikhonchuk [2018].

Laser-plasma interactions can be studied using two main types of codes. The first is codes which solve the coupled envelope equations for various non-linear couplings of waves, such as the Laser-Plasma Simulation Environment [Myatt et al., 2019]. These coupled envelope equations can be adapted to include corrections from kinetic physics, such as the model of Tran et al. [2020] which includes a non-linear frequency shift of the plasma waves due to electron trapping. The second way to approach modelling LPIs relevant to ICF is to use a particle-in-cell (PIC) code, significant examples of which include: EPOCH [Arber et al., 2015]; OSIRIS [Fonseca et al., 2002]; and SMILEI [Derouillat et al., 2018]. For many scientists interested in ICF, the ultimate goal of these LPI simulations is to create "reduced models" of laser-plasma interactions which can be included into hydrodynamic simulations of the full implosion and ignition dynamics.

Two-dimensional PIC simulations of the shock-ignition coronal plasma at ignition-scale have been performed by Seaton and Arber [2020], and compared to 2D "sub-scale" simulations. They find that large convective gains of scattering instabilities below the quarter-critical density surface leads to laser-plasma dynamics controlled by pump depletion. The work presented in this thesis builds on Seaton and Arber [2020]'s analysis by examining, in more detail, the convective SRS which takes place in the shock-ignition plasma corona below quarter-critical; and by looking for mechanisms by which its impact can be mitigated.

This thesis presents simulations which investigate the detailed kinetic physics behind stimulated Raman scattering (a laser-plasma instability of concern to ICF). To this end, we use the particle-in-cell (PIC) code EPOCH. One major advantage that the particle-in-cell method has over the other main family kinetic plasma codes (which are based on direct integration of the Vlasov-Fokker-Planck equation), is that they are significantly cheaper to run for laser-plasma interaction problems. Furthermore, the EPOCH PIC code is developed in-house at the University of Warwick. This allowed us to work closely with the developers when designing simulations and running them on the constantly-changing UK high-performance computing architectures.

One major concern about the use of PIC simulations for laser-plasma interactions in ICF is that they are generally poor at predicting experimental observables, such as the amount of reflected light as a fraction of the incident laser power (known as the reflectivity). This can be attributed to the fact that PIC simulations of LPI are rarely economical to perform in full 3D geometry with realistic laser speckle patterns. Even simulations which are performed in 3D (such as Yin et al. [2009]) are often at "sub-scale" density scale-lengths and temperatures, which dramatically changes the behaviour of the convective instabilities.

1.3 Thesis Outline

In the next five chapters, we present a subset of the work performed by the author in the four years of their PhD registration. Chapters 2 and 3 provide high-level summaries of the relevant theory and methods employed in this work, and contain full references for interested readers.

Chapter 2 We present in Chapter 2 the theory of laser-plasma interactions relevant to coronal plasmas in direct-drive ICF. We start by revising the fluid theory of stimulated Raman scattering (SRS), and quantify its absolute and convective gains. We then discuss how kinetic effects, including large trapped-particle populations, modify the behaviour of SRS.

Chapter 3 Here we present the EPOCH particle-in-cell (PIC) code, which is used to perform all the simulations presented in this thesis, alongside a review of the PIC method for kinetic plasma simulations. Basic benchmarking of the code to the theory presented in Chapter 2 is referenced, and we introduce several key diagnostics which are used throughout the thesis.

Chapter 4 In this work, we use one-dimensional particle-in-cell simulations to show that there is a non-linear frequency shift caused by kinetic effects, resulting in the growth of SRS in an inhomogeneous plasma far exceeding the predictions of fluid theory, so-called inflationary SRS or iSRS. We find that iSRS occurs over a wide range of density scale-lengths relevant to shock-ignition and other directly- driven inertial confinement fusion schemes. Here we quantify the intensity threshold for the onset of iSRS for shock-ignition relevant parameters.

Chapter 5 In this chapter, results of one-dimensional PIC simulations are presented, which represent the first investigation into the practical possibility of using broad-band to suppress inflationary SRS in shock-ignition. We show that for a decoupled broadband laser, the non-linear frequency shift must be taken into account when calculating the condition for suppression of iSRS. Next we consider the effect of bandwidth on iSRS for realistic shock-ignition schemes on two laser systems: frequency-tripled Nd : glass; and Argon Fluoride (ArF).

Chapter 6 In this chapter, we present work performed by the author while employed as a Junior Specialist at the University of California, San Diego between January and April 2020. We present modelling, performed by the author, of an experiment performed at the Laboratoire pour l'Utilisation des Lasers Intenses (France) by J. R. Marquès *et al.*. The experiment showed a small increase in SRS with an applied magnetic field, and this is recreated in our simulations. We then go on to investigate how the effect of the magnetic field depends on $k_{\mathrm{EPW}}\lambda_D$ of the SRS electron plasma wave.

Conventions adopted in the thesis

Unless otherwise stated in the text, all equations and physical quantities in this thesis are in SI units. Standard SI prefixes (k for kilo, T for tera- etc) are used. All numerically-calculated values are given to two significant figures, and written in scientific notation for values greater than 1000, and less than 1/1000.

Chapter 2

Theory

This chapter aims to remind the reader of the tools and methods needed to read, and to engage critically with, the rest of the thesis, and to introduce notation. By the end of this chapter, the reader should be familiar with the following concepts and methods:

1. Backward stimulated Raman scattering (SRS) as a three-wave parametric instability.
2. The difference between convective and absolute SRS, and how we can quantify their gain.
3. The difference between fluid and kinetic SRS, and how we can use $k_{\mathrm{EPW}}\lambda_D$ to delineate these two regimes.
4. The effect of large trapped-particle populations on SRS, including the growth of additional resonant modes.

2.1 Pre-requisites

This section provides a minimal set of pre-requisites I will be assuming in this chapter. We start with Maxwell's equations in differential form:

$$\nabla \times \vec{E} = -\frac{\partial \vec{B}}{\partial t} \qquad \text{(Faraday-Lenz Law)} \tag{2.1a}$$

$$\nabla \times \vec{B} = \mu_0 \vec{j} + \frac{1}{c^2}\frac{\partial \vec{E}}{\partial t} \qquad \text{(Ampere-Maxwell Law)} \tag{2.1b}$$

$$\nabla \cdot \vec{B} = 0 \qquad \text{(No Magnetic Monopoles)} \tag{2.1c}$$

$$\nabla \cdot \vec{E} = \frac{\rho}{\epsilon_0} \qquad \text{(Gauss's Law).} \tag{2.1d}$$

These describe the evolution of the vector fields $[\vec{E}(\vec{x},t), \vec{B}(\vec{x},t)]$ using the mathematical notation $\nabla = \left(\frac{\partial}{\partial x}, \frac{\partial}{\partial y}, \frac{\partial}{\partial z}\right)$ to denote the scalar function divergence $(\nabla\cdot)$ and the vector function curl $(\nabla\times)$. The charge density ρ and current density $\vec{j}$ are most properly calculated by summing the contributions of the exact phase-space coordinates of every

particle in the plasma. However, we can make an approximation and assume that that the phase space is continuous and take an average to get the distribution function $f(\vec{x}, \vec{v}, t)$. Each plasma species has its own distribution function $f_\alpha(\vec{x}, \vec{v}, t)$. We can now define ρ and $\vec{j}$ in terms of the distribution function like so:

$$\rho = \sum_\alpha q_\alpha \int d\vec{v} f_\alpha(\vec{x}, \vec{v}, t) \tag{2.2}$$

$$\vec{j} = \sum_\alpha q_\alpha \int d\vec{v}\vec{v} f_\alpha(\vec{x}, \vec{v}, t). \tag{2.3}$$

In order to close the Maxwell equations, we need an equation which tells us how any distribution function evolves in terms of $[\vec{E}(\vec{x}, t), \vec{B}(\vec{x}, t)]$. Following any course in the kinetic theory of plasmas (for example, Dellar and Schekochihin), and dropping the subscript α on the distribution function, we end up with the Vlasov equation for a collisionless plasma:

$$\frac{\partial f}{\partial t} + \vec{v} \cdot \nabla f + \frac{q}{m}\left(\vec{E} + \frac{\vec{v} \times \vec{B}}{c}\right) \cdot \frac{\partial f}{\partial \vec{v}} = 0 \tag{2.4}$$

By taking moments, with respect to velocity, of the Vlasov equation (and moving to 1D for brevity), we obtain the following reduced description of the plasma in terms of an electron fluid:

$$\frac{\partial n}{\partial t} + \frac{\partial}{\partial x}(nu) = 0 \quad \text{(0th moment: Continuity equation)} \tag{2.5}$$

$$m_e n\left(\frac{\partial u}{\partial t} + u\frac{\partial}{\partial x}u\right) = -\frac{\partial P}{\partial x} + qE_x n \quad \text{(1st moment: Momentum equation)}. \tag{2.6}$$

Where n is the number density (calculated by taking the zeroth moment of the distribution function); u is the macroscopic flow velocity (calculated by taking the first moment of the distribution function); and P is a scalar pressure. In order to close this set of equations, we require an expression for the scalar pressure P that does not introduce any higher moments of the distribution function. Typically in this thesis the timescales are such that thermal conduction can be neglected, and we assume that the process is adiabatic. This means that our final equation takes the form:

$$\frac{d}{dt}\left(\frac{P}{n^\gamma}\right) = 0 \quad \text{(Energy equation)}, \tag{2.7}$$

introducing $\gamma = C_p/C_v = 1 + 2/n = 3$ the ratio of specific heats in one dimension, where n is the number of degrees of freedom. The exception to this adiabatic assumption comes when we consider the ion acoustic wave, in which the electron fluid response is treated as isothermal. When taken together, Equations 2.5, 2.6, and 2.7 are known as

the hydrodynamic equations of motion. For a multi-species plasma, each species will have its own continuity, momentum, and energy equations.

We recall the fundamental time and length scales associated with a plasma: the plasma frequency and the Debye length. The plasma frequency describes the natural frequency of oscillation of electrons in a cold plasma, its expression in terms of the electron number density can be derived by considering the displacement of a block of plasma and considering the restoring forces acting on it, to give:

$$\omega_{pe} = \sqrt{\frac{n_e e^2}{m_e \epsilon_0}}. \tag{2.8}$$

This fundamental time-scale allows us to define a fundamental length-scale based on how far a particle with thermal velocity v_{th} can travel in one oscillation period.

$$\lambda_D = \frac{v_{\text{th}}}{\omega_{pe}} \propto \left(\frac{\text{temperature}}{\text{density}}\right)^{1/2}. \tag{2.9}$$

The thermal velocity is given by:

$$v_{\text{th}} = \sqrt{\frac{k_B T_e}{m_e}}, \tag{2.10}$$

where k_B is the Boltzmann constant. This fundamental length scale is called the Debye length. For a test charge in a plasma, the effect of its electric field is only felt by particles within a sphere of radius λ_D, outside this sphere its electric field is screened out by the other charges in the plasma. For this reason, the Debye length is sometimes called the "screening length".

2.2 Fluid theory of three-wave instabilities

Equipped with this brief revision of the fundamental relationships which describe a plasma, we can now move onto the theory behind our object of study: laser-plasma instabilities.

2.2.1 Dispersion curves and linear modes

Equipped with the hydrodynamic equations of motion (Equations 2.5, 2.6, and 2.7), we now look for normal modes of the system. These describe oscillations in which all variables vary sinusoidally with the same frequency, meaning that they can be written as $A(x,t) = A_1(x)e^{-i\omega t}$. A non-magnetised, thermal, two-species (electron-ion) plasma supports two longitudinal electrostatic modes and one electromagnetic mode. An excellent derivation of these modes can be found in Chapter Three of Jones et al. [1985].

By linearising the electron fluid equations and Maxwell's equations, assuming that ion motion is negligible, and looking for solutions which are harmonic in space and time

$(n_e, P, u_e, E \propto e^{i(kx-\omega t)})$ we can derive the dispersion relation for electron plasma waves (EPWs):

$$\omega^2 = \omega_{pe}^2 + 3k^2 v_{\mathrm{th}}^2. \tag{2.11}$$

Electron plasma waves are also known as "Langmuir waves" after Irving Langmuir, and Equation 2.11 is sometimes called the "Bohm-Gross dispersion relation".

By a similar linear analysis, this time assuming that $T_e \gg T_i$ and that $\omega \ll \omega_{pi}$ (the ion plasma frequency), we find the dispersion relation for ion acoustic waves (IAWs):

$$\omega = c_s k, \tag{2.12}$$

where c_s is the sound speed,

$$c_s = \sqrt{\frac{Z\gamma_e k_B T_e + \gamma_i k_B T_i}{m_i}}. \tag{2.13}$$

Z is the ion charge state, and γ_e, γ_i are the ratio of specific heats for electron and ion fluids, respectively. Typically, we take $\gamma_i = 3$ which corresponds to 1D adiabatic compression of the ions, and $\gamma_e = 1$, corresponding to isothermal compression of the electrons. The requirement that $T_e \gg T_i$ ensures that the IAW does not experience very strong Landau-damping by the ions.

Finally, we consider the problem of a high frequency electromagnetic wave (EMW) travelling in a plasma. The dispersion relation for electromagnetic waves in a plasma is:

$$\omega^2 = \omega_{pe}^2 + c^2 k^2. \tag{2.14}$$

This expression shows that the frequency of EMWs in a plasma is bounded below, in magnitude, by the electron plasma frequency. The limit $\omega_0 = \omega_{pe}$ defines a critical density past which EMWs cannot propagate, since the the electrons can respond in time to shield out the field of the EMW:

$$n_{cr} = \frac{\omega_0^2 m_e \epsilon_0}{e^2}. \tag{2.15}$$

Figure 2.1 shows graphically the dispersion relations for electron plasma waves (EPWs) and electromagnetic waves (EMWs) in a non-magnetised, thermal plasma. The angular frequency of the waves is normalised to the electron plasma frequency, and the wavenumber to the inverse Debye length. The black dashed line $\omega/k = c$ is the dispersion relation for EMW in vacuum, and dashed line $\omega/k = \sqrt{3/2}v_{th}$ is the electron-acoustic wave (EAW) for a population of hot electrons with thermal velocity v_{th}. The frequency of the electron-acoustic wave satisfies $\omega_{pi} < \omega < \omega_{pe}$. The EPW branch and electron acoustic branch actually merge at short wavelengths ($k_{\mathrm{EPW}}\lambda_D \sim 0.53$) [Rose, 2003]. The electron-acoustic wave (EAW) and its cousin the beam-acoustic mode (BAM) will be covered in Section 2.3, where we look at the limits of the hydrodynamic theory and consider some important additions from kinetic theory.

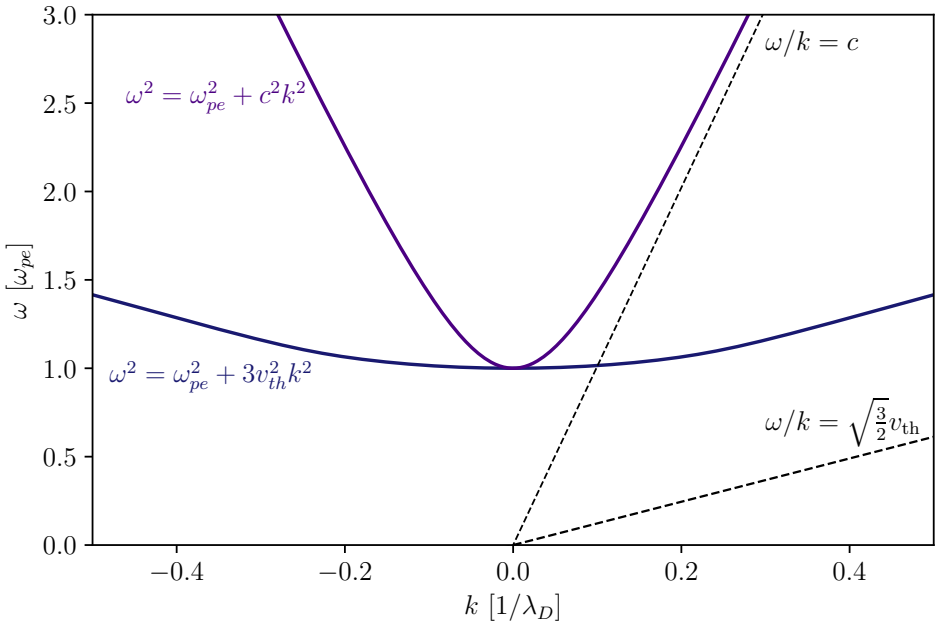

Figure 2.1: Dispersion relations for electromagnetic waves and electron plasma waves in a non-magnetised, hot plasma with $T_e = 5\mathrm{keV}$, $n_e = 0.1n_{cr}$. The limits are chosen such that $k_{\mathrm{EPW}}\lambda_D < 0.5$ for the EPWs, which is required for Equation 2.11 to be valid.

2.2.2 Three-wave instabilities

From linear analysis of the hydrodynamic equations in an un-magnetised plasma (Equations 2.5, 2.6, 2.7) we have recovered three waves: the EPW, IAW, and EMW. Linear analysis in a homogeneous plasma, however, does not tell us anything about how the perturbations associated with one of the waves might affect one or more of the other waves present in the plasma. A second order analysis, which considers contributions proportional to the product of two oscillating quantities, is required to understand how these waves might influence each other. A three-wave instability is the lowest-order example of this non-linear interaction.

An intuitive physical understanding of three-wave instabilities in a plasma driven by a large amplitude laser is given in Figure 2.2. It shows how the laser interacts with an electron plasma wave to generate Thomson-scattered light, which is Doppler-shifted due to the longitudinal collective motion of the electrons in the wave. This new scattered light wave beats with the laser light to create a beat-wave whose envelope reinforces the original EPW via the ponderomotive force, which is proportional to the gradient of the energy density of the beat EMW. Keeping this picture in mind will help to track through the mathematics that is to follow.

As an introduction to the theory of three coupled waves, we start by considering the case of three coupled oscillators, following [Nishikawa, 1968] and [Nishikawa and Liu, 1976]. Setting out the problem in terms of the three waves identified in the previous section, we assume small non-linear coupling, which allows us to say that each of

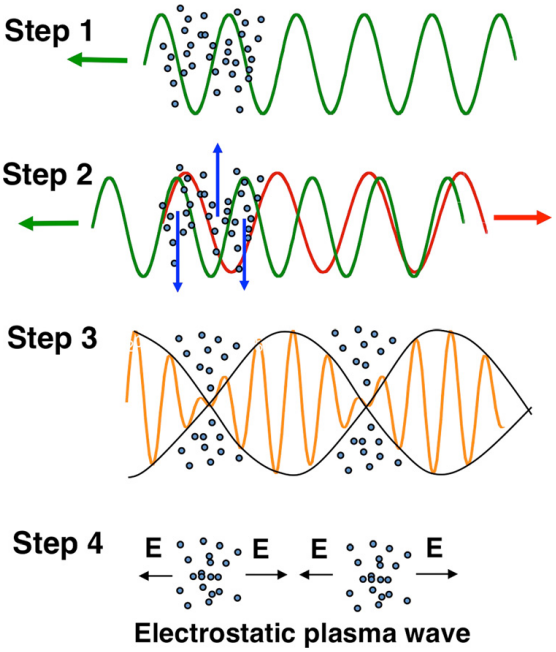

Figure 2.2: **Reprinted with permission from Montgomery [2016].** Graphic depiction of a three-wave instability driven by a large amplitude laser, such as SRS or SBS. The laser travels from right to left, causing electrons in the plasma to oscillate in the laser electric field (Step 1). The oscillating electrons generate a transverse current which generates a scattered light wave (Step 2), which then beats with the original laser wave (Step 3). The ponderomotive force pushes the plasma particles into the troughs of the beat-wave, creating an electrostatic plasma wave (Step 4).

the three waves has angular frequency and wave-number $(\omega, \vec{k})$ which locally satisfy the linear dispersion relations presented in Section 2.2.1. Furthermore, we insist that frequency and wave-number matching are satisfied for the real parts of each:

$$\omega_0 = \omega_1 + \omega_s \tag{2.16a}$$

$$\vec{k_0} = \vec{k_1} + \vec{k_s}. \tag{2.16b}$$

The subscripts $0, 1, s$ are to prepare us for the specific cases of stimulated Raman and Brillouin scattering in which the three waves are: a large-amplitude laser $(\omega_0, \vec{k_0})$; a plasma wave $(\omega_1, \vec{k_1})$; and a scattered light wave $(\omega_s, \vec{k_s})$. Finally, we assume that the plasma is infinite in extent and spatially homogeneous, and that there is no pump depletion. Given these requirements, we make a simplification and model these three waves as three oscillators each satisfying the equation for a damped harmonic oscillator of the form:

$$\left[\frac{d^2}{dt^2} + 2\Gamma_i \frac{d}{dt} + \omega_i^2\right] X_i(t) = 0, \tag{2.17}$$

where ω_i is the characteristic frequency and Γ_i is the constant damping rate of the wave. Since wave 0 (the laser) has large amplitude and is undamped, and we assume no pump

depletion, the lowest order coupling of these waves gives the coupled system:

$$\left[\frac{d^2}{dt^2} + \omega_0^2\right] X_0(t) = 0 \tag{2.18a}$$

$$\left[\frac{d^2}{dt^2} + 2\Gamma_1\frac{d}{dt} + \omega_1^2\right] X_1(t) = 2\alpha X_0(t) X_s(t) \tag{2.18b}$$

$$\left[\frac{d^2}{dt^2} + 2\Gamma_s\frac{d}{dt} + \omega_s^2\right] X_s(t) = 2\beta X_0(t) X_1(t), \tag{2.18c}$$

where α and β are constants that describe the coupling, and satisfy $\alpha\beta \in \mathbb{R}_{>0}$. Equation 2.18 (a) can be solved directly to find:

$$X_0(t) = \bar{X_0}\cos(\omega_0 t). \tag{2.19}$$

Taking the Fourier transform of Equations 2.18 (b) and (c) we get:

$$\left[\omega^2 + 2i\Gamma_1\omega - \omega_1^2\right] X_1(\omega) + \alpha\bar{X_0}\left[X_s(\omega-\omega_0) + X_s(\omega+\omega_0)\right] = 0 \tag{2.20a}$$

$$\left[\omega^2 + 2i\Gamma_s\omega - \omega_s^2\right] X_s(\omega) + \beta\bar{X_0}\left[X_1(\omega-\omega_0) + X_1(\omega+\omega_0)\right] = 0. \tag{2.20b}$$

We now use Equation 2.20 (b) to evaluate $X_s(\omega \pm \omega_0)$ and, since we are looking for solutions for $\omega \simeq \omega_1$, we can ignore the terms in $X_1(\omega \pm 2\omega_0)$. Defining $D_n(\omega) = \omega^2 + 2i\Gamma_n\omega - \omega_n^2$, we find that solutions for ω must satisfy:

$$D_1(\omega) = \alpha\beta{\bar{X_0}}^2\left[\frac{1}{D_s(\omega+\omega_0)} + \frac{1}{D_s(\omega-\omega_0)}\right]. \tag{2.21}$$

We then consider the real and imaginary parts of $\omega = x + i\gamma$ separately and find, for the case where ω_1/ω_0 is far from zero, that the exponential growth rate is given by:

$$(\gamma+\Gamma_1)(\gamma+\Gamma_s)\left[1 + \frac{\Delta\omega^2}{(2\gamma+\Gamma_1+\Gamma_s)^2}\right] = \gamma_0^2. \tag{2.22}$$

Where γ_0 is the coupling constant, given by:

$$\gamma_0 = \frac{\bar{X_0}}{2}\sqrt{\frac{\alpha\beta}{\omega_1\omega_s}}. \tag{2.23}$$

Examining limiting cases of Equation 2.22 gives the following key results for the growth of a three-wave parametric instability in an infinite, homogenous plasma [Nishikawa, 1968]. Firstly, when the frequency mismatch ($\Delta\omega = \omega_0 - (\omega 1 + \omega_s)$) and damping rates of both daughter waves are zero, the instability has maximum growth rate given by the coupling constant γ_0. Secondly, when $\Delta\omega = 0$ but both waves have

finite non-zero damping, the growth rate is given by

$$\gamma = \gamma_0 \sqrt{1 + \left(\frac{\Gamma_s - \Gamma_1}{2\gamma_0} \right)^2} - \frac{\Gamma_1 + \Gamma_s}{2}. \tag{2.24}$$

This means that there is a threshold amplitude, caused by damping, for the pump laser below which the instability cannot grow:

$$I > I_{\text{threshold}} \propto \Gamma_1 \Gamma_s. \tag{2.25}$$

The final comment on this idealised solution is that we assumed $X_1, X_s \ll X_0$ in order to begin solving for ω. However, the analysis presented above shows that X_1, X_s will grow exponentially for $I > I_{\text{threshold}}$, which will soon make this assumption invalid. When we consider more realistic situations such as: pump depletion; finite plasma length; plasma density gradients; things become much more intractable.

Zooming out from the detailed groundwork provided by Nishikawa [1968], we now present the main three-wave instabilities of concern to direct-drive inertial confinement fusion. Table 2.1 shows the interactions in the form: "mother wave → daughter wave 1 + daughter wave 2". In Chapters 4, and 5 we focus entirely SRS. However, in Chapter 6 we also include the effect of mobile ions, and we observe in our simulations stimulated Brillouin scattering and the Langmuir decay instability.

EMW1 → EPW + EMW2	Stimulated Raman Scattering
EMW1 → IAW + EMW2	Stimulated Brillouin Scattering
EMW1 → EPW1 + EPW2	Two-Plasmon Decay
EPW1 → EPW2 + IAW	Langmuir Decay Instability
EMW → EPW + IAW	The Parametric Instability

Table 2.1: Three-wave instabilities in direct-drive ICF. Left column: Quasi-formula, right column: name. Canonical references for each of the instabilities include: SRS [Forslund et al., 1975; Liu et al., 1974]; SBS [Forslund et al., 1975; Liu et al., 1974]; TPD [Liu and Rosenbluth, 1976]; LDI [Karttunen, 1981]; and the parametric instability [Kruer, 1996].

2.2.3 Stimulated Raman scattering

Equipped with a general picture of the three-wave scattering processes driven by a large amplitude laser in a plasma, we now look in detail at stimulated Raman scattering (SRS). Stimulated Raman scattering is a three-wave instability in which a large-amplitude pump wave (the laser) transfers energy to two daughter waves: a scattered light wave and an electron plasma wave. Since the two SRS daughter waves must both have angular frequencies greater than, or equal to, the electron plasma frequency, the frequency-

matching conditions for SRS tell us that SRS can only happen at plasma densities below $n_{cr}/4$. Depending on the laser and plasma conditions, SRS can grow in three ways: absolute SRS; convective fluid SRS; and convective kinetic SRS. In the rest of this section, we cover absolute and convective fluid SRS.

Absolute SRS in a homogeneous plasma

Absolute SRS growth describes the exponential growth of the SRS daughter waves in an infinite homogeneous plasma for a fixed real $\vec{k}$ and complex $\omega = x + i\gamma$. The daughter waves of an absolute instability grow such that *at fixed x, the amplitude grows exponentially in time*. Forslund et al. [1975] outlines three regions of instability for absolute SRS satisfying the matching conditions: $\omega_0 = \omega_s + \omega_{\text{EPW}}$ and $\vec{k_0} = \vec{k_s} + \vec{k}_{\text{EPW}}$. The first is the undamped case with the imaginary part of the SRS EMW frequency satisfying $\gamma \ll \omega_{pe}$, where the growth rate is given by the expression

$$\gamma_0 = \frac{\vec{k}_{\text{EPW}} \cdot \vec{v_{os}}}{2\sqrt{2}} \left[\frac{\omega_{pe}^2}{\omega_{\text{EPW}}(\omega_0 - \omega_{\text{EPW}})} \right]^{1/2}. \tag{2.26}$$

This expression is known as the infinite homogeneous growth rate and it depends on the pump laser intensity via

$$v_{os} = \frac{e}{m_e \omega_0} E_0 = \frac{e}{m_e \omega_0} \sqrt{\frac{2I_0}{c\epsilon_0}}. \tag{2.27}$$

The infinite homogeneous growth rate has its maxima for the case of direct back-scatter, but absolute SRS can also scatter forwards and sideways. In this thesis we are concerned only with backwards SRS, which occurs in one dimension. From this point forward, we will drop the vector notation for the wave-vectors.

The second case considered in Forslund et al. [1975] is the case where $\Delta\omega = 0$ and the daughter waves have non-zero damping and the laser is slightly above the threshold intensity, where the growth rate depends on the damping rates according to Equation 2.24. In this thesis, we will mostly be discussing SRS which arises in PIC codes where the scattered light wave damping can be ignored (since collisional damping is extremely weak at the temperatures considered, and our PIC simulations do not include collisions), and the EPW damping is non-zero. For growth in a homogeneous plasma, with perfect frequency matching, this has growth rate

$$\gamma = \gamma_0 \sqrt{1 + \left(\frac{\Gamma_{\text{EPW}}}{2\gamma_0} \right)^2} - \frac{\Gamma_{\text{EPW}}}{2}, \tag{2.28}$$

which can change as the EPW damping (the Landau damping rate) changes.

Convective growth in a homogeneous plasma

In contrast to the absolute SRS instability, which grows exponentially in time at a fixed x, the convective SRS instability grows exponentially in time in a co-moving frame at the daughter EPW group velocity. This happens in a homogeneous plasma when the electron plasma wave is strongly damped and we seek solutions for a fixed real ω and complex $\vec{k}$.

Convective growth in an inhomogeneous plasma

In an inhomogeneous plasma, such as the shock-ignition plasma corona, backward SRS grows as a convective instability, up to the quarter critical density surface where the growth is absolute. The local dispersion relations for the waves are functions of density; therefore, the wave-number matching term $\kappa(x) = k_0(x) + k_s(x) - k_{\mathrm{EPW}}(x)$ is not constant as the waves amplify through the corona. At the point of perfect resonance $\kappa(x_{\mathrm{res}}) = 0$, but as the daughter waves convect away from this resonant point $\kappa(x > x_{\mathrm{res}}) > 0$. Once $\kappa > 1/2$ we consider the resonance lost.

Unlike in the purely temporal case of the three oscillators (Equation 2.18), we now consider three waves with amplitudes which are functions of both space and time. Following Nishikawa and Liu [1976], each of the three waves can be described by amplitudes satisfying:

$$X_i(x,t) = \tilde{X}_i(x,t)\exp\left[i(k_i x - \omega_i t)\right], \tag{2.29}$$

where the $\tilde{X}_i$ are assumed to be slowly varying in time and space compared to the inverse frequency and inverse wavenumber. Equation 2.29 describes this so-called *envelope approximation*. We also assume that the pump wave is uniform in space. Following a similar analysis to Section 2.2.2, and defining $a_1(x,t)$, $a_2(x,t)$ to be normalised amplitudes of the two daughter waves, we find can define the coupled envelope equations:

$$\left[\frac{\partial}{\partial t} + \Gamma_1 - v_{g,1}\frac{\partial}{\partial x}\right] a_1 = \gamma_0 a_2 \exp\left(i\int^x \kappa(x')dx'\right) \tag{2.30a}$$

$$\left[\frac{\partial}{\partial t} + \Gamma_2 - v_{g,2}\frac{\partial}{\partial x}\right] a_2 = \gamma_0 a_1 \exp\left(i\int^x \kappa(x')dx'\right). \tag{2.30b}$$

$\Gamma_{1,2}$ are the damping rates; $a_{1,2}$ the amplitudes; and $v_{1,2}$ the group velocities of the two daughter waves. The integral term on the right-hand side models the de-phasing of the resonance as the daughter waves convect away from the point of perfect resonance. Considering the zero damping case with $\kappa(x) \propto x$, the famous result of Rosenbluth [1972] finds that the peak intensity of a parametrically unstable mode is given by:

$$I = I_0 \exp\left(2\pi\gamma_0^2/|\kappa' v_{g,1} v_{g,2}|\right). \tag{2.31}$$

In this expression: I_0 is the non-driven, thermal, source intensity; γ_0 is the infinite homogeneous growth rate; κ' is the spatial derivative of the wavenumber mismatch; and $v_{g,1}, v_{g,2}$ are the group velocities of the daughter waves.

A more precise definition of the convective amplification coefficient (a generalisation of the Rosenbluth gain exponent) is given by Williams [1991]. In the WKB approximation, the net growth factor on propagation through the resonant region is

$$\exp\left\{(2\gamma_0^2/\kappa' v_{g,1} v_{g,2})\left[\arccos(G) - G\sqrt{1-G^2}\right]\right\}, \tag{2.32}$$

for $G = \sqrt{\Gamma_1\Gamma_2}/\gamma_0 \geq 1$. This formula reduces to the Rosenbluth formula when either of the two daughter waves is undamped ($G = 0$). Furthermore, when the incident laser intensity is such that the homogeneous convective growth threshold is not reached ($G < 1$), William's growth factor gives no amplification. In all the simulations presented in this thesis, we assume that the back-scattered EMW is has ignorable collisional damping and therefore the growth of SRS is described by the Rosenbluth gain exponent.

Saturation mechanisms

The possible saturation mechanisms for SRS include, but are not limited to: Langmuir decay instability (LDI); wave-breaking; trapped-particle modulation instability (TPMI); nonlinear frequency shift.

2.2.4 Stimulated Brillouin scattering

Stimulated Brillouin scattering SBS is another three-wave parametric instability in which a large-amplitude pump wave (the laser) transfers energy to a scattered light wave and an ion acoustic wave. Since the frequency of ion-acoustic waves is much less than the laser frequency ω_0, almost all of the energy is transferred to the scattered EMW. In this thesis, SBS is important in the very low-density plasmas of Chapter 6, as it causes pump-depletion which reduces the level of SRS.

In the weak-coupling limit, absolute back-scatter SBS has a temporal growth rate of

$$\gamma = \frac{1}{2\sqrt{2}} \frac{k_0 v_{\text{os}} \omega_{pi}}{\sqrt{\omega_0 k_0 c_s}} \tag{2.33}$$

[Forslund et al., 1975]. Where ω_{pi} is the ion plasma frequency, given by:

$$\omega_{pi} = \sqrt{\frac{Z^2 e^2 n_i}{\epsilon_0 m_i}}, \tag{2.34}$$

for Z the ion charge state. For a quasi-neutral plasma ($n_e \simeq Z n_i$), the ion plasma frequency and electron plasma frequency satisfy

$$\omega_{pi} = \sqrt{\frac{Z m_e}{m_i}} \omega_{pe}. \tag{2.35}$$

In an inhomogeneous plasma, SBS occurs as a convective instability below the critical density surface, and can grow absolutely at $n = n_{cr}$.

2.3 Kinetic theory of three-wave instabilities

In the previous section, we considered the non-linear coupling of three waves, each of which locally satisfied dispersion relations derived from fluid theory. In this section, we extend our analysis to consider particles which may be in resonance with the electrostatic waves, and may extract energy from them. These wave-particle effects cannot be derived from the fluid equations, and we must use the Vlasov equation.

2.3.1 Landau damping

Landau damping provides damping for electron plasma waves and ion-acoustic waves. We have seen that the growth of SRS can depend on the damping rates of the two daughter waves. Following Landau [1946], consider the resonant interaction between an electron plasma wave and the electrons of the plasma that supports it. This system is described by the collisionless Vlasov equation and Gauss' Law in 1D:

$$\frac{\partial f}{\partial t} + v\frac{\partial f}{\partial x} = \frac{q}{m}\frac{\partial \phi}{\partial x}\frac{\partial f}{\partial v} \tag{2.36a}$$

$$\frac{\partial^2 \phi}{\partial x^2} = \frac{q}{\epsilon_0}\int dv f, \tag{2.36b}$$

where $f(x, v, t)$ is the electron distribution function and $\phi(x, t)$ is the electric scalar potential which characterises the electric field of the EPW. Landau [1946] solves this system as an initial value problem and looks for solutions to of the form $f(v, t)\exp(ikx)$. We can separate the distribution function into an equilibrium component f_0 and a small perturbation $f_1 \ll f_0$. Moving to k-space and linearising, we get the linearised Vlasov system:

$$\frac{\partial f_1}{\partial t} + ikvf_1 = \frac{q}{m}ik\phi_1\frac{\partial f_0}{\partial v}. \tag{2.37a}$$

$$\phi_1 = \frac{q}{\epsilon_0 k^2}\int dv f_1. \tag{2.37b}$$

Taking Laplace transforms, rearranging, and transforming back, we get the following dispersion relation:

$$\epsilon(\omega, k) = 1 + \frac{\omega_{pe}^2}{n_0 k}\int_{-\infty}^{\infty}\frac{\partial f_0/\partial v}{(\omega - kv)}dv. \tag{2.38}$$

Solutions for the perturbed quantities $\phi_1(t, k), f_1(t, k)$ require integrating expressions with poles which are located at the zeros of $\epsilon(\omega, k)$. Integrating along the Landau

contour, we find that

$$\epsilon(\omega_r, k) = 1 + \frac{\omega_{pe}^2}{n_0 k}\mathcal{P}\int \frac{\partial f_0/\partial v}{(\omega - kv)} - i\pi\frac{\omega_{pe}^2}{n_0 k}\left(\frac{\partial f_0}{\partial v}\right)_{\omega_r/k}. \tag{2.39}$$

Where $\mathcal{P}$ represents the Cauchy principal value of the integral and the imaginary term is the residual at the pole. Setting $\epsilon(\omega, k) = 0$ and equating real and imaginary parts, we find that the imaginary part of ω (the part which represents damping or growth) is:

$$\gamma = \frac{\pi\omega_{pe}^2}{n_0 k}\left(\frac{\partial f_0}{\partial v}\right)_{\omega_r/k}. \tag{2.40}$$

Equation 2.40 is known as the Landau damping rate since, in plasma which is initially Maxwellian, $\partial f_0/\partial v < 0$, leading to damping of the waves.

Further to this, if we also assume the long wavelength limit ($\omega \gg kv$) then we can Taylor expand the denominator of the Cauchy principal value integral and integrate term-by-term. Setting $\epsilon(\omega, k) = 0$, we recover the dispersion relation for electron plasma waves from fluid theory:

$$\omega^2 \simeq \omega_{pe}^2 + 3k^2 v_{th}^2. \tag{2.41}$$

Landau damping is important in all the simulations presented in this thesis, as it provides the damping for all the SRS-driven electron plasma waves. This, in turn, accelerates particles and produces suprathermal electron populations. Furthermore, when the EPWs are strongly Landau damped, stimulated scatterings develop between the laser and other electronic modes. One example of this is stimulated electron acoustic scattering (SEAS) which scatters laser energy from an electrostatic mode with frequency $\omega_{pi} < \omega < \omega_{pe}$, and is associated with strong electron trapping [Montgomery et al., 2001].

2.3.2 Trapping and nonlinear frequency shift

Particles with velocities near the electron plasma wave phase velocity experience a nearly-stationary potential associated with the wave. Such particles can become trapped in the potential well of the EPW, and oscillate with a frequency the depends on the EPW amplitude and wavenumber as:

$$\omega_B = \sqrt{\frac{eEk}{m}}. \tag{2.42}$$

Trapped electrons make two important contributions to the EPW behaviour. After several bounce times ($\tau_B = 2\pi\omega_b$), the Landau damping rate tends towards zero. Furthermore, the frequency shift which arises from trapped particles extracting energy from the wave tends towards a steady-state, negative value. The steady state of the

nonlinear frequency shift depends on the square-root of the EPW amplitude like so:

$$\omega_{NL} = \eta\sqrt{|\tilde{n_e}|}, \tag{2.43}$$

where η is a positive parameter [Morales and O'Neil, 1972].

Both of these results can be explained in terms of the effect of the trapped particles on the distribution function. After several bounce periods, particles trapped in a wave with phase velocity v_{ph} cause a flattened region to emerge which has

$$\left(\frac{\partial f_0}{\partial v}\right)_{v_{ph}} = 0. \tag{2.44}$$

From Equation 2.40, we see immediately that the Landau damping rate becomes zero. Furthermore, inspection of Equation 2.38 shows that the contribution to the real frequency from the region of phase space near the residual is now zero.

2.3.3 Inflationary stimulated Raman scattering

Stimulated Raman scattering (SRS) which takes place in the kinetic regime is often called inflationary SRS (iSRS), and we will use this shorthand throughout the thesis. The name "inflationary SRS" refers to the "inflation" of measures of SRS-activity (such as the reflectivity) above the level predicted by fluid theory, often by many orders of magnitude. The first experimental evidence of this effect can be been in Figure 5 of Montgomery et al. [2002]. The kinetic effect responsible for inflationary SRS depends on whether the coronal plasma is homogeneous (as is generally the case in LID) or inhomogeneous (as in LDD).

For the case of a homogeneous plasma, there are two mechanisms by which inflationary SRS has been shown to occur. The first is that the non-linear reduction in Landau damping of the EPW increases the convective SRS growth rate [Vu et al., 2002]. Furthermore, if the Landau damping rate becomes effectively zero, this can lead to a transition from convective to absolute growth [Wang et al., 2018].

In an inhomogeneous plasma, there are also two explanations for inflationary SRS. For the case in which both daughter waves are initially damped, the theory of Williams [1991] tells us that the inhomogeneous gain increases as the EPW damping decreases (for fixed EMW damping). However, if the EMW is undamped, then the gain is unaffected by the non-linear reduction in EPW Landau damping [Williams, 1991]. In this case, it is the non-linear frequency shift which is responsible for the enhanced SRS growth. The non-linear frequency shift can be such that it cancels out the wave-number detuning caused by propogation up the plasma density gradient; this effect is known as autoresonance [Chapman et al., 2012].

2.3.4 Autoresonance

Autoresonance was proposed as an explanation for inflationary stimulated Raman scattering in an inhomogeneous plasma by Chapman et al. [2010]. As we know, the three-wave interaction is most efficient when frequency and wavenumber matching conditions are satisfied, such that $\omega_0 = \omega_s + \omega_{\mathrm{EPW}}$ and $\vec{k}_0(x) = \vec{k}_s(x) + \vec{k}_{\mathrm{EPW}}(x)$. However, as the SRS electron plasma wave is driven to large amplitude, its frequency undergoes a nonlinear frequency shift which is proportional to the square-root of its amplitude. Unless this effect is cancelled out by some other non-linear effect, the resonance will become de-tuned, leading the SRS instability to saturate. In autoresonant SRS the amplitude of the EPW self-adjusts so that the non-linear frequency shift cancels out the wavenumber mismatch. Figure 2.3 shows the autoresonant growth of an SRS EPW in an EPOCH simulation, performed by the author to benchmark the results of Chapman et al. [2012]. We can see that the density peturbation associated with the EPW amplifies according to the relationship $|\delta n_e/n_e| = \alpha(x - x_r)^2$, where $\alpha = (c_L\kappa'/\eta_n\omega_L)^2$ and c_L, ω_L are the EPW group velocity and frequency, and η_n describes the dependence of the non-linear frequency shift on density.

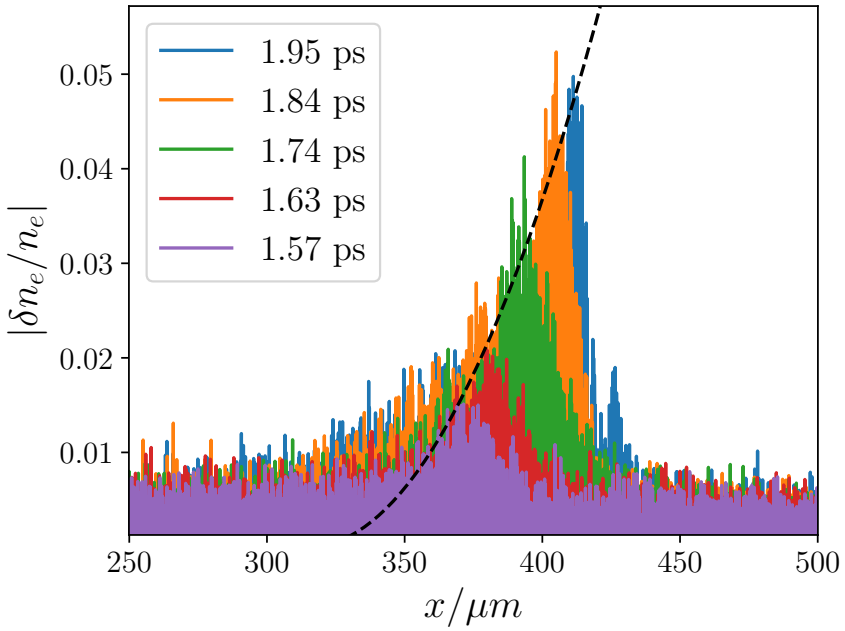

Figure 2.3: Example of autoresonant growth in an EPOCH simulation with parameters: $n_{min} = 0.06 n_{\mathrm{crit}}$; $n_{max} = 0.17 n_{\mathrm{crit}}$; $T_e = 4.5\mathrm{keV}$; nPPC $= 10,000$; $I_0 = 2 \times 10^{15}\mathrm{W/cm^2}$. Black dashed line calculated from the formula in Chapman et al. [2012].

2.4 Laser smoothing techniques

In this thesis, all simulations are performed in one dimension and the laser is modelled as a plane wave. In ICF experiments, various techniques are used to increase the uniformity

of the laser illumination. Figure 2.4 shows the most common two-step process: first the laser is smoothed in space using random phase plates, this breaks up the large-scale spatial phase variations which are present in the laser beam before focussing, into smaller-scale "random" phase variations. These many small beamlets with random phase variation create a speckle pattern at focus (as can be seen in Figure 2.4 (c)). Secondly, the illumination at focus is smoothed in time by varying the speckle intensity pattern using a dispersive optical element which introduces slight angle variations of each wavelength in the laser spectrum Geissel et al. [2016]. This dispersive effect is known as smoothing by spectral dispersion SSD, and was patented by Skupsky et al. [1991]. We consider the effect of this smoothing by spectral dispersion(SSD) in Chapter 5.

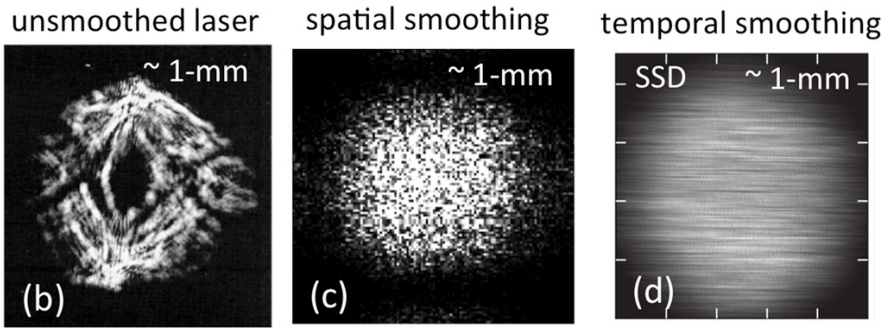

Figure 2.4: **Reprinted with permission from Montgomery [2016]**. Three typical laser focal spots: (b) without smoothing; (c) with spatial smoothing from a random phase plate (RPP); and (d) with RPP and temporal smoothing from 1-D smoothing by spectral dispersion (SSD).

2.5 Final remarks

In this chapter, we presented results from fluid theory, the dispersion relations, the results of considering higher order terms in the fluid or kinetic theory of waves in a plasma, and kinetic effects on the SRS EPW. In the SRS literature referenced in this thesis, there is a significant confusion of language. For example, many papers refer to the "linear theory of SRS", referring to the theory derived from linearising the fluid equations. However, it is clear that since SRS involves a coupling of three waves, it is a non-linear process. From this point on, we will use the phrases "fluid theory of SRS" and "kinetic theory of SRS" to delineate the regimes where SRS is well-described without considering trapped particle effects (often called the linear theory of SRS).

In most cases, the distinction between the fluid and kinetic regimes of SRS behaviour can be made by calculating the product of the local EPW wavenumber and the local Debye length. In the fluid limit, the phase velocity of the EPW is much greater than the thermal velocity ($v_{th}/v_{ph} \ll 1$), and so a vanishingly small percentage of the particles are resonant with the EPW. As the ratio $v_{th}/v_{ph} \simeq k_{\mathrm{EPW}}\lambda_D$ increases, kinetic effects

control the evolution of the EPW. Figure 2.5 shows the how the dominant non-linear effect on the electron plasma wave evolution depends on $k_{\mathrm{EPW}}\lambda_D$. The simulations in this thesis cover a range of $0.1 < k_{\mathrm{EPW}}\lambda_D < 0.41$.

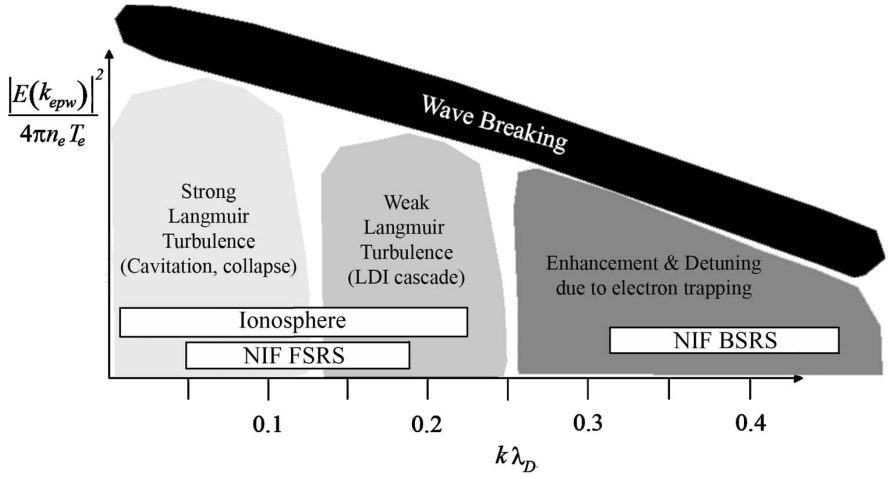

Figure 2.5: **Reprinted with permission from Kline et al. [2006]**. Graphic representation of different non-linear regimes for EPWs as a function of $k_{\mathrm{EPW}}\lambda_D$.

Chapter 3

Methods

Many of the diagnostics presented in this chapter have been adapted from a large repository of LPI diagnostics for EPOCH which was created by Alexander Seaton as part of his PhD project "Particle-in-cell Simulations of Laser-Plasma Instabilities in Shock-Ignition" [Seaton, 2019]. Since Alex left Warwick in September 2019, I have become the main developer and maintainer for the repository.

This chapter introduces the reader to the particle-in-cell code EPOCH, which is used to perform all the simulations presented in this thesis. We also explain the methods used to turn EPOCH's output into diagnostics better-suited to the problem of stimulated Raman scattering in the kinetic regime.

3.1 The particle-in-cell method

The core components of a particle-in-cell (PIC) code are: a fixed spatial grid; finite-sized particles; a solver that moves charged particles according to the Lorentz force law and calculates currents due to this motion (the particle pusher); a solver which uses the calculated currents to solve Maxwell's equations on the grid (the field solver); plus field-to-particle and particle-to-field interpolation routines [Birdsall and Langdon, 1991]. In this section, we cover each of these aspects in turn. Figure 3.1 shows the computational cycle of a typical PIC code, including the optional step of particle collisions, which are not considered in this thesis.

3.1.1 Fixed spatial grid and finite-sized particles

One of the key features of a plasma is that there is a fundamental length scale over which electrostatic fields arising from charge-carriers in the plasma are screened-out: the Debye length. This means that we can make a major simplification in our modelling, and use a spatial grid, rather than resolving fields to arbitray precision. It is not necessary to resolve the Debye length in modern PIC codes, as the particle shape function ensures stability of the algorithm even when the Debye length is under-resolved. However, resolving the Debye length is a strong condition for avoiding numerical self-heating.

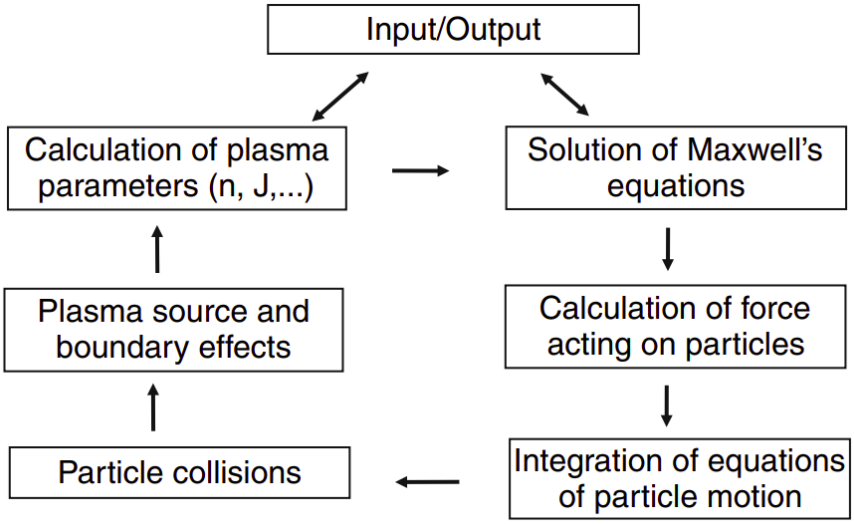

Figure 3.1: **Reprinted with permission from Tskhakaya [2008].**

In practice, the use of higher-order shape functions and field smoothing can keep self-heating at managable levels for even $\Delta x \gg \lambda_D$ [Arber et al., 2015]. Associated with the spatial grid is a temporal grid, the timestep of which is chosen in EPOCH from the Courant–Friedrichs–Lewy condition. For our simulations, which need to resolve the speed of light, this means that $\Delta t \leq c\Delta x$.

There are many more particles in a real plasma than it would be computationally possible to follow through the PIC cycle. As such, PIC codes consider "macro-particles" which each represent many more real particles. The number of particles represented by each macro-particle is called the weight [Arber et al., 2015].

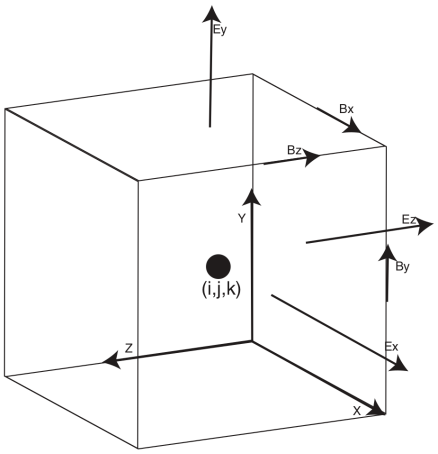

Figure 3.2: **Reprinted from Arber et al. [2015].** Yee staggered grid used for the Maxwell solver in EPOCH.

3.1.2 Field solver

The key point of a PIC simulation is that the system evolves self-consistently, this means that every time the particles move we must calculate the electric and magnetic fields generated by their new current densities. To calculate these new fields we need to solve Maxwell's equations (Equation 2.1). These are differential equations, which means we can solve them using finite-difference methods, in which the full and partial differentials are replaced by difference equations. In EPOCH, the electric and magnetic fields are specified on a Yee staggered grid Yee [1966] (Figure 3.2) and are solved using a finite-difference time-domain (FDTD) re-factoring of the leapfrog method like so: fields are advanced one half time-step from n to $n+1/2$, using the currents from time-step n; then the current is updated by a full time-step by the particle pusher to $\vec{J}_{n+1}$; finally the fields are updated from $n+1/2$ to $n+1$. An advantage of the FDTD method is that all fields are defined at all full and half timesteps.

3.1.3 Particle push

The basic particle pusher acts to integrate the equations of motion for the charged particles and then to accelerate the particles to new velocities, and to translate them to new positions. EPOCH solves the relativistic equation of motion under the Lorentz force, which can be written, for each particle, as a finite difference equation as so:

$$\vec{p}_{n+1} - \vec{p}_n = \Delta t q \left[\vec{E}_{n+\frac{1}{2}} \left(\vec{x}_{n+\frac{1}{2}} \right) + \vec{v}_{n+\frac{1}{2}} \times \vec{B}_{n+\frac{1}{2}} \left(\vec{x}_{n+\frac{1}{2}} \right) \right]. \tag{3.1}$$

Where $\vec{p} = \gamma m v$ is the relativistic particle momentum. This equation can be solved using the Boris algorithm [Boris and Shanny, 1973].

The second equation of motion can be solved using the following integrator:

$$\vec{x}_{n+\frac{3}{2}} - \vec{x}_{1+\frac{1}{2}} = \Delta t \vec{v}_{n+1}. \tag{3.2}$$

Together, these two equations form a second order leapfrog integrator; conventionally understood to be the integrator with the best balance between accuracy, stability and efficiency. The final step of the particle pusher is interpolating from the new particle positions and velocities to new values of the current densities on the grid.

3.1.4 Interpolations

In order to use the field solver and particle pusher together, we need to be able to interpolate between field values defined on the grid, and particle properties defined at the particle locations. For example, the $\vec{E}$ and $\vec{B}$ fields are defined on the staggered grid at cell vertices and cell face-centres, but the particles upon which the fields act can have their centres anywhere in the cell. We therefore require a scheme that will allow us to interpolate from grid quantities to particle quantities and vice versa. Following the excellent summary provided in [Tskhakaya, 2008] for a general PIC code, we associate

with the particles some shape function $S(x_i - X_j)$ where x_i is a grid point onto which the particle is interpolated and X_j is the particle position. As such, the contribution of particle "j" to moments of the distribution function at grid point i can be written

$$A_i^m = a_i^m S(x_i - X_j), \tag{3.3}$$

where m indexes the order of the moment (for example, $A_i^0 = n_i$, $a_i^0 = 1/V$, for V the cell volume).

Figure 3.3 shows the two lowest order shape functions, the nearest grid point (NGP) and linear weightings. In NGP weighting, we count the contribution of particles within one cell width of grid point x_i to the current density, and all particles outside the cell width do not contribute. In linear weighting, we consider the contributions from the two nearest cells, which produces a triangular particle shape

$$S^0(x) = \begin{cases} 1 - |x|/\Delta x, & |x| < \Delta x/2 \\ 0, & \text{otherwise} \end{cases}. \tag{3.4}$$

EPOCH uses the triangle shape function as default.

In EPOCH, the current is not actually calculated from moments of the distribution function, rather it uses Esirkepov's algorithm [Esirkepov, 2001] which always satisfies $\nabla \cdot \vec{E} = \rho/\epsilon_0$, guaranteeing charge conservation.

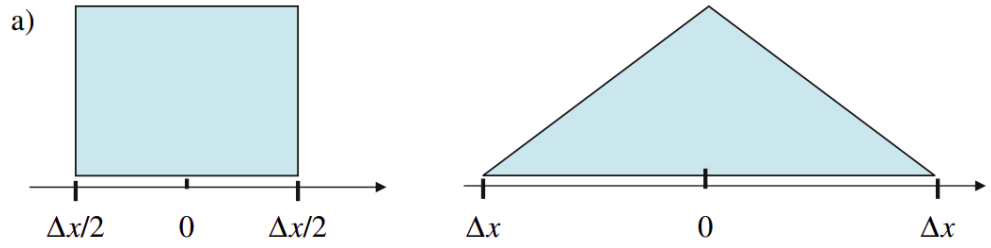

Figure 3.3: **Reprinted with permission from Tskhakaya [2008]**

Interpolation from fields, defined at grid points as $\vec{E}_i, \vec{B}_i$, to particle positions operates in the same manner, using the same shape function as for the current density interpolation.

3.1.5 EPOCH

The EPOCH (Extendable Particle-in-cell Open Collaboration) code is a Birdsall and Langdon type [Birdsall and Langdon, 1991] particle-in-cell (PIC) code developed at the University of Warwick. It is an MPI parallelised, explicit, and relativistic PIC code which is controlled through a customisable input deck [Arber et al., 2015]. The code has over 1,500 registered users, and is one of the standard PIC codes used by plasma physics researchers. As such, the code has been well-tested. Alexander Seaton's doctoral thesis contains very detailed benchmarking of the code against the infinite

homogeneous growth rates for stimulated Raman scattering with and without perfect frequency-matching [Seaton, 2019].

3.2 Diagnostics

The EPOCH code produces outputs in terms of physical variables, for example, electric and magnetic fields as functions of space and time. It can be useful to plot these directly, however it is often more useful to process or transform these outputs before plotting. In this section we cover: frequency-filtered diagnostics; and a method for quantifying the inflation threshold intensity in certain SI coronal plasmas.

3.2.1 Frequency-filtered diagnostics

The core element of several diagnostics used in this thesis is the ability to separate the E_y and B_z fields into different frequency components.

When SRS is measured in experiments, the value reported is the reflectivity: the ratio of SRS-scattered light to incident laser light. For a 351nm laser beam, SRS is typically measured in the 400–700nm band. In order to separate out scattered light from laser light, we use a bandpass filter centred at ω_0. Figure 3.4 shows a typical electromagnetic frequency spectrum for the simulations considered in Chapter 4. The red-shaded band represents the filter bandwidth of $0.3\omega_0$. Following Chapters 14 and 16 of Smith [1997], we construct the bandpass filter by convolving a low-pass and a high-pass filter. Since we want to separate frequencies, we use a windowed sinc filter [Smith, 1997]. A low-pass sinc filter has frequency response given by

$$A(\omega) = \begin{cases} 1 & \omega \leq \omega_c \\ 0 & \omega > \omega_c, \end{cases} \tag{3.5}$$

where ω_c is the cut-off frequency. Taking the inverse Fourier transform of this frequency response gives the filter kernel, which is the sinc function $\sin(x)/x$. In order to use this filter kernel for digital signal processing, it must be truncated so that it has takes non-zero values only on a finite domain. If the truncation is too abrupt, it will introduce large ripples into the passband, meaning that desirable frequencies will not all be passed with their correct amplitude, and ripples in the stop band, meaning that undesirable signals will be unevenly attenuated. For this reason, the filter kernel is convolved with a Hamming window, to recover a smooth frequency response. By combining a low-pass and a high-pass windowed sinc filter, we can design a passband filter which has high stopband attenuation and low passband ripple.

Applying this band-pass filter to the $E_y(x,t)$ and $B_z(x,t)$ signals attenuates all frequencies that are not in the red band in Figure 3.4, leaving only frequencies in the range $0.85\omega_0 \leq \omega_0 \leq 1.15\omega_0$ which represent the transmitted laser light, and light scattered by SBS (which has $\omega_s \simeq \omega_0$). We can define the "near-laser" Poynting flux

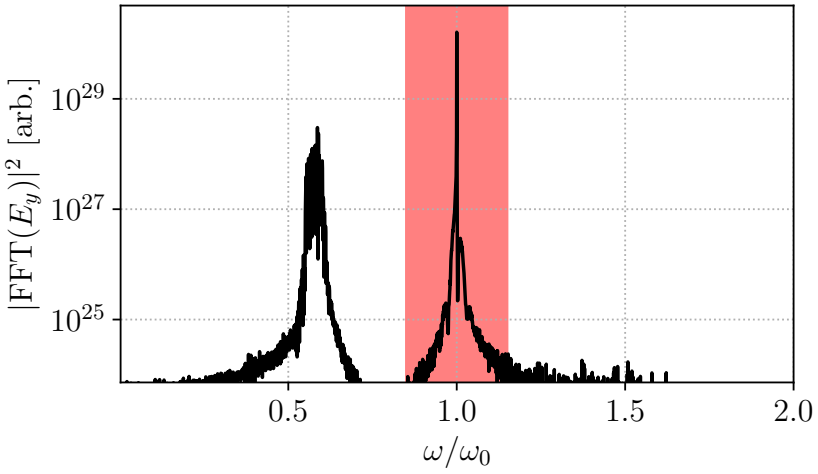

Figure 3.4: Fourier-transform of $E_y(t)$ at laser-entry boundary (back-scattered light exit boundary). Before the application of the bandpass filter, we see two peaks: the peak at 1.0 is the incident laser, and the broader peak around 0.55 is the light scattered by SRS. The red shaded area represents the bandwidth of frequencies that will pass through our filter, with all other frequencies being attenuated.

$L(x,t)$ by calculating the Poynting flux $S(x,t) = E_y B_z/\mu_0$ of these filtered signals. We can also define a "reflected" Poynting flux $R(x,t)$ by subtracting the filtered signals from the original signals, to recover all the light which is not near the laser frequency. We can now construct several other signals like so:

- Transmitted light: $L(x,t)$ averaged over cells close to the right-hand boundary (typically 10 cells in this thesis).
- Backward-SRS scattered light: $R(x,t)$ averaged over cells close to the left-hand boundary.
- Forward-SRS scattered light: $R(x,t)$ averaged over cells close to the right-hand boundary.
- Backward-scattered SBS light: Incident laser power minus $L(x,t)$ averaged over cells close to the left-hand boundary.

Depending on the simulation, one must be careful ascribing these signals to particular three-wave instabilities. For example, in Chapter 6, significant portions of the backward-SRS scattered light undergoes backward-SRS again on its journey towards the left-hand boundary. In such cases, the "rescattered" light may reach the right-hand boundary and get reported as forward-SRS scattered light. In the simulations presented in this thesis, none of the rescattered light reaches any boundary within the simulation time, and so this is not a concern. Furthermore, depending on the plasma density, the filter bandwidth of $0.3\omega_0$ may be too wide and will let-through some of the scattered light

signal. Once again, this is only a concern in Chapter 6 and is avoided by calculating the scattered light frequency from fluid theory and adjusting the filter width accordingly.

3.2.2 Inflation threshold diagnostic

This diagnostic was developed for use in Spencer et al. [2020], in order to quantify an intensity threshold past which SRS is enhanced by several orders of magnitude compared to the predictions of fluid theory.

According to fluid theory, the growth of a parametrically unstable mode in an inhomogeneous plasma is limited by the loss of resonance between the waves as they propagate through the plasma and experience wave-number shift Rosenbluth [1972]. We can formulate this inhomogeneous growth in terms of the Rosenbluth gain exponent

$$G_{\mathrm{Ros}} = 2\pi\gamma_0^2/|v_{g,1}v_{g,2}\kappa'|, \tag{3.6}$$

where γ_0 is the growth rate of the equivalent mode in a homogeneous plasma, $v_{g,1}, v_{g,2}$ are the group speeds of the scattered EM wave/EPW and κ' is the x-derivative of the wave-number mismatch $\kappa(x) = k_0(x) - k_{\mathrm{s}}(x) - k_{\mathrm{EPW}}(x)$ [Rosenbluth, 1972]. The maximum intensity reached by a parametrically unstable wave which has grown from noise at point x is then given by the expression $I_{\mathrm{noise}}\exp(G_{\mathrm{Ros}}(x))$. In order to calculate the intensity of scattered light due to SRS, we substitute for $k_0, k_{\mathrm{s}}, k_{\mathrm{EPW}}$ using the electromagnetic and Bohm-Gross dispersion relations in one dimension, to get:

$$\frac{d\kappa}{dx} = -\frac{1}{2}\frac{q_e^2}{m_e\epsilon_0}\left(\frac{1}{c^2k_0} - \frac{1}{3v_{\mathrm{th}}^2k_{\mathrm{EPW}}} - \frac{1}{c^2k_{\mathrm{s}}}\right)\frac{dn_e}{dx}. \tag{3.7}$$

Substituting this back into G_{Ros} with the growth rate for backward SRS in a homogeneous plasma [Kruer, 2003],

$$\gamma_0 = \frac{k_{\mathrm{EPW}}v_{os}}{4}\left[\frac{\omega_{\mathrm{pe}}^2}{\omega_{\mathrm{EPW}}(\omega_0 - \omega_{\mathrm{EPW}})}\right]^{1/2}, \tag{3.8}$$

gives an appropriate Rosenbluth gain exponent for calculating convective amplification of back-scattered SRS light in our simulations.

We make several simplifying assumptions that allow us to estimate the maximal scattered light intensity at a point in our simulation domain. Firstly, we neglect the dependence of the scattered light velocity on space, and consider it to be fixed at c. This means that we slightly over-estimate the amount of scattered light which is able to reach the point x in time t. We also assume that the laser achieves its maximum intensity starting at $t = 0$ rather than ramping up, as it does in the simulations. We neglect collisional damping of the scattered EM waves and assume that the noise source I_{noise} is homogeneous in the domain. Finally, we assume that the amplification described by the Rosenbluth gain exponent occurs locally and instantaneously at the point of perfect

matching ($\kappa = 0$), rather than across the resonance region defined by $\ell \sim 1/\sqrt{\kappa'}$. For all the simulations presented in this paper $\ell < 6\mu$m. The scattered light intensity is then given by

$$I(x) = \frac{1}{L_x} \int_x^{L_x} I_{\text{noise}} \exp(G_{\text{Ros}}(s)) ds. \tag{3.9}$$

The prefactor $1/L_x$ ensures that if $G_{\text{Ros}} = 0$, such that there is no growth, then the back-scattered signal remains at the the noise intensity. The steady-state intensity of SRS scattered light measured at the laser-entry boundary is then given by $\langle I_{\text{SRS}} \rangle = I(0)$. This model is limited to calculating the maximum reflected light ignoring the effects of pump depletion.

Chapter 4

Inflationary stimulated Raman scattering in shock-ignition plasmas

This chapter is adapted, with the permission of AIP Publishing, from:

- S. J. Spencer, A. G. Seaton, T. Goffrey, and T. D. Arber. Inflationary stimulated Raman scattering in shock-ignition plasmas. *Physics of Plasmas*, 27(12):122705, 2020. doi: 10.1063/5.0022901. URL https://doi.org/10.1063/5.0022901.

In this chapter, results of one-dimensional (1D) particle-in-cell simulations are presented, which show that inflationary SRS (iSRS) can occur in shock-ignition plasmas and which characterise its threshold intensity in terms of the density scale length of the coronal plasma. Inflationary SRS refers to the enhancement of SRS above the levels predicted by fluid theory, caused by kinetic effects. The chapter begins with a review of the previous work on inflationary SRS in homogeneous plasmas, where the effect was first identified and understood. Then the case of iSRS in large-scale inhomogenous plasmas is considered, and a description in terms of autoresonance is presented. The code and initial conditions of the simulation are described, followed by a review of the signatures of iSRS and how they manifest in an inhomogeneous plasma. Finally the dependence of the inflationary SRS threshold intensity on density scale length for shock-ignition parameters, and the saturation of the instability are explored. The conclusion discusses the applicability of these results and ways to increase the experimental relevance of the simulations.

The simulations in this chapter, and in the next two chapters, are greatly simplified compared to the experimental conditions in which inflationary SRS arises. In most SI experiments, the pulse length is on the order of nano-seconds (compared to the sub pico-second timescale of iSRS). Our simulation times vary between one and ten pico-seconds, plenty long enough to resolve the iSRS initial growth and "bursty" nonlinear behaviour, but not long enough to include additional effects from ion dynamics. Furthermore,

our simulations are limited to one spatial dimension, which removes the potential contribution to experiment-scale dynamics of sideways SRS; two-plasmon decay; and spatial detrapping of electrons out of the SRS electron plasma waves.

4.1 Motivation and literature review

4.1.1 Homogeneous plasmas

Inflationary SRS has been studied extensively in the low-density homogeneous plasmas relevant to indirect-drive ICF on the NIF [Ellis et al., 2012; Strozzi et al., 2007; Vu et al., 2002, 2007; Yin et al., 2006, 2008, 2012]. In attempting to explain experimental measurements of large SRS-reflectivities at high values of $k_{\mathrm{EPW}}\lambda_{\mathrm{D}}$ [Fernández et al., 2000; Montgomery et al., 2002], it was suggested that some mechanism caused a reduction in the Landau damping rate by four to five times, compared to the damping for a Maxwellian plasma [Montgomery et al., 2002]. Anomalously large SRS-reflectivities were recreated in simulations [Vu et al., 2001, 2002], and were explained by reference to O'Neil's 1965 model of reduced EPW damping caused by electron-trapping [O'Neil, 1965]. In homogeneous plasmas, iSRS occurs when an SRS EPW grows to a point where it can trap electrons for one complete bounce period or longer, without them becoming de-trapped due to velocity-space diffusion or side-loss [Vu et al., 2002]. This trapped electron population leads to modification of the distribution function, in the form of a locally flattened region around the EPW phase velocity. This translates to a modification of the dielectric properties of the plasma, resulting in a reduction in the EPW's associated Landau damping rate [O'Neil, 1965; Vu et al., 2002], and increased SRS growth.

Key results of previous studies of inflationary SRS in homogeneous plasmas include: a theory for the saturation of iSRS in terms of EPW bowing and the trapped-particle modulation instability [Yin et al., 2008]; the derivation of an inflation threshold intensity in terms of competition between trapping in the EPW and diffusion in velocity space [Vu et al., 2007]; and the description of iSRS in terms of a transition from convective to absolute growth [Wang et al., 2018]. Inflationary SRS has also been identified as an important mechanism in simulations with ensembles of laser speckles [Winjum et al., 2019; Yin et al., 2012].

4.1.2 Inhomogeneous plasmas

In the large-scale inhomogeneous plasmas associated with shock-ignition ($L_n \simeq 300 - 1000\mu$m) the mechanism and effects of inflationary SRS have received much less attention. The few papers which do refer to iSRS in SI inhomogeneous plasmas assume that the explanation of iSRS in a homogeneous plasma in terms of reduced Landau damping also applies to iSRS in an inhomogeneous plasma. However, iSRS in an inhomogeneous plasma actually happens by a different mechanism. In the case of a homogeneous plasma,

reduced Landau damping due to electron-trapping in the EPW leads to an increase of the SRS growth rate which, if sufficiently large, can cause a transition from convective to absolute growth [Wang et al., 2018]. For an inhomogeneous plasma with a linear density profile, where the growth of SRS is always convective, the reduction in Landau damping associated with trapping in the EPW has no net effect on the convective gain unless the daughter EMW is *also* damped [Williams, 1991].

While the local SRS growth rate may depend on the EPW damping rate in an inhomogeneous plasma, the region of SRS convective growth is also extended, leading to a net Rosenbluth gain [Rosenbluth, 1972] which is independent of Landau damping [Liu and Tripathi, 1994; Williams, 1991]. We therefore look to another non-linear effect caused by the trapped electrons in the SRS EPW, the non-linear frequency shift [Morales and O'Neil, 1972]. In an inhomogeneous plasma, the frequency shift resulting from electron-trapping can compensate for the wave-number mismatch on propagating up the density gradient, thereby allowing growth over a larger region - an auto-resonance [Chapman et al., 2010, 2012]. Chapman et al. [2012] proposed this theory for iSRS in an inhomogeneous ($L_n \lesssim 100\mu$m) plasma close to the hohlraum wall in indirect-drive ICF. They demonstrated the auto-resonant interaction between the non-linear frequency shift associated with electron-trapping in EPW and the wave-number mismatch caused by plasma inhomogeneity; which allows larger SRS gain [Chapman et al., 2012].

Inflationary SRS has been suggested as the cause of SRS from low densities in simulations of LPI in shock ignition [Klimo et al., 2014]. Sub-scale shock-ignition experiments have detected SRS scattered light from densities $0.09 - 0.16 n_{\mathrm{cr}}$, where the inflationary mechanism should be important [Cristoforetti et al., 2017]. Recent full-scale ($L_n > 500\mu$m, $T_e = 5$keV) directly-driven experiments have detected significant SRS-reflected light from densities $0.15 - 0.21 n_{\mathrm{cr}}$ [Rosenberg et al., 2020]. Another full-scale ($L_n = 450\mu$m, $T_e = 4.5$keV) SI experiment measured SRS-reflected light from densities between $0.05 - 0.15 n_{\mathrm{cr}}$. Under the conditions of the experiment, $k_{\mathrm{EPW}}\lambda_D$ ranges from $0.3 - 0.6$ and the measured SRS is assumed to be inflationary in origin [Baton et al., 2020]. For a single laser speckle in an inhomogeneous plasma with density scale-length $L_n \simeq 70\mu$m, Riconda et al. [2011] demonstrated that iSRS was associated with electron-trapping in the EPW. By varying $a_0 = eE_0/cm_e\omega_0$ from 0.03 to 0.06, i.e. an increase in laser intensity from 1.0×10^{16}W/cm^2 to 4×10^{16}W/cm^2, they showed a transition to iSRS.

4.2 Code and initial conditions

As described in Chapter 3, all simulations are performed using the EPOCH [Arber et al., 2015] particle-in-cell code. The simulation parameters are chosen to achieve our primary aim of identifying plasma parameters where iSRS may occur; which does not require large simulations of the entire LPI system. The simulations all used a domain size of $L_x = 100\mu$m and ran to $T_{\mathrm{end}} = 2$ps with 2048 particles per cell (PPC)

for the electron species. We treat the ions as a neutralising background population, since we simulate only a two pico-second interval of SRS development, during which ion dynamics will not become important [Rousseaux et al., 2006]. For the plasma parameters laid out above, electron-ion collisions occur on a characteristic timescale of approximately 7ps at the highest density probed, $0.22n_{\mathrm{cr}}$. Since the inflationary Raman process we are investigating takes place on a sub-picosecond timescale, we do not include collisions in our simulations. The plasma density profiles are given by the expression $n(x) = n_{\mathrm{min}}\exp(x/L_n)$ and can be seen in Table 4.1.

$L_n/\mu\mathrm{m}$	$n_{\mathrm{mid}}/n_{\mathrm{cr}}$	$(n_{\mathrm{min}}, n_{\mathrm{max}})/n_{\mathrm{cr}}$	$(k\lambda_{\mathrm{D}_{\mathrm{min}}}, k\lambda_{\mathrm{D}_{\mathrm{max}}})$
300	0.15	$(0.13, 0.18)$	$(0.28, 0.37)$
500	0.12	$(0.11, 0.13)$	$(0.37, 0.41)$
500	0.15	$(0.14, 0.17)$	$(0.29, 0.35)$
500	0.20	$(0.18, 0.22)$	$(0.21, 0.27)$
1000	0.15	$(0.14, 0.16)$	$(0.31, 0.32)$

Table 4.1: Summary of density profiles and $k_{EPW}\lambda_{\mathrm{D}}$ values in each simulation. $L_n = n_e/(dn_e/dx)$ evaluated at n_{mid}. For all but the case centred at $0.2n_{\mathrm{cr}}$, $k_{\mathrm{EPW}}\lambda_{\mathrm{D}} > 0.28$ and we are in the strongly kinetic regime. The total range of $k_{\mathrm{EPW}}\lambda_{\mathrm{D}}$ probed is 0.21-0.41.

We simulate a frequency-tripled Nd:glass laser with vacuum wavelength $\lambda_0 = 351\mathrm{nm}$, polarised in the y-direction. The laser intensity was varied in 20 logarithmically evenly-spaced increments between $10^{14}\mathrm{W/cm}^2$ and $10^{16}\mathrm{W/cm}^2$, with a half-Gaussian temporal profile followed by a flat top, and a rise-time of 50 laser periods. We use absorbing boundaries for the fields and thermal for the particles; these replace any particle leaving the simulation with an incoming particle with velocity consistent with a Maxwellian plasma based on the initial temperature of 4.5keV.

EPOCH uses a pseudorandom number generator (PRNG) to generate the initial particle distribution. Each simulation was repeated 10 times with a different PRNG seed, allowing us to determine the sensitivity of SRS to plasma fluctuations. This allowed us to calculate the mean and standard deviation of the intensity of the light scattered through SRS.

SRS amplifies fluctuations in the plasma, and so is sensitive to number of particles per cell used in the simulation, as can be seen in Figure 4.1. In this figure, the intensity of SRS back-scattered light (denoted in this chapter by $\langle I_{\mathrm{SRS}}\rangle$) is plotted against the incoming laser intensity I_0 ranging between $0.4 - 4.0 \times 10^{15}\mathrm{W/cm}^2$ for a homogeneous plasma with $n_e = 0.15n_{\mathrm{cr}}, T_e = 4.5\mathrm{keV}$, for different numbers of particles per cell. At low incident intensity, $\langle I_{\mathrm{SRS}}\rangle$ is inversely proportional to the number of PPC used. This is as we would expect for the case of simple convective amplification [Rosenbluth, 1972] of the product of two quantities (E_y, B_z) which vary as background PIC noise, which is proportional to $1/\sqrt{\mathrm{PPC}}$. The upper saturated level of $\langle I_{\mathrm{SRS}}\rangle$ is robust to the

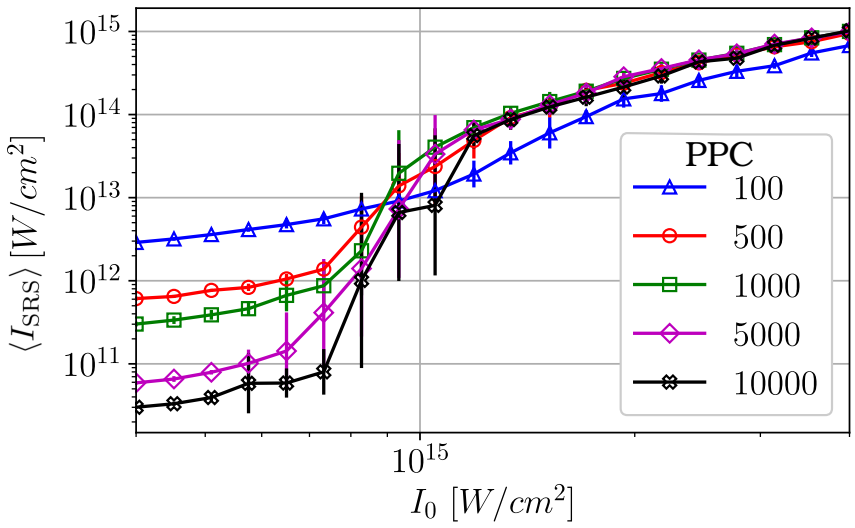

Figure 4.1: Time-averaged intensity of SRS scattered light for a homogeneous simulation ($n_e = 0.15 n_{\mathrm{cr}}$, $T_e = 4.5$keV) with different numbers of particles per cell. Relative errors are given by one standard deviation of the SRS scattered light intensity as calculated from ten simulations.

number of PPC for PPC > 100. The transition between these two levels represents the change from standard convective amplification of SRS to enhanced growth of SRS due to trapping (inflationary SRS), hence we call this the inflation threshold. The existence of an inflation threshold is also robust to the number of particles per cell for PPC > 100.

In the region containing the inflation threshold, the error associated with the intensity of SRS scattered light is largest. This suggests that inflationary SRS is very sensitive to the initial distribution of particles in the simulation domain, and that a statistical analysis of the mean and standard deviation of intensity across different random seeds will be important if we are to determine the iSRS threshold intensity accurately.

4.3 Diagnosing iSRS in inhomogeneous plasmas

If we wish to be sure that the SRS in our simulations is, indeed, inflationary SRS then we should check that it shows signatures which are different from those of fluid convective SRS. Three signatures of inflationary SRS observed in the literature for homogeneous plasmas are: a threshold intensity past which scattering of laser light is enhanced above the level predicted by fluid theory [Vu et al., 2007]; electron-trapping in the SRS EPWs leading to local flattening of the distribution function at the EPW phase velocity [Vu et al., 2002]; and the growth of down-shifted SRS EPWs and a continuum of beam-acoustic modes (BAMs) [Yin et al., 2006]. In what follows we show that all of these signatures are also present for iSRS in an inhomogeneous plasma, despite the instability arising by a different mechanism.

4.3.1 Inflation threshold

We consider first the existence of a threshold intensity past which SRS growth is enhanced, by several orders of magnitude, above the predictions of fluid theory; this has been seen in experiments [Kline et al., 2006] and simulations [Riconda et al., 2011; Vu et al., 2002, 2007; Yin et al., 2006].

In order to identify kinetic inflation of the SRS scattered light intensity in our PIC simulations, we use the simple fluid model presented in Section 3.2.2 to calculate and compare the intensity of SRS scattered light in the absence of kinetic effects. The red circular markers in Figure 4.2 show the results of applying this method to the case of a 500µm density scale-length plasma, with the density profile centred at $0.15n_{\mathrm{cr}}$, for incident laser intensities ranging from $10^{14} - 10^{16}\mathrm{W/cm^2}$. The blue triangular markers show the intensity of SRS scattered light calculated from the equivalent kinetic EPOCH simulations. The relationship between the kinetic and fluid results changes as the incident laser intensity increases. At low intensities the fluid and kinetic models are well matched, but not identical. Continuing this analysis to intensities $< 10^{13}\mathrm{W/cm^2}$ (well below those relevant to shock-ignition) shows that the two methods converge for low intensities, where the behaviour is purely fluid. Once the incident laser intensity exceeds $I_{\mathrm{threshold}} \sim 1.4 \times 10^{15}\mathrm{W/cm^2}$, the intensity of SRS scattered light measured in the kinetic simulations exceeds the fluid prediction by between one and three orders of magnitude, until the intensity reaches $I_0 = 10^{16}\mathrm{W/cm^2}$. In the fluid model, $\langle I_{\mathrm{SRS}} \rangle$ is a smooth function of incident laser intensity and we cannot define such a threshold intensity. This implies that kinetic effects in our simulations are responsible for the increase in $\langle I_{\mathrm{SRS}} \rangle$ and that we have observed iSRS. The fluid estimate shows no sign of saturating at high intensities, since the Rosenbluth gain formula used is based on unbounded linear SRS growth over the resonance region ℓ and the model does not include pump depletion.

By constructing plots such as these, which show the fully kinetic PIC results alongside results from our simple fluid model, we are able to identify the iSRS threshold as the point past which the kinetic and fluid models differ by at least one order of magnitude.

4.3.2 Electron trapping

A second signature of iSRS, as reported in the literature for homogeneous plasmas, is electron-trapping in the SRS electron plasma waves, leading to a non-linear frequency shift and enhanced SRS-reflectivies at large $k\lambda_{\mathrm{D}}$ [Vu et al., 2002]. A typical manifestation of this, for our inhomogeneous simulations, is shown in Figure 4.3. Figure 4.3 shows the instantaneous SRS-reflectivity measured at the left boundary of the simulation domain (a,c), alongside the box-averaged electron distribution function at four times (b,d), for two simulations with laser intensities above and below the iSRS threshold. Sub-figures 4.3 (a,b) show that, when driven below threshold, the distribution of electron momenta is Maxwellian throughout the simulation, and that the maximum instantaneous power

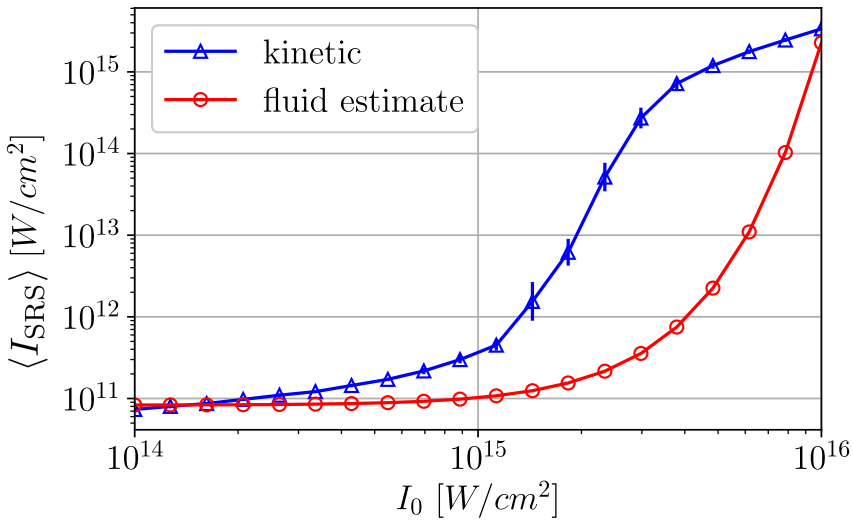

Figure 4.2: Blue triangular markers show the intensity of SRS scattered light calculated using the fully-kinetic EPOCH code for parameters: $L_n = 500\mu\mathrm{m}$ and $n_{\mathrm{mid}} = 0.15 n_{\mathrm{cr}}$. Red circular markers show the intensity of SRS scattered light calculated, for the same plasma parameters, from the fluid model presented above. The initial noise level in the fluid model was calculated from a PIC simulation without the laser driver: $I_{\mathrm{noise}} = \langle E_y B_z \rangle_{x,t} / \mu_0 = 8 \times 10^{10} \mathrm{W/cm^2}$.

in SRS-reflected light is consequently very low ($P \sim 10^{-3} P_0$). In sub-figures (c,d), where the incident laser intensity is well above the iSRS threshold, we see that the power in SRS-reflected light is correlated with the growth of a non-Maxwellian tail in the distribution function, corresponding to an electron population trapped in the SRS electron plasma waves. There is a general trend of increasing SRS-reflected light that correlates with the increasing trapped electron population.

4.3.3 Nonlinear frequency shift

Electron-trapping in the SRS-driven EPW causes a time-dependent non-linear frequency shift of the EPWs [Kline et al., 2006; Morales and O'Neil, 1972], and the growth of a sequence of beam-acoustic modes [Yin et al., 2006]; this is the third signature of iSRS.

Figure 4.4 shows the spatially resolved frequency spectra of EPWs (a,c) and EMWs (b,d) at 0-0.7ps (a,b) and 1.5-1.9ps (c,d). In panels (a,b), the signal maxima sit very close to the white dashed line, which represents the frequencies predicted by the SRS matching-conditions for the original Maxwellian plasma. This means that, at early time, the SRS EPWs and their associated back-scattered light waves are excited at the frequencies matching those of the linear theory without trapping. They are slightly down-shifted from the analytical prediction, which suggests that the trapping becomes important almost immediately in our simulations. At later time, Figure 4.4 (c) shows that the EPW spectrum is down-shifted in frequency at every location in the simulation domain, including to frequencies below the plasma frequency for the original Maxwellian

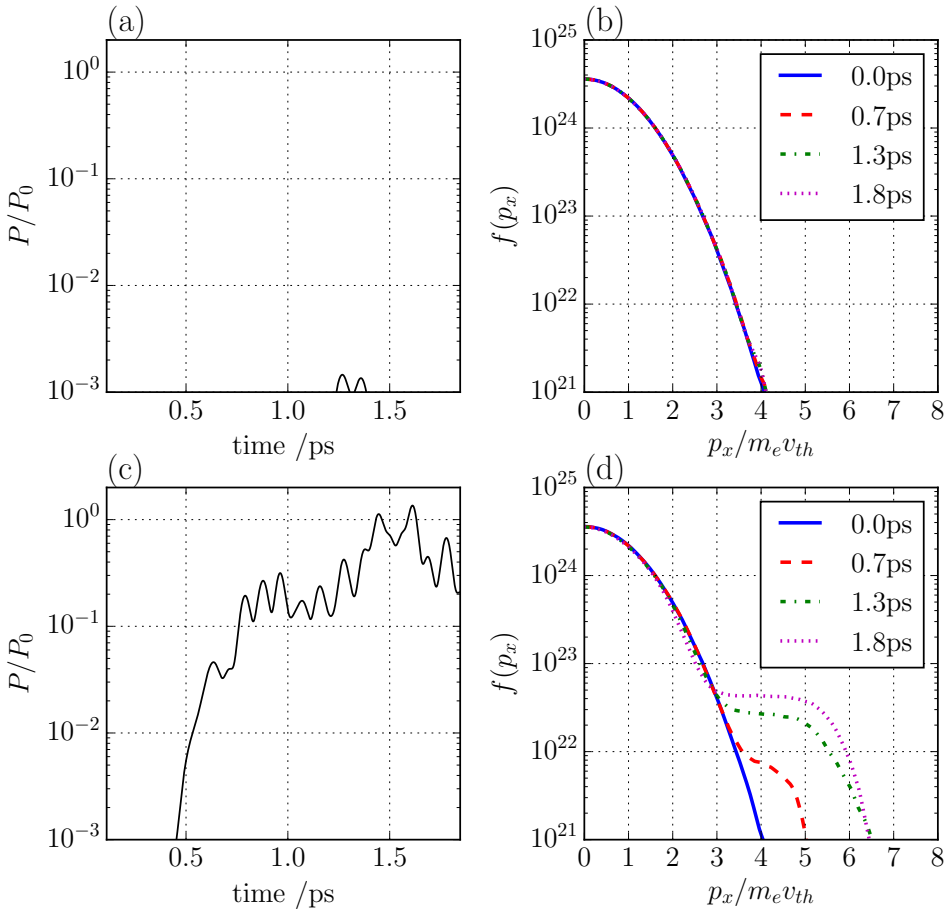

Figure 4.3: Time-resolved comparison of SRS-reflectivity (a,c) and electron distribution functions (b,d) for two simulations with parameters: $L_n = 500\mu$m; centred at $0.15n_{\rm cr}$; and $T_e = 4.5$keV. The distribution function of electron momentum is averaged over the entire spatial domain at four times, normalised to the initial thermal momentum. Panels (a,b) have an incident laser intensity below the threshold for inflationary SRS; $I_0 = 1.13 \times 10^{15}$W/cm^2. Panels (c,d) have an incident laser intensity above the iSRS threshold; $I_0 = 4.83 \times 10^{15}$W/cm^2. For these simulations v_{ph}/v_{th} is in the range 3.59 to 4.02.

plasma (orange solid line). This is evidence of a large trapped particle population removing energy from the wave, causing the frequency of the wave to decrease such that energy is conserved [Morales and O'Neil, 1972]. We also note that in Figure 4.4 (d) the back-scattered light spectrum is up-shifted in frequency space, so as to maintain frequency matching. As well as obvious up-shift of the electromagnetic spectrum, we can also see more general broadening as we move from Figure 4.4 (b) to (d). This could be caused by waves from a higher density propagating to smaller x, so that at a particular location the spectrum covers waves from a range of densities.

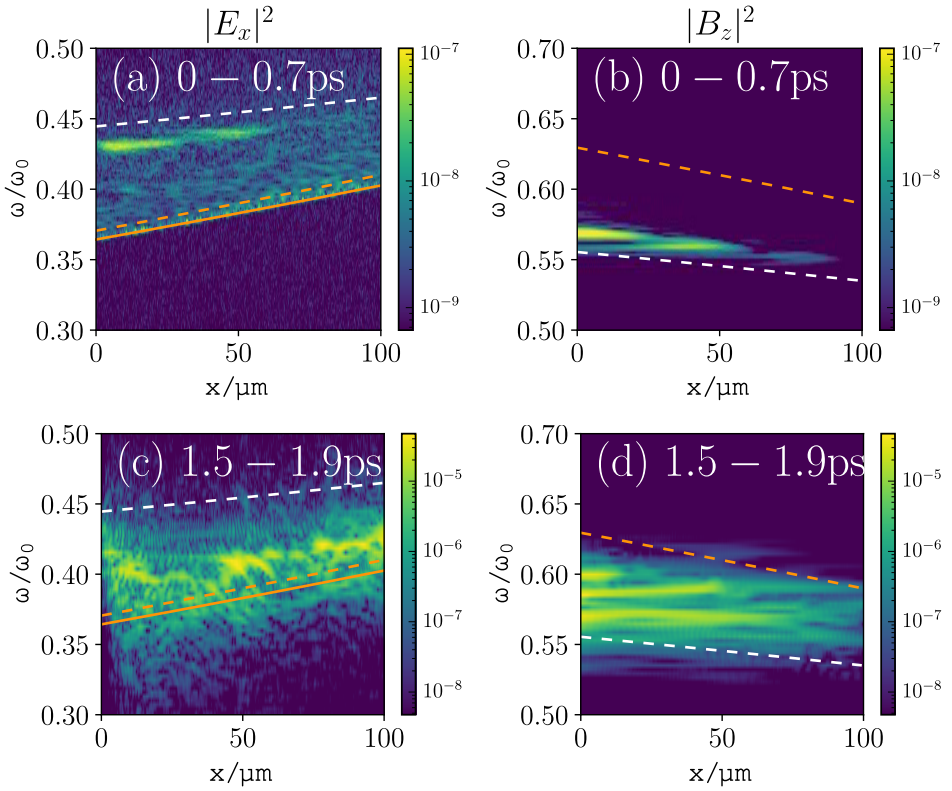

Figure 4.4: Top panels show the spectra of electrostatic (a) and electromagnetic (b) waves over the period $0 - 0.7$ps. The white (orange) dashed lines represent the linear predictions for the spectra of backward (forward) SRS. The bottom panels show the same spectra calculated over the period $1.5 - 1.9$ps. The E_x (B_z) spectrum is significantly down-shifted (up-shifted), demonstrating a trapped population of electrons in the EPW [Yin et al., 2006]. The orange solid line represents the plasma frequency $\omega_{\rm pe}$ for the simulation parameters: $L_n = 500\mu$m centred at $0.15n_{\rm cr}$ and $I_0 = 4.83 \times 10^{15}$W/cm^2.

4.3.4 Beam acoustic modes

Further evidence for a large trapped particle population can be seen in the growth of a beam acoustic mode in the electrostatic (ω, k) spectrum. Figure 4.5 shows the electrostatic dispersion relation from a simulation; it is calculated by taking a 2D Fourier transform of the E_x field over the entire spatial domain, and over two distinct time intervals. At early time, shown in Figure 4.5 (a), electron plasma waves are excited, from background noise, between the two white dashed curves. These represent the Bohm-Gross dispersion relations $\omega^2_{\rm EPW} = \omega^2_{\rm pe} + 3v^2_{\rm th}k^2_{\rm EPW}$ for the highest density in the domain (top line) and the lowest density (bottom line). According to fluid theory, SRS will grow where the Stokes branch, defined by $(\omega - \omega_0)^2 = \omega^2_{\rm pe} + c^2(k - k_0)^2$, intersects with this dispersion curve. This fluid-SRS signal can be seen in Figure 4.5 (a).

The right hand panel of Figure 4.5 shows the EPW dispersion relation calculated from the simulation between $1.2 - 1.9$ps. Inspection of the distribution function in Figure 4.3 shows that, at these times, the distribution function is modified from the

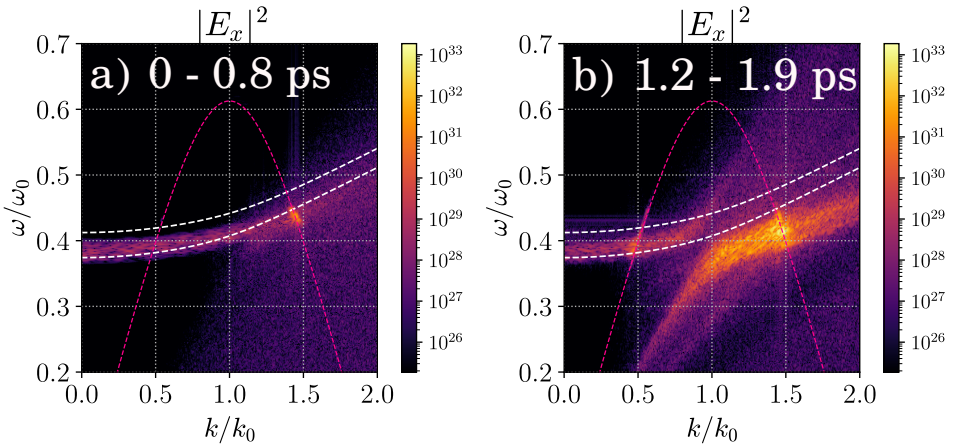

Figure 4.5: (a) 2D FFT of E_x over the period $0 - 0.8$ps. (b) 2D FFT of E_x over the period $1.2 - 1.9$ps. The white dashed lines represent the analytical dispersion relations corresponding to the minimum (bottom line) and maximum (top line) plasma densities, assuming a Maxwellian electron distribution. The pink dashed line shows the Stokes line for down-shifted EM waves. Simulation parameters: $L_n = 500$µm centred at $0.15n_{\text{cr}}$ and $I_0 = 4.83 \times 10^{15}\text{W/cm}^2$.

initial Maxwellian and has a large flattened region, which acts as an effective beam population [Yin et al., 2006]. According to linear theory, this change in the distribution function f changes the kinetic dispersion relation for the electrostatic waves in the system, defined by: $\epsilon(\omega, k) = 1 - \frac{q_e^2}{\epsilon_0 m_e k} \int \frac{\partial f/\partial v}{v - \omega/k} dv = 0$. This change in the dielectric properties of the plasma is realised in the (ω, k) spectrum as a continuum of beam acoustic modes [Yin et al., 2006], this is the large spectral feature in the right hand panel of Figure 4.5 that sits strictly below the Bohm-Gross dispersion curves. These beam acoustic modes are frequency downshifted, recovering the result from Morales and O'Neil's non-linear analysis[Morales and O'Neil, 1972]. The maximum of the BAM signal at $k \sim 1.5k_0$ is the intersection of the BAM with the Stokes branch, the new location of SRS growth.

We can also see in Figure 4.5 (b) a signal at $k \sim 0.5k_0$ which sits on the intersection of the Stokes branch with the range of EPWs satisfying the Bohm-Gross dispersion relations. This represents forward-scattered SRS EPWs, which have not undergone a significant frequency shift. For all the simulations presented in this paper, when driven above threshold, the power in forward SRS scattered light is of the order $P \sim 10^{-3}P_0$ or lower, and is therefore energetically unimportant.

4.4 Intensity threshold and hot electron scaling

Using the method developed in Section 4.3 for locating the inflation threshold, and the analysis of electron trapping and downshifted EPWs to ensure that the SRS observed is inflationary in origin, we investigate how iSRS depends on various plasma parameters

relevant to shock-ignition. Using the PIC simulation set-up as in Section 4.2 (with the same simulation domains, plasma densities, and temperatures), we varied the plasma density scale-length across the range of values predicted for shock-ignition (300µm – 1000µm) [Ribeyre et al., 2009]. As well as varying the density scale-length, we also centred the density profiles at different values of density. Figure 4.6 shows the result of this parameter scan.

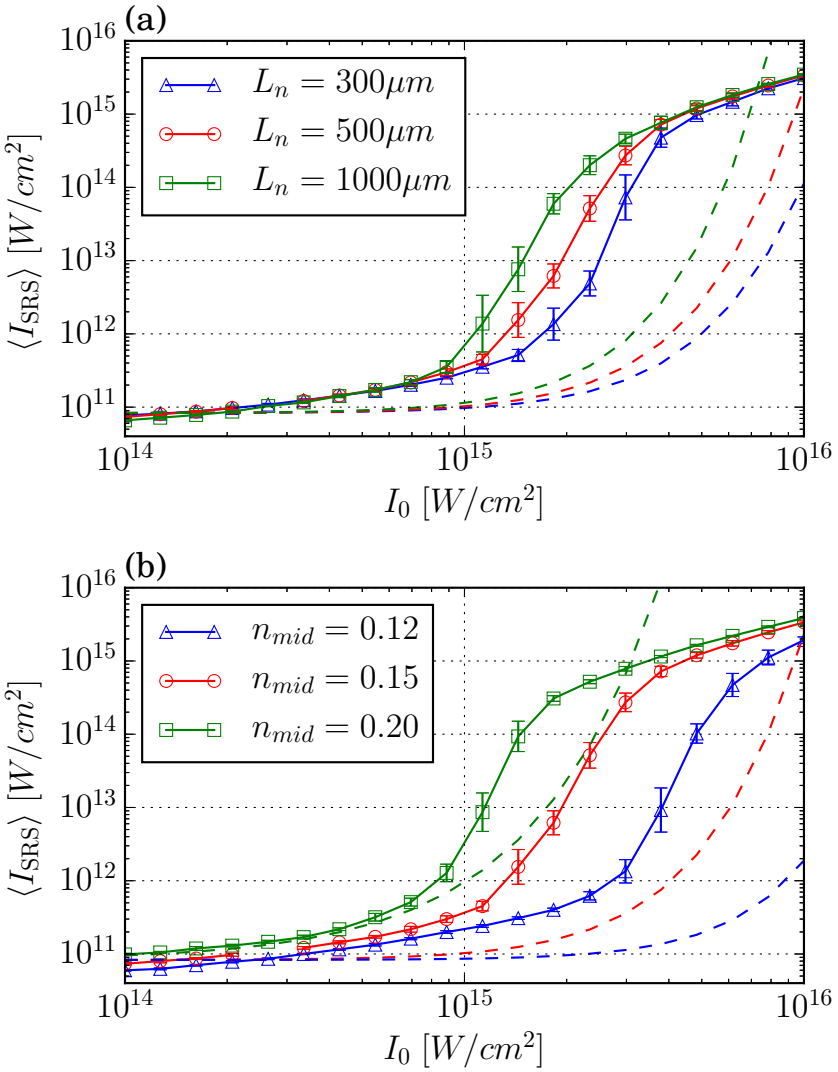

Figure 4.6: (a) Relationship between incident laser intensity and the intensity of SRS scattered light for three different density scale-lengths, with plasma density profiles centred at $0.15n_{cr}$. (b) Relationship between incident laser intensity and the intensity of SRS scattered light for three simulations with $L_n = 500$µm centred at three different densities. Each coloured dashed line represents the prediction of the fluid model presented in Section 4.3 for the same parameters as the solid line of the same colour.

From Figure 4.6 (a) we see that as the density scale-length of the SI coronal plasma decreases, the intensity threshold for iSRS increases. Vu et al. [2007] derived a condition

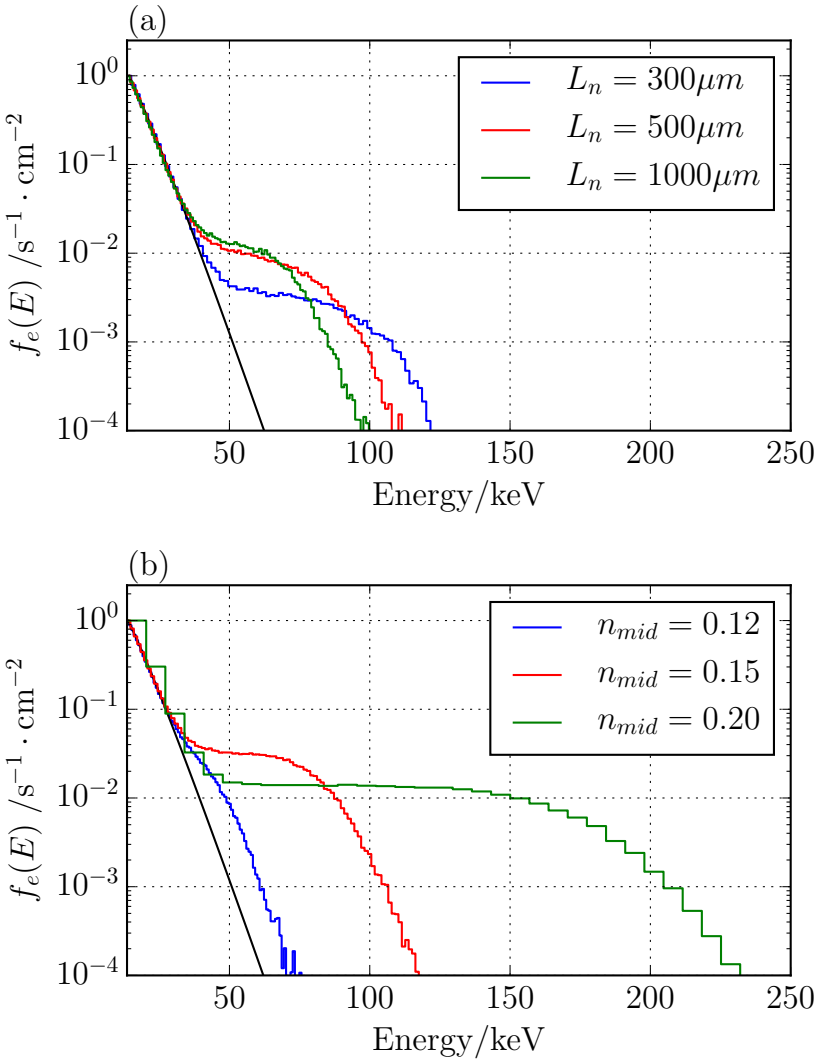

Figure 4.7: (a) Hot electron flux through the right boundary in three simulations with parameters: $I_0 = 2.98 \times 10^{15}$W/cm^2; $n_{\text{mid}} = 0.15 n_{\text{cr}}$; $L_n = 300, 500$,1000µm. (b) Hot electron flux through the right boundary in three simulations with parameters: $I_0 = 6.16 \times 10^{15}$W/cm^2; $L_n = 500$µm; $n_{\text{mid}} = 0.12, 0.15, 0.20 n_{\text{cr}}$ respectively. Each distribution is normalised to its maximum value. The smooth b lack line corresponds to the equivalent flux for a Maxwellian distribution with $T_e = 4.5$keV, for comparison with the bulk plasma.

for the kinetic inflation threshold of SRS in a homogeneous plasma. They showed that the magnitude of the trapped electron potential energy in the EPW must be greater than or equal to the energy gained by a particle in one complete trapped orbit due to velocity diffusion in the background plasma fluctuations. This ensures that trapping remains for at least one bounce period.

No such analytic threshold has been derived for an inhomogeneous plasma. However, when L_n is smaller the inhomogenous gain is smaller and the amplitude reached by

convective amplification of the SRS EPW is lower for the same intensity. Hence SRS in a shorter density scale length plasma is less likely to generate EPWs with sufficient amplitude for electron trapping effects to trigger the transition to iSRS.

Figure 4.6 (b) shows the measured intensity of SRS scattered light in three sets of simulations with density profiles centred at $0.12, 0.15, 0.20 n_{\mathrm{cr}}$, chosen so that the density ranges do not overlap (see Table 4.1). As the central density decreases, the intensity threshold for iSRS increases. As for the case of varying scale-lengths changing the threshold, this can be explained in terms of the Rosenbluth gain [Rosenbluth, 1972]. For a fixed density scale-length, as the density decreases, the Rosenbluth gain exponent also decreases. This means that the fluid gain through convective SRS is reduced. Hence SRS at a low density is less likely than that at higher density to generate EPWs with sufficient amplitude for electron trapping effects to trigger the transition to iSRS. For the parameters of Figure 4.7 (b) with $I_0 = 6.16 \times 10^{15}\mathrm{W/cm^2}$, the Rosenbluth gain exponent increases from ~ 1 to ~ 12 as the densities increase.

As well as understanding how the density scale-length of the plasma and the density at which iSRS is driven affects the iSRS threshold, we would like to understand how these factors affect the hot electron population. We consider three simulations from Figure 4.6 (a) with $I_0 = 2.98 \times 10^{15}\mathrm{W/cm^2}$, and three from Figure 4.6 (b), with $I_0 = 6.16 \times 10^{15}\mathrm{W/cm^2}$. Figures 4.7 (a,b) show the hot electron population in these simulations, in the form of histograms for the electron flux through the right boundary.

Figure 4.7 (a) shows the electron distribution function resulting from iSRS for three density scale-lengths. These are for a laser intensity above the onset threshold for iSRS but below an intensity which would lead to saturation. All results are for the same central density. The most prominent difference is that the peak electron energy increases with decreasing density scale-length. This results from the fact that the shorter density scale-length simulation access a higher peak density since the simulation domain size is the same for all three cases. The SRS matching conditions for these higher densities result in a higher phase speed of driven EPWs. Solving the SRS matching conditions for these densities, we find that the hot-electron energies calculated from the phase velocities are between $35 - 50$keV for all three cases.

Figure 4.7 (b), however, shows a clear dependence of the hot electrons from iSRS on density. As the density increases the maximum hot- electron kinetic energy also increases in line with the increase in SRS EPW phase velocities. Over the 2ps of the simulations the fraction of incident laser energy converted into hot-electrons with energy > 100keV are: 0, 0.002, and 0.15 for the $0.12, 0.15, 0.20 n_{\mathrm{cr}}$ densities. For the density scale-lengths $L_n = 300, 500, 1000$µm the fractions of incident laser energy converted into > 100keV hot- electrons are: $0.005, 0.001$ and 0 respectively.

4.5 Saturation

Several saturation mechanisms for iSRS in PIC simulations have been proposed, depending on the physical mechanisms present in the simulation. For simulations in 1D with immobile ions, there are three possible saturation mechanisms for SRS undergoing autoresonance: wave-breaking of the plasma wave; pump depletion of the laser driver; and frequency shift such that the autoresonance condition is no longer satisfied. In simulations with mobile ions and in higher dimensions, additional saturation mechanisms have been identified for iSRS in a homogeneous plasma. These additional saturation mechanisms are: Langmuir decay instability (LDI); wavefront bowing of the EPW; the trapped particle modulation instability (TPMI); and self-focusing [Yin et al., 2007].

We can eliminate EPW wave-breaking as the saturation mechanisms in our simulations as the maximum normalised EPW energy well below the wave-breaking limit in all cases. Take, for example, the simulation corresponding to $I_0 = 7.83 \times 10^{15}\mathrm{W/cm^2}$ on the red curve of Figure 4.6 (a). We can calculate the wave-breaking limit across the density range to be $E_{\mathrm{WB}}e/m_e c\omega_0 = 0.024 - 3.52$; but the maximum EPW energy in the simulation is $E_{\mathrm{EPW}}e/m_e c\omega_0 = 0.0056$, well below the limit. Figure 4.8 shows the Poynting flux of the scattered light (a) and incident laser (b) for a simulation with intensity in the saturated regime ($I_0 = 7.83 \times 10^{15}\mathrm{W/cm^2}$). We can see complete depletion of the pump correlated with the maximum intensity of scattered light first at approximately $x = 45\mu\mathrm{m}$, $t = 0.8\mathrm{ps}$. It is interesting to note that iSRS at low densities is depleting the pump before it can reach higher densities, where the growth of SRS would be even greater.

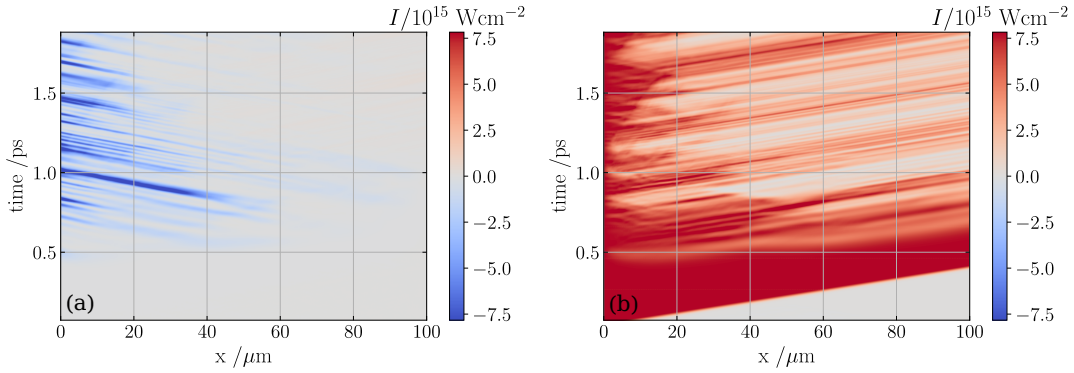

Figure 4.8: (a) Poynting flux of scattered light (b) laser energy, showing significant depletion of the pump. Simulation parameters: $L_n = 500\mu\mathrm{m}$ centred at $0.15n_{\mathrm{cr}}$ and $I_0 = 7.83 \times 10^{15}\mathrm{W/cm^2}$.

4.6 Conclusion

Inflationary SRS has been detected in PIC simulations of a inhomogeneous plasmas with parameters relevant to the shock-ignition model of ICF. This study demonstrates

an iSRS threshold $I_{\text{threshold}} \lesssim 5 \times 10^{15}\text{W/cm}^2$ across the whole range of parameters tested and that the location of this threshold depends on the density scale-length L_n. For the case with $L_n = 500\mu\text{m}$ and $I_0 = 4.83 \times 10^{15}\text{W/cm}^2$ significant iSRS would occur at $0.15n_{\text{cr}}$ generating hot-electrons with mostly < 100keV energies and depleting the laser drive available at higher densities. This is potentially beneficial to shock-ignition in that these electrons are likely to enhance the ignitor shock and prevent significant SRS at higher densities, potentially absolute at $0.25n_{\text{cr}}$. SRS at higher densities is likely to generate electron distributions with a higher percentage of > 100keV electrons than that from iSRS at lower densities. These results suggest that a potential route to use iSRS to the advantage of shock-ignition, assuming all SRS cannot be removed by other means, would be for the shock ignitor pulse to have the largest possible amplitude. This would ensure significant iSRS at lower densities and generate only hot-electrons with energies below 100keV. This in turn would pump deplete the laser reducing SRS at higher densities which could generate hot-electrons with energy above 100keV. These conclusions are however only valid for the restricted 1D, collisionless simulations presented in this paper and more detailed simulations, as outlined below, would be needed to fully assess the hot-electron distribution and its impact on SI schemes.

The simulations presented in this chapter highlight the importance of a thorough investigation of iSRS for any shock-ignition plans. These results are however a first study of the plasmas parameters where iSRS may occur. A full theoretical investigation of the potential impact of iSRS on shock-ignition will require significantly larger scale simulations. Of particular importance are multi-dimensional effects and laser speckle profiles. These would allow the competition between SRS and TPD as sources of hot-electrons to be assessed in two and three dimensions. The transverse non-uniformity associated with multi-dimensional effects is likely to affect iSRS through trapped electron side losses and a broader spectrum of EPWs resulting from side-scatter and TPD. Furthermore, the auto-resonance responsible for iSRS in these simulations may not be possible when a full speckle profile is included; since the extension of the resonance region may take the resonant waves outside of an individual speckle. The use of broadband laser systems to mitigate LPI will also need to be assessed in the kinetic regime of iSRS. All of these refinements to iSRS simulations will require considerably more computing resources but are none-the-less needed for a comprehensive treatment of LPI relevant to shock-ignition.

Chapter 5

Effects of laser bandwidth on inflationary stimulated Raman scattering

In this chapter, results of one-dimensional PIC simulations are presented, which represent the first investigation into the practical possibility of using broadband to suppress inflationary SRS in shock-ignition. The chapter begins with a review of the literature discussing suppression of SRS by broadband lasers. We then show that for a decoupled broadband laser, as defined by Zhao et al. [2017b], the non-linear frequency shift arising from kinetic effects must be taken into account when calculating the condition for suppression of iSRS. Next we consider the case of realistic shock-ignition schemes on two laser systems: frequency-tripled Nd : glass; and Argon Fluoride (ArF). In each of these cases we model the predicted maximum realistic bandwidth in its physically-correct functional form. The chapter concludes with a discussion of the limitations of the modelling done so far, and suggestions for future work.

N.B. In this chapter, bandwidths are given in units of tera-Hertz (THz) since this is standard in the literature. This can be converted to radians per second through the relation $\Delta\omega = 2\pi\Delta f$.

5.1 Motivation and literature review

Early results in the 1970s suggested that finite-bandwidth laser drivers could change the behaviour of parametric instabilities, by disrupting the three-wave coupling. These studies considered a variety of parametric instabilities, including: the parametric decay instability [Thomson and Karush, 1974]; stimulated Brillouin scattering [Kruer et al., 1973]; and stimulated Raman scattering [Raymer et al., 1979]. Recently, broadband suppression of parametric instabilities has, once again, become a fashionable topic of discussion, as it has been shown in simulations to be effective in suppressing cross beam energy transfer [Bates et al., 2020] and the absolute forms of stimulated Raman

	Absolute SRS	Convective fluid SRS	Inflationary SRS
Decoupled broadband laser	Zhao et al. [2017a]	Zhao et al. [2019]	?
Sinusoidal frequency modulation	Zhao et al. [2015]	Wen et al. [2021]	Wen et al. [2021]
Random phase modulation	Kruer et al. [1973]	Guzdar et al. [1991]	?
Random amplitude modulation	Thomson and Karush [1974]	Guzdar et al. [1991]	?

Table 5.1: Reference table for the effect of broadband on stimulated Raman scattering. Four types of bandwidth are considered, each of which will be explained in the relevant section of the literature review. Cells with a green background represent results which show effective suppression of the particular form of SRS by the particular form of bandwidth. Cells with a red background show theoretical results proving that random bandwidth will have no effect on convective fluid SRS. The cells containing question marks are the starting point for our investigation. The references contained in this table are the canonical ones, and do not make up a complete survey of the relevant results; this will appear in the literature review.

scattering and two-plasmon decay [Follett et al., 2019]. All lasers have some natural bandwidth, which arises from quantum effects in solid-state lasers and from the Doppler effect in gas lasers. However, for the majority of lasers relevant to ICF, this natural bandwidth is far too small to affect parametric instabilities.

As discussed in Chapter 4, Stimulated Raman Scattering (SRS) is a parametric instability of major concern to shock ignition; since it scatters light away from the target, and drives electron plasma waves to large amplitudes which then damp and send hot electrons towards the cold fuel. As such, many people are interested in the possibility of using broadband laser systems to suppress the growth of SRS in shock-ignition coronal plasmas. In the following literature review, we consider each of the main forms of SRS separately: absolute; convective-fluid; inflationary (convective-kinetic); and multi-beam. The original work presented in this chapter focuses on inflationary SRS, but we believe that it must be placed in its proper context by reviewing the literature for all types of SRS, since these are often concurrent and may all be present in the shock-ignition plasma corona. Furthermore, understanding the effect of broadband on non-inflationary forms of SRS may give us an idea for what types of broadband could work to suppress inflationary SRS. A handy overview of the literature review can be found in Table 5.1.

5.1.1 Absolute SRS

A brief revision of the theory of absolute SRS driven by a *monochromatic* laser driver can be found in Section 2.2.2 of this thesis.

Considering the case of random amplitude modulation of the laser driver, Thomson

and Karush [1974] showed that for an absolute parametric instability, with homogeneous growth rate γ_0 driven by a laser with bandwidth $\Delta\omega$, if $\Delta\omega > \gamma_0$ then the growth rate of the instability is reduced by a factor of $\gamma_0/\Delta\omega$. A consequence of this is that, for a fixed bandwidth $\Delta\omega$, the suppressive effect of the bandwidth increases as the incident laser intensity decreases.

PIC modelling of absolute SRS at low density and temperature ($n_e = 0.08 n_{cr}$, $T_e = 100$eV, corresponding to $k_{\mathrm{EPW}}\lambda_D \sim 0.08$) performed by Zhao et al. [2015] demonstrates the suppression of the SRS growth rate by frequency-modulated SSD-type bandwidth. In this thesis, SSD-type bandwidth refers to the form of bandwidth generated by the beam-smoothing method known as smoothing by spectral dispersion Skupsky et al. [1991] (see Section 2.4). In one-dimension the bandwidth from SSD can be modelled as a sinusoidal frequency modulation, like so:

$$E_z = a_0 \cos\left[2\pi t + b\sin(2\pi f_m t)\right], \tag{5.1}$$

where a_0 is the normalised vector potential, f_m the modulation frequency, and b the modulation depth. The total bandwidth can be approximated as $\Delta\omega = (2b+1)f_m$ [Zhao et al., 2015]. They find that the suppression effect is increased by increasing the bandwidth; and that for a fixed bandwidth, the suppression depends on the modulation frequency. They also note that the bandwidth has no effect on the saturated level of SRS, only the growth rate. In their conclusion they stress the importance of considering the temporal structure of the laser field in each bandwidth investigation.

In a follow-up paper Zhao et al. [2017b] consider SRS driven by light which is composed of a large number of beamlets each with different frequency and phase (called a decoupled broadband laser (DBL)). A decoupled broadband laser is defined in Zhao et al. [2017b] as

$$a_{\mathrm{DBL}} = \sum_{i=1}^{N} a_i \cos(\omega_i t + \phi_i), \tag{5.2}$$

where a_i, ω_i, and $\phi_i \in [-\pi, \pi]$ are the normalised amplitude, carrier frequency, and phase of each of the N beamlets. The central frequency and wavelength of the laser is (ω_0, k_0) and the total frequency spectrum bandwidth is $\Delta\omega_0$. For very large bandwidths (on the order of $10\%\omega_0$) they find that the growth rate of backward SRS is reduced compared to the frequency-modulated light with the same bandwidth, but that the scattered light still saturates at the same level as with no bandwidth.

The work of Zhou et al. [2018] develops the theory of absolute SRS suppression by bandwidth by considering the "highly nonlinear", kinetic case where $k_{\mathrm{EPW}}\lambda_D = 0.3$. They model the broadband laser pump spectrum as

$$a = \sum_{i=1}^{N} a_i \cos\left[(\omega_0 + \delta\omega_i)t\right], \tag{5.3}$$

where N is on the order of 100, $a_i = a_0/\sqrt{N}$ for all i, and $\delta\omega_i \in [-\Delta\omega/2, +\Delta\omega/2]$ is a random frequency shift within the total bandwidth $\Delta\omega$. As well as confirming the suppression of the growth rate measured in [Zhao et al., 2015, 2017b], they find that bandwidth in the range 2.25% to 3.0% actually acts to *enhance* SRS in the so-called "deep nonlinear stage" by increasing the resonant range in line with the non-linear frequency shift. Zhou et al. [2018] conclude that a broadband laser light is not an appropriate choice for suppression of absolute SRS on a several picosecond time-scale.

Finally, Follett et al. [2019] used the LPSE code in one dimension to show that continuous bandwidth on the order of $1\%\omega_0$, modelled as many spectral lines with random phases, can increase the absolute threshold for SRS.

5.1.2 Fluid convective SRS

We have seen, in the previous section, that absolute SRS can be suppressed using random bandwidth [Thomson and Karush, 1974]; deterministic frequency-modulated bandwidth [Zhao et al., 2015]; and bandwidth from a DBL [Zhao et al., 2017b; Zhou et al., 2018]. This is not true, however, for convective SRS in an inhomogeneous plasma. It was shown by Guzdar et al. [1991] that bandwidth in the form of random phase modulation reduces the growth rate of SRS, but it also increases the length of the resonance region. For a system with the laser and plasma satisfying certain conditions, these two effects cancel out and the bandwidth has no net effect on the SRS gain. The conditions for exact cancellation are: the homogeneous growth rate and bandwidth are much smaller than the plasma frequency at the resonance point ($\gamma_0, \Delta\omega \ll \omega_{pe}(x_{\rm res})$); the length of the interaction region and coherence length are less than the plasma size ($\ell, c/\Delta\omega < L_x$); and that the homogeneous growth rate is much smaller than the bandwidth ($\gamma_0 \ll \Delta\omega$) Guzdar et al. [1991]. This analytical result tells us that random phase modulation will not be sufficient to suppress convective SRS.

It may be possible, however, to suppress convective SRS by using a decoupled broadband laser (DBL). Zhao et al. [2017b] apply their theory of absolute SRS suppression in a homogeneous plasma by DBLs, to the case of convective SRS in an inhomogeneous plasma. For a plasma with a linear density profile and constant temperature such that $k_{\rm EPW}\lambda_D \ll 0.25$ throughout, they compare the electrostatic energy present in the simulation in the cases $\Delta\omega_0 = 0$ and $\Delta\omega_0 = 15\%$. They find that for the 15% bandwidth case, the electrostatic energy is reduced compared to with zero bandwidth and conclude that the linear convective SRS has been suppressed [Zhao et al., 2017b]. In a second paper the same year, Zhao et al. [2017a] consider the case of an inhomogeneous plasma density profile relevant to direct-drive ICF.

An analytic description of convective SRS suppression by DBLs is given in Zhao et al. [2019]; they find that SRS can be well-controlled for a laser beam structure of multiple frequency components and total bandwidth of a few percent. By considering the frequency difference between any two beamlets, they find that there is a critical

frequency difference below which the SRS instability regions for the beamlets overlap to form a single instability region. In this case, the two beamlets can be coupled with one EPW, leading to a higher growth rate for SRS. This effect is demonstracted in 1D PIC simulations, which show that SRS can grow to a high level if the beamlets satisfy this coupling condition, even if the total bandwidth is very large. Zhao et al. [2019] derive a gain exponent for convective-fluid SRS, in the limit of strong EPW damping, driven by two beamlets of different frequencies. They find that two beamlets are independent when

$$\delta\omega_0 \geq \frac{\pi n_0 c \left(\omega_0^2 - \omega_{pe}^2\right)^{3/2}}{8L\omega_0\omega_L^2\nu_p^2}, \tag{5.4}$$

where ω_L is the EPW frequency and ν_p the EPW Landau damping rate.

For the case of a DBL composed of more than two beamlets, it is necessary that the frequency difference between any two neighbouring beamlets ($\delta\omega = \Delta\omega/(N-1)$) satisfies Equation 5.4. Note that this condition is independent of the intensity of the incident laser. In theory, this condition would allow us to construct a DBL to suppress SRS in a large-scale inhomogeneous plasma, however, secondary amplification of back-scattered light by one of the beamlets is a possibility. Secondary amplification here refers to the continued amplification of the scattered light wave by another laser beamlet and electron plasma wave. Zhao et al. [2019] therefore consider another threshold for this secondary amplification: $\delta\omega_0 > \omega_{L1} - \omega_{L2}$ where $[\omega_{L1}, \omega_{L2}]$ is the range of EPW frequencies excited by SRS in the plasma (not including nonlinear frequency shift).

In support of their analytic results, Zhao et al. [2019] perform PIC simulations with parameters: $\lambda_0 = 0.33\mu\text{m}$; $I_0 = 2.5 \times 10^{15}\text{W/cm}^2$; $T_e = 2\text{keV}$; $n_e = [0.08, 0.12]n_c$; giving $k_{\text{EPW}}\lambda_D \sim [0.26, 0.35]$. They find that the box-averaged power in EPWs is reduced for $\Delta\omega = 2\%\omega_0$, and further reduced for $\Delta\omega = 4\%\omega_0$. It is not clear in this paper whether SRS is growing in the weakly or strongly kinetic regimes, or whether the growth is inflationary.

5.1.3 Inflationary SRS

Wen et al. [2021] derive a condition for the maximum gain of convective SRS driven by a sinusoidally frequency-modulated broadband laser, when the velocity of the resonance point is equal to the group velocity of the back-scattered light for as long as possible. By tuning the plasma parameters and/or laser parameters away from this condition, they can increase the threshold for kinetic SRS [Wen et al., 2021]. For SSD-type bandwidth of the form

$$\begin{aligned} E(x,t) &= E_0 \sin\left(\omega_0 t - \phi(x,t)\right) \\ \phi(x,t) &= \frac{1}{2}\frac{\Delta\omega}{\omega_m}\sin\left(\omega_m t - \frac{\omega_m}{c}x\right), \end{aligned} \tag{5.5}$$

the maximum gain criterion is given by the expression:

$$\Delta\omega\omega_m = \omega_{pe}c/2L_n. \tag{5.6}$$

The maximum gain criterion is verified through PIC simulations in the kinetic and fluid regimes. The left-hand side of Eq. 5.6 represents the maximum chirp ($|\partial_t\omega_0(x,t)|$) of the laser, and the right-hand side gives an expression for the spatial detuning due to density inhomogeneity. Several simplifying assumptions are made by the authors which allow them to derive this expression for the spatial detuning. Most importantly for our work, they omit the contribution of the non-linear frequency shift (which is proportional to the Langmuir wave amplitude) in their calculation of the velocity of the resonance point.

A key result of Wen et al. [2021] is that the threshold for iSRS driven by a sinusoidally frequency-modulated laser is independent of the bandwidth or frequency modulation alone, rather it depends on their product. Figure 5.1 shows results from our benchmarking of Wen's work. In this benchmarking study we recovered the results of their OSIRIS study using our own PIC code, EPOCH. We ran several simulations with fixed maximum normalised chirp ($\Delta\omega\omega_m/\omega_0 = 5.5\times10^{-6}$) and varied bandwidth. We find that the inflation threshold has a weak dependence on the bandwith alone. From this preliminary investigation, we were confident in our laser set-up and in the use of EPOCH for this project.

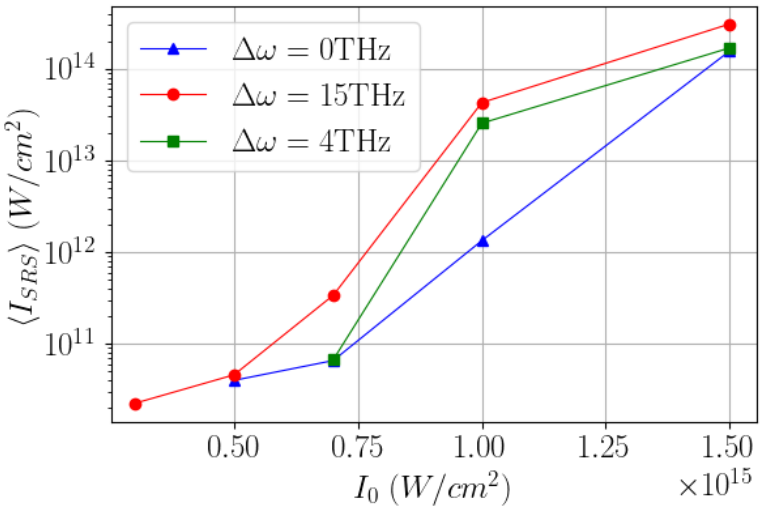

Figure 5.1: Intensity of light scattered by SRS, averaged over the last three picoseconds of each simulation, for three laser set-ups with fixed maximum normalised chirp ($\Delta\omega\omega_m/\omega_0 = 5.5\times10^{-6}$) and varied bandwidth. The simulation parameters common to all data-points are: $T_e = 4$keV; $L_n = 400\mu$m; $n_e(x) = 0.11n_{\rm cr}\exp(x/L_n)$; PPC=16,000.

Finally, studies have also been performed using the code LPSE in three dimensions which show that, at ignition scales, absolute multi-beam backward SRS can be mitigated

with bandwidth $\sim 1.6\%$ [Follett et al., 2021]. From this literature review (summarised in Table 5.1), it is clear that there is no complete picture of how bandwidth affects convective SRS gain in inhomogeneous plasmas.

5.2 Decoupled broadband lasers

The work in this section was presented at the 62nd Annual Meeting of the American Physical Society Division of Plasma Physics in November 2020 [Spencer et al., 2020].

In this investigation we applied the theory of Zhao et al. [2019] to the inflationary SRS set-up from Spencer et al. [2020]. At the time, Zhao's result was the most relevant for SRS in inhomogeneous plasmas (with Wen et al. [2021]'s result not being published until after the APS conference). We used the following laser and plasma parameters to allow for direct comparison with the monochromatic case in Spencer et al. [2020]: $L_n = 500\mu\text{m}$; $n_e(x) = 0.14 n_{\text{cr}} \times \exp(x/L_n)$; $T_e = 4.5\text{keV}$; PPC = 2048; and $L_x = 100\mu\text{m}$. Given these plasma conditions, we can calculate the *minimum* frequency difference required for two neighbouring beamlets to be independent as:

$$\begin{aligned} \delta\omega &\geq \frac{\pi n_0 c}{8 L \omega_0} \frac{\left(\omega_0^2 - \omega_{pe}^2\right)^{3/2}}{\omega_L^2 \nu_p^2} \\ &> 2.78 \times 10^{23} \max_{n_e} \frac{\left(\omega_0^2 - \omega_{pe}^2\right)^{3/2}}{\omega_L^2 \nu_p^2} \\ &> 0.31\% \omega_0, \end{aligned} \tag{5.7}$$

where ω_L and ν_p are calculated numerically from the three-wave matching conditions. However, if we take into account the threshold for secondary amplification we find that $\delta\omega > 2\%\omega_0$. Since this requirement is stronger, our final design for the DBL is: $\delta\omega = 2\%\omega_0$; $N = 3$; $\Delta\omega = 4\%\omega_0$. Note that this is the minimum total bandwidth predicted to be effective in suppressing the growth of SRS according to Zhao et al. [2019].

We also consider a second simulation in which the range of EPW frequencies is found by inspection of Figure 4.5 (b). It is clear that the range of excited EPWs is greater than the $2\%\omega_0$ predicted by fluid theory (white dashed lines). For our second simulation, the DBL is such that: $\delta\omega = 6\%\omega_0$; $N = 3$; $\Delta\omega = 12\%\omega_0$. For both simulations, the laser intensity is chosen such that the summed beamlet intensities are above the threshold for iSRS and also above the saturated intensity (moving to a higher intensity does not increase the reflectivity due to iSRS). This intensity is chosen from inspection of Figure 4.6 (a) to be $I_0 = 4.83 \times 10^{15}\text{W/cm}^2$. For three beamlets, the individual beamlet intensity is $I = 1.61 \times 10^{15}\text{W/cm}^2$, which Figure 4.6 (a) tells us is above the threshold for iSRS. This means that each beamlet should, in theory, be able to drive inflationary SRS independently of the others, and that we are not just creating suppression by driving iSRS below its threshold.

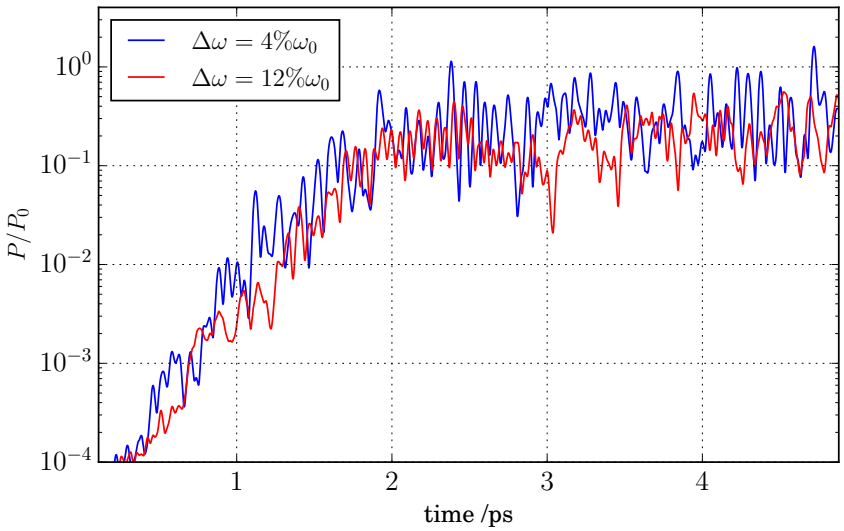

Figure 5.2: Reflected light from SRS a the left simulation boundary, as a function of time. The time-averaged reflectivities for $t > 1$ps are: 27% when $\Delta\omega = 4\%\omega_0$ and 13% when $\Delta\omega = 12\%\omega_0$. The base case ($\Delta\omega = 0$) is not plotted here, for clarity, but has time-averaged reflectivity of 29%.

Figure 5.2 compares the time-resolved reflectivity for the simulations with $\Delta\omega = 4\%\omega_0$, and $\Delta\omega = 12\%\omega_0$. We see that the initial linear growth period of $\langle R_{\mathrm{bSRS}} \rangle$ and the saturation time are the same for both cases. However, the level of SRS is consistently lower for the higher bandwidth case. This suggests that we are seeing a true suppression of the SRS behaviour, rather than a change in the intensity threshold or growth time. The time-averaged reflectivities for the 0%, 4%, and 12% bandwidths are 29%, 28%, and 13% respectively. From this, we conclude that the bandwidth requirement calculated in Zhao et al. [2019] is not sufficient to suppress inflationary SRS.

Figures 5.3 and 5.4 provide us with an explanation for why Zhao et al. [2019]'s bandwidth construction must be extended to include the contribution of the non-linear frequency shift. We consider first the electrostatic fields; Figure 5.3 shows the 2D Fourier transforms of the E_x field over all space and time. Figure 5.3 (a) shows that SRS is growing at frequencies below those predicted from the fluid Bohm-Gross dispersion relation for EPWs (white dashed lines), and that the areas of high spectral density are not clearly separated. Figure 5.3 (b), however, shows three pairs of bright spectral features, each sitting on a unique Stoke's line. This suggests that each of the three beamlets of the decoupled broadband laser is driving a unique SRS instability, that does not support any of the two others.

This conclusion is supported by inspection of the electromagnetic wave frequencies plotted in Figure 5.4. In this plot we see that for the case $\Delta\omega = 4\%\omega_0$ (black line) the scattered light forms a single spectral feature, but three distinct scattered light features when $\Delta\omega = 12\%\omega_0$ (red line).

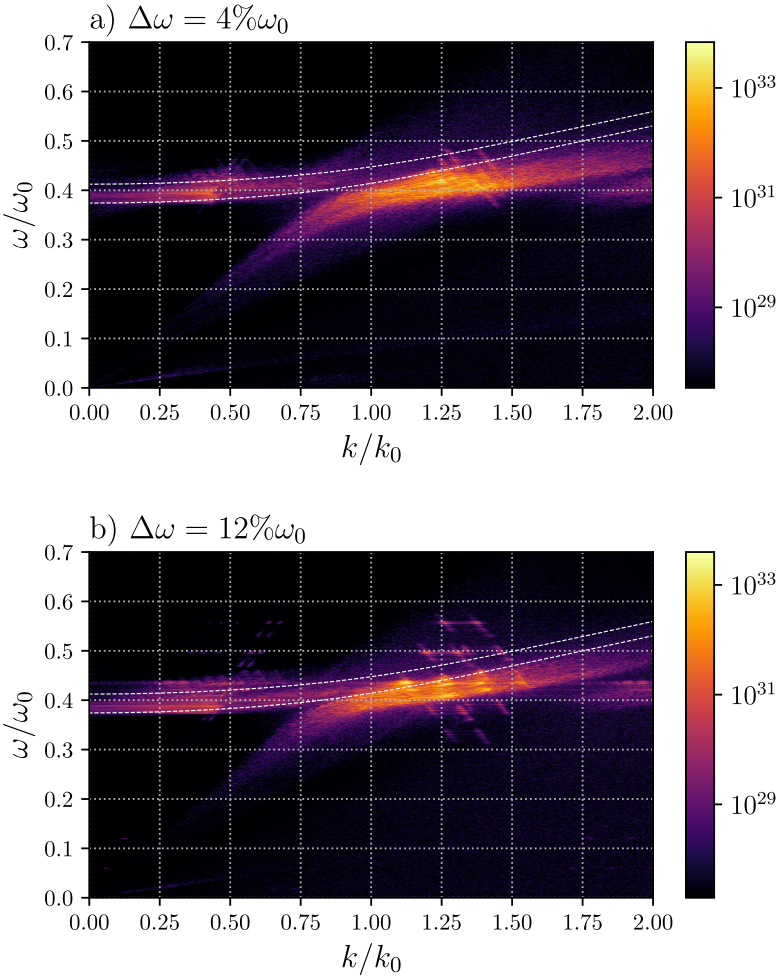

Figure 5.3: Two-dimensional Fourier transform of E_x over all space and time. White dashed lines show the EPW Bohm-Gross dispersion relations at the maximum and minimum plasma densities, calculated from fluid theory.

5.2.1 Conclusion

If we are to use decoupled broadband lasers for the suppression of inflationary SRS as described in Zhao et al. [2019], the bandwidth between any two beamlets should satisfy

$$\delta\omega > \max_{n_e}\{\omega_{\mathrm{EPW}}\} - \min_{n_e}\{\omega_{\mathrm{EPW}}\} + |\delta\omega_{NL}|, \tag{5.8}$$

where the maximum/minimum EPW frequencies are calculated from the SRS matching conditions with fluid dispersion relations. Since analytic expressions for $\delta\omega_{NL}$ can only be found for a small number of particular plasma distribution functions, the contribution from the non-linear frequency shift is probably best calculated, in the author's opinion, from fully kinetic simulations.

We decided not to pursue our investigation into DBL-type bandwidth any further since there are, at time of publication, no plans to implement such bandwidth on any

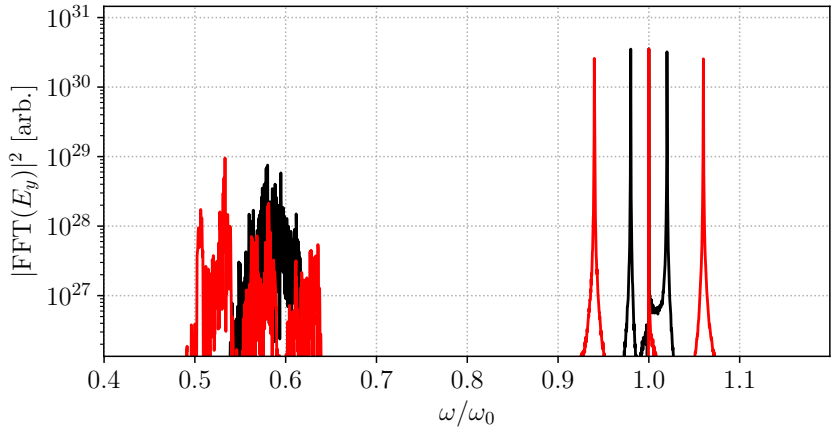

Figure 5.4: One-dimensional Fourier transform of E_y at $x = x_{\mathrm{mid}}$ over all simulation time. The black lineout shows the incident laser and reflected light spectra for the case $\delta\omega = 2\%\omega_0$; $N = 3$; $\Delta\omega = 4\%\omega_0$. The red lineout shows the incident laser and reflected light spectra for the case $\delta\omega = 6\%\omega_0$; $N = 3$; $\Delta\omega = 12\%\omega_0$. In the 12% bandwidth case, the reflected light has three distinct spectral features, but in the 4% bandwidth case the reflected light forms a single feature.

lasers which might be used in inertial confinement fusion. In the next section, we turn our attention to laser systems currently being considered for ICF experiments.

5.3 Realistic laser bandwidth

This section concerns the results of our investigation into broadband suppression of inflationary SRS on different broadband laser systems. We consider shock-ignition driven by two different laser systems: frequency-tripled Nd : glass lasers, such as the NIF and LMJ; and Argon Fluoride (ArF) lasers. Each laser has a different frequency and native bandwidth. A third laser system of interest to shock-ignition is Krypton Fluoride (KrF) lasers, such as the Nike laser at the Naval Research Laboratory (NRL), which has an intrinsic bandwidth of 3THz [Obenschain et al., 2015]. However, we do not consider KrF lasers here, due to time constraints; this is left for future work.

Andrew J. Schmitt (Naval Research Laboratory) provided us with density, temperature and intensity lineouts in one-dimension from simulations of shock-ignition with Nd : glass and ArF lasers. We selected a single time slice for our PIC simulations, just before the interaction pulse enters the under-dense plasma created by the assembly pulse.

For all the simulations presented in this section, the following EPOCH parameters are constant: $\Delta x = \min_x(\lambda_D)$; PPC $= 16,000$; $T_{\mathrm{end}} = 6$ps; thermal boundaries for particles; field boundaries are laser (x_{min}), and absorbing boundaries (x_{max}). We treat the ions as a neutralising background population to allow us to pinpoint the effect of bandwidth on inflationary SRS only. The incident laser intensity is varied around both sides of the threshold intensity for inflationary SRS. The approximate threshold

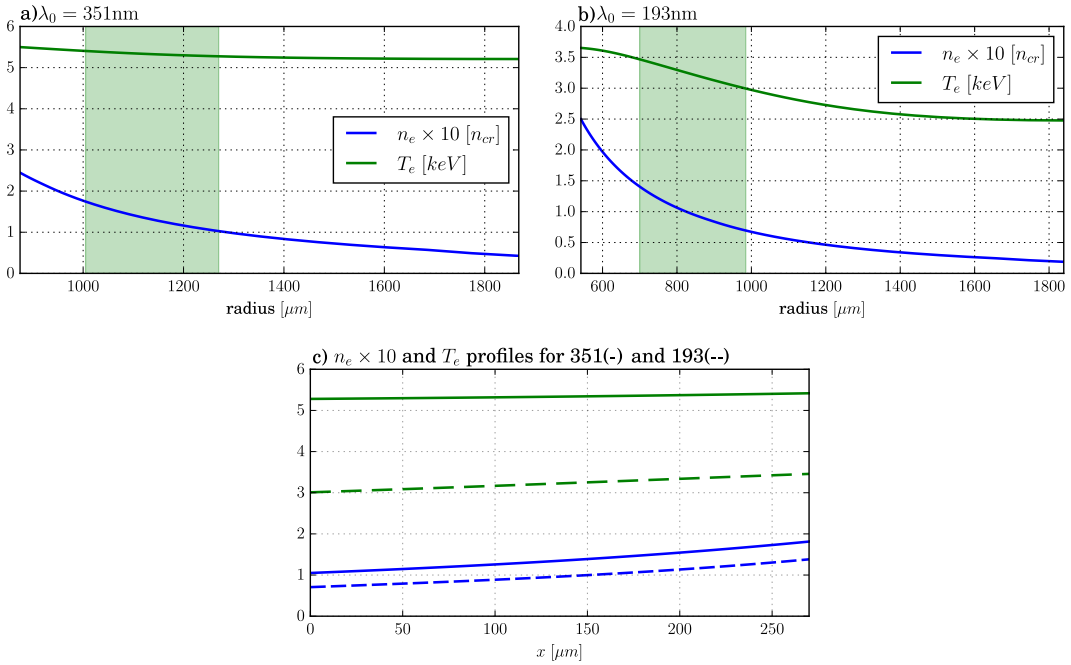

Figure 5.5: Sub-figures a) and b) show density and temperature line-outs from NRL simulations at the end of the assembly pulse and the start of the ignition pulse. The laser is incident from the right, and the left-hand side boundary represents the quarter critical density surface. The green highlighted areas show the density and temperature range such that $0.3 < k_{\mathrm{EPW}}\lambda_D < 0.45$. Sub-figure c) shows the final density and temperature profiles used for our campaign, defined by third order polynomials on the interval $[0, 270\mu\mathrm{m}]$, and with the laser incident from the left.

intensity is found by varying the intensity for identical PIC set-ups to find the minimum intensity such that the time-averaged intensity of scatter from bSRS is greater than 10% of the incident laser intensity. The very high number of particles per cell (16,000 compared to 2048 in the previous chapter) comes from convergence testing on the iSRS threshold for the 351nm base case. Wen et al. [2021] also report convergence of the iSRS threshold at $16,000$ PPC. It was also less expensive to use a large number of particles per cell than to run 10 simulations, each with 2048 PPC, with different random seeds.

Wavelength / nm	L_x /µm	T_e / keV	n_e / n_{cr}	ω_{pe} / ω_0	L_n / µm
351	270	5.4	$[0.105, 0.175]$	$[0.33, 0.42]$	$[420, 590]$
193	270	3.5	$[0.071, 0.140]$	$[0.26, 0.37]$	$[330, 470]$

Table 5.2: Table shows plasma parameters from simulations performed at the NRL, chosen such that $k_{\mathrm{EPW}}\lambda_D$ is between 0.3 and 0.45. The temperature given is the maximum temperature of the particles initialised at $t = 0$, as there is, in reality, a slight temperature gradient in the electron profile.

λ_0 / nm	n_e or T_e	a_0	a_1	a_2	a_3
351	density	1.05×10^{-1}	1.81×10^{2}	2.02×10^{5}	6.47×10^{8}
351	temperature	5.28	3.16×10^{2}	6.60×10^{5}	1.80×10^{8}
193	density	7.06×10^{-2}	1.66×10^{2}	3.95×10^{4}	1.01×10^{9}
193	temperature	3.01	1.47×10^{3}	1.31×10^{6}	-2.27×10^{9}

Table 5.3: Coefficients for the third-order polynomials describing density and temperature profiles in our 1D PIC simulations, for anyone wishing to replicate the simulations. The density and temperature polynomials take the form $n_e(x) = \sum_{i=0}^{3} a_i x^i$.

5.4 351nm Nd : glass laser

We begin by considering shock-ignition with frequency-tripled Nd : glass lasers, such as the NIF and LMJ. In these simulations, the laser has wavelength 351nm, incident intensity in the range $0.4 - 4.0 \times 10^{15}\mathrm{W/cm^2}$, and maximum bandwidth of 1THz $= 0.12\%\omega_0$. This bandwidth is the maximum applied as part of smoothing by spectral dispersion (SSD) on the OMEGA laser system [Regan et al., 2005]. According to Lehmberg et al. [2020] this maximum bandwidth might be increased up to 10THz by optical parametric amplification; we do not consider this case here, since it is still in the very early stages of development.

5.4.1 Base case: $\Delta f = 0$

As stated in Section 5.3, the plasma density and temperature profiles are taken from the library of radiation hydrodynamic simulations at the Naval Research Laboratory. The plasma densities probed are very similar to those considered in Chapter 4, and so we would expect the simulations to exhibit similar key features. By inspection of the scattered-light Poynting fluxes for simulations with incident laser intensities either side of the SRS threshold (Figure 5.6), we see that the scattered light signal is dominated by backward-travelling SRS light. From the near-laser Poynting flux (not plotted), we see that the main saturation effect is pump depletion of the laser close to the right boundary. Finally, the two-dimensional Fourier transforms of the E_x field (not plotted) show that SRS is resonant well-below the frequencies predicted by the Bohm-Gross dispersion relation. In summary, the base case simulations with a monochromatic laser behave as we would expect from Chapter 4, and their interpretation is straightforward. In the next section, we will add bandwidth to the laser driver in hopes of reducing the threshold for inflationary SRS, in line with the theory of Wen et al. [2021].

5.4.2 SSD-type bandwidth: $\Delta f = 1\mathrm{THz}$

1THz is the maximum bandwidth currently implemented with SSD on a 351nm laser, achieved at the Omega laser facility [Regan et al., 2005]. Adding bandwidth to the laser

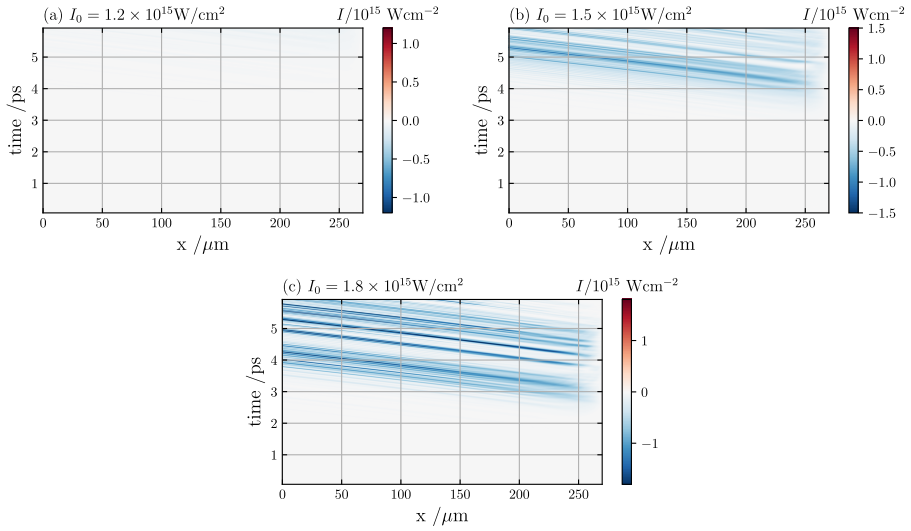

Figure 5.6: $\lambda_0 = 351$nm. Poynting flux of scattered light as function of space and time, for three laser intensities: below (a), at (b), and above (c) the iSRS threshold intensity estimated from Figure 5.7. Each signal is normalised to the incident laser intensity, and plotted with a linear colourbar.

pulse is essential to the process of smoothing by spectral dispersion, as only then will the diffraction grating have something to disperse. The additional bandwidth which is required to use SSD is added to the fundamental laser frequency using an electro-optical modulator [Hohenberger et al., 2016]. In one-dimension, the spectrum from SSD reduces to a frequency-modulated bandwidth. According to Wen et al. [2021], in order to increase the iSRS threshold we require that the modulation frequency associated with the SSD satisfies $\omega_m \gg \omega_{pe} c/2L_n\Delta\omega$. From the plasma parameters given in Table 5.2 and bandwidth of 1THz, this requirement becomes:

$$\begin{aligned} \omega_m &\gg \frac{c}{2\Delta\omega}\frac{\omega_{pe}}{L_n} \\ &\gg 1.50 \times 10^4 \max_{n_e} \frac{\omega_{pe}}{L_n} \\ &\gg 128\text{THz}. \end{aligned} \tag{5.9}$$

This is problematic, since the optimal modulation frequency for SSD-type smoothing is on the order of 10GHz = 0.01THz [Kelly et al., 2013; Regan et al., 2005].

We can implement a continuous-bandwidth frequency-modulated laser in EPOCH using the standard EPOCH laser-driver in one dimension as

$$\begin{aligned} E(t) &= E_0 \sin(\omega_0 t - \phi(t)) \\ \phi(t) &= \frac{1}{2}\frac{\Delta\omega}{\omega_m}\sin(\omega_m t), \end{aligned} \tag{5.10}$$

for $\Delta\omega = 1$THz and $\omega_m = 260$THz (a normalised maximum chirp of $\Delta\omega\omega_m/\omega_0^2 = 3.8 \times 10^{-4}$).

Figure 5.7 shows the dependence of back-scattered SRS light on the incident laser intensity for simulations with a 351nm laser, with and without SSD-type bandwidth. In Chapter 4, the equivalent plots (for example, Figure 4.6) had a dashed line, which represented the estimated back-scattered light intensity from our simple fluid model. No such line is plotted in this chapter, since the density profiles no longer take the simple form: $n_e(x) = n_{\min}\exp(x/L_n)$, and the model does not work for non-monochromatic drivers. In Figure 5.7, the blue triangular markers represent the base-case with no bandwidth, and the red circular markers represent simulations with the bandwidth calculated from Wen et al. [2021]. Straightforward application of Wen's theory, for a maximum total bandwidth of 1THz, suggests that the threshold for inflationary SRS will increase if the modulation frequency satisfies the maximum local chirp rate of the pump exceeds the spatial detuning due to the density gradient. However, we can see from Figure 5.7 that the threshold doesn't seem to change or, perhaps, seems to decrease.

Unfortunately, we do not have sufficient data output from the simulations to work out why this apparently failed. One potential solution, given more compute, would be to perform a finer scan around the threshold, and to do a statistical analysis with multiple random PRNG seeds. However, it is our view that this is not a valuable use of compute resources, when it does not seem like any realistic laser system would be able to meet the criterion derived in Wen et al. [2021] for increasing the iSRS threshold.

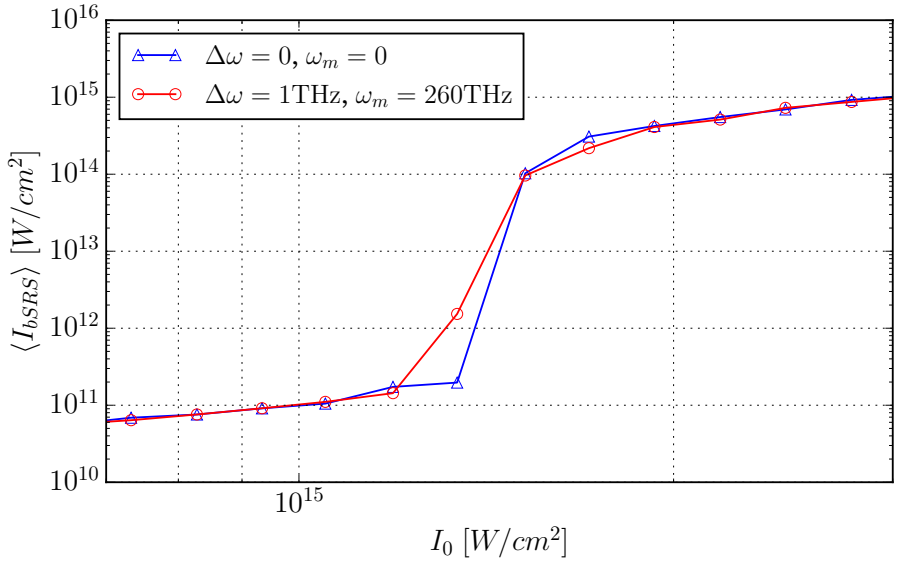

Figure 5.7: $\lambda_0 = 351$nm. Intensity of light scattered by backward SRS, time-averaged for all $t > 2$ps, for simulations with and without SSD-type laser bandwidth. The incident laser intensity varies between 7×10^{14}W/cm^2 and 3×10^{15}W/cm^2.

5.5 193nm Argon Fluoride

Excimer lasers have a broad amplification spectrum in the UV when compared to Nd: glass lasers. In this section we consider the argon fluoride (ArF) laser under development at the NRL, which is predicted to have native bandwidth up to 10THz [Obenschain et al., 2020]. The simulations presented in this section have a wavelength of 193nm, incident intensity in the range $2.0 - 5.0 \times 10^{15}\text{W/cm}^2$, and maximum bandwidth of $10\text{THz} = 0.64\%\omega_0$.

5.5.1 Base case: $\Delta f = 0$

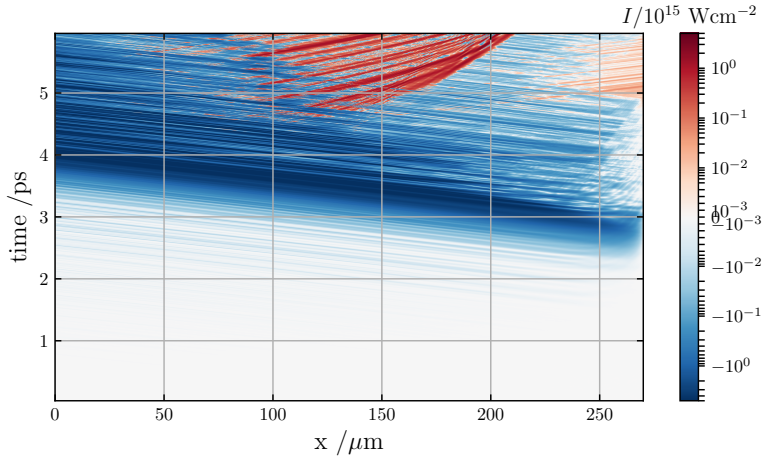

Figure 5.8: $\lambda_0 = 193\text{nm}$. Intensity of SRS-scattered light as a function of space and time, for the 193nm base-case simulation with $I_0 = 5 \times 10^{15}\text{W/cm}^2$.

Interpreting the effect of the bandwidth on inflationary SRS in our simulations of ArF lasers is not as straightforward as calculating the time-averaged reflected light at the left boundary (as we did in the previous section). We now examine in detail the simulation with $I_0 = 5 \times 10^{15}\text{W/cm}^2$, in order to understand the various concurrent SRS behaviours that contribute to the total SRS behaviour. Figure 5.8 shows the Poynting flux in the simulation domain as a function of space and time, calculated from the E_y and B_z fields that were filtered to remove contributions from the laser. Our first observation is that, although it only takes the laser $\sim$ 1ps to cross the box, it takes $\sim$ 2ps to begin exciting iSRS. We then see very large backward SRS growth with intensity approximately equal to the incident laser intensity. From inspection of the time-dependent reflectivity at the left boundary (Figure 5.9), the instantaneous reflectivity is sometimes greater than three. This large reflectivity leads to pump depletion of the laser. The intensity of the backward-travelling scattered light waves is reduced for $t > 4.5$ps. This is caused by the fact that the SRS-reflected light is itself undergoing SRS in the low-density plasma, this is the large red feature in Figure 5.8. We can discern that this signal must be re-scatter, and not forward-SRS, by inspecting the $E_{x,y}(\omega, k)$ signals plotted in Figure 5.10. The

blue circled signals in Figure 5.10 sub-figures (c) and (d) represent the three waves involved in the re-scatter SRS process, which produces a backwards-travelling (with respect to the incident laser) EPW. The red circle on sub-figure (c) is the scattered light from forward SRS of the original laser, which has much smaller $v_{ph} = \omega/k$ than the forward-travelling re-scattered light (blue circled signal with very small k).

The final SRS signal present in Figure 5.8, is the weak forward-scatter SRS signal which can be seen for $x > 200\mu\text{m}, t > 4.5\text{ps}$. This forward-SRS signal is also highlighted in Figure 5.10 in red. The over-lapping nature of these three signals means that it is difficult to define whether SRS is suppressed by the addition of laser bandwidth.

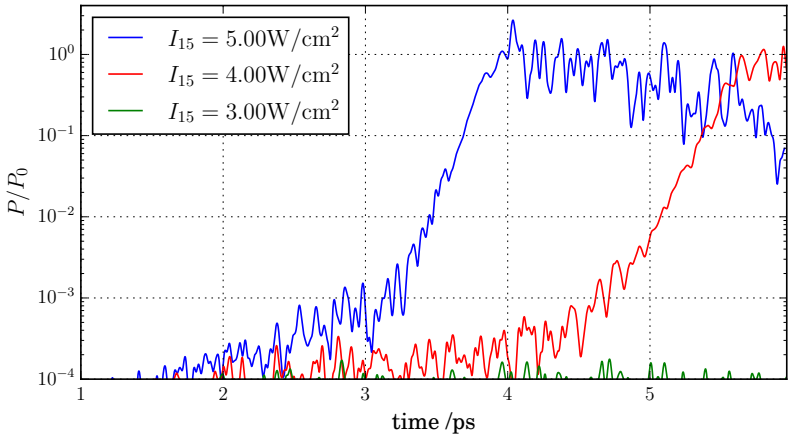

Figure 5.9: $\lambda_0 = 193\text{nm}$. Reflectivity due to backward SRS at left boundary, smoothed on scales less than 0.01ps, for three different monochromatic laser intensities. Each is normalised to its own incident laser power. The time-averaged reflectivity over all $t > 1\text{ps}$ are $26.8\%, 7.20\%, 0.008\%$ for the three decreasing intensities.

The most common method in the literature for quantifying the impact of a parameter on inflationary SRS is to look at how the threshold changes as that parameter is varied. In these analyses, the threshold is measured in terms of the amount of back-scattered SRS light reaching the laser-entry boundary (for examples of this method, see: [Vu et al., 2007; Wen et al., 2021; Yin et al., 2009]). This is the method applied in Chapter 4, and it provides us with a good idea of how the iSRS threshold depends on the coronal density scale-length and the density at which iSRS is driven. However, this method of calculating the iSRS threshold relies on the fact that, wherever back-scattered light is generated in the plasma, given enough time it will reach the laser-entry boundary. Furthermore, the standard methods for calculating iSRS thresholds assume that the SRS-reflected light increases monotonically with the incident laser intensity. We can see from the analysis above, that this is not always true for the simulations presented in this section. Figure 5.11 shows what happens when this assumption fails. The blue triangular markers represent the backward-scattered SRS light averaged over the entire simulation time, for times greater than 1ps (the box-crossing time for the laser). We can see that is has the chracteristic shape we that we have become accustomed to

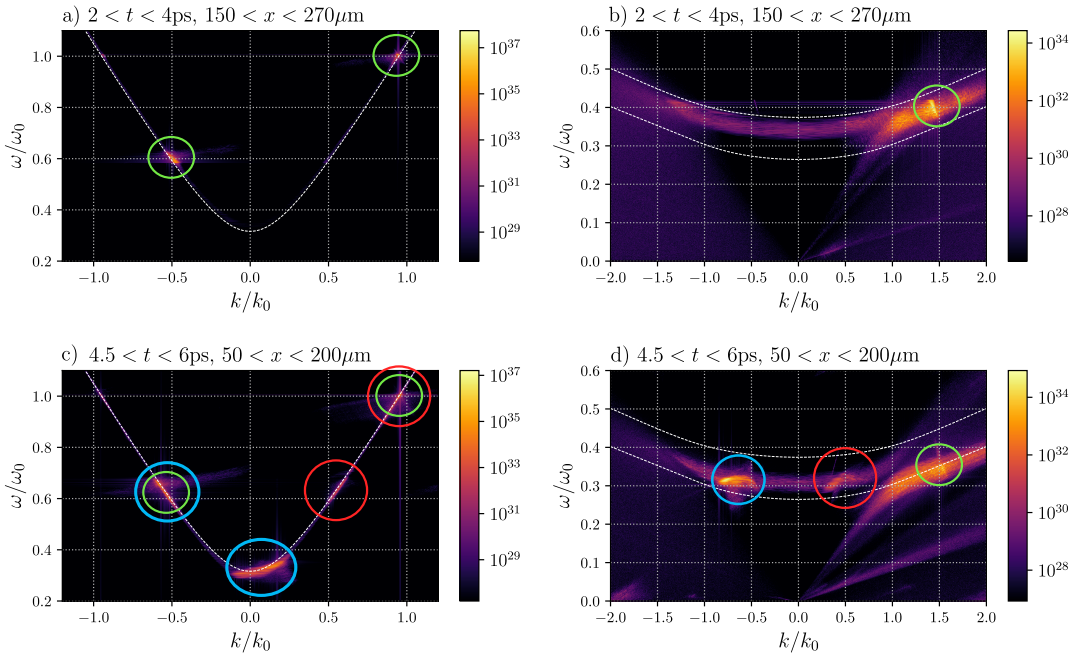

Figure 5.10: $\lambda_0 = 193$nm. 2D Fourier transforms of E_y (a,c) and E_x (b,d) for the 193nm laser base-case with $\Delta\omega = 0$, and plasma parameters from Table 5.2. Taken together, sub-figures a) and b) show inflationary backward SRS (bSRS) of the laser driver. The green circled signals are (from left to right) the back-scattered EMWs; the incident laser; and the forward-travelling EPWs. In sub-figures c) and d) we see the same bSRS signal as at earlier time (still highlighted with green circles), but we also see backward SRS of the bSRS light (circled in blue). This *rescatter* SRS occurs at densities less than $0.1n_{cr}$, and produces a backward travelling EPW. The white dashed lines represent the electromagneticz (a,c) and Bohm-Gross dispersion relations (b,d) for the plasma. Axes are normalised to the laser frequency and wavenumber in vacuum. Red-circled signals represent forward-scatter of the incident laser.

throughout this thesis: with a threshold intensity past which the signal increases by several orders of magnitude, and a rapid saturation at this level. However, if we average over different periods of time (the red circles and green squares in Figure 5.11) then this "standard" shape is lost.

These additional complications arise because the simulations with $\lambda_0 = 193$nm have a large portion of the plasma corona satisfying $n_e < 0.11n_{cr}$, where the effects of re-scatter can become important. Just as the SRS frequency matching conditions mean that SRS can only take place below the quarter critical density of the incident laser, they also mean that re-scatter SRS can only occur below $n_{cr}/9 \simeq 0.11n_{cr}$.

5.5.2 Intrinsic bandwidth: $\Delta f = 10$ THz

In this section, we simulate shock-ignition driven by a laser with 10THz of native bandwidth, which is considered realistic for ArF laser systems currently under development [Obenschain et al., 2020]. To model the continuous laser spectrum, we follow the method

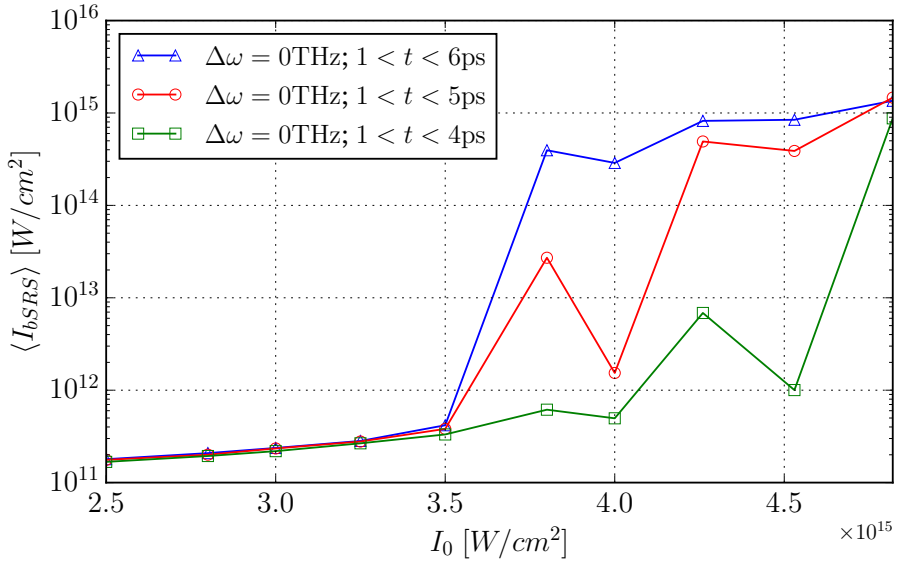

Figure 5.11: $\lambda_0 = 193$nm. Intensity of SRS-scattered light as a function of incident laser intensity averaged over three time periods of different total lengths.

presented in Bates et al. [2020] and distribute 50 beamlets of different frequencies around the central frequency. The intensities of the lines follow a flat-top distribution. Each beamlet has a random phase so the total driven laser field looks like this:

$$\begin{aligned} E(x,t) &= \sum_{i=1}^{50} E_i \sin(\omega_i t + \phi_i) \\ \phi_i &\in [0, 2\pi] \\ \omega_i &\in [\omega_0 - \Delta\omega/2, \omega_0 + \Delta\omega/2] \end{aligned} \tag{5.11}$$

Figure 5.12 compares the intensity of backward-scattered light from inflationary SRS as a function of the incident laser intensity, for 193nm lasers with and without bandwidth. For the base-case with zero bandwidth (red circular markers), we can estimate a threshold intensity for inflationary SRS of approximately 3.5×10^{15}W/cm^2. However, for the case with 10THz bandwidth (blue triangular markers) we cannot define a threshold. As we saw in the previous section, these simulations have multiple scattering processes which develop on different time-scales and saturate non-linearly at different levels. In order to un-pick the contributions from these different scattering processes, we would need to run simulations which output the field data everywhere in the domain, rather than just at the left and right boundaries. This represents a significant computational effort, but would certainly need to be done in order to prepare this work for publication.

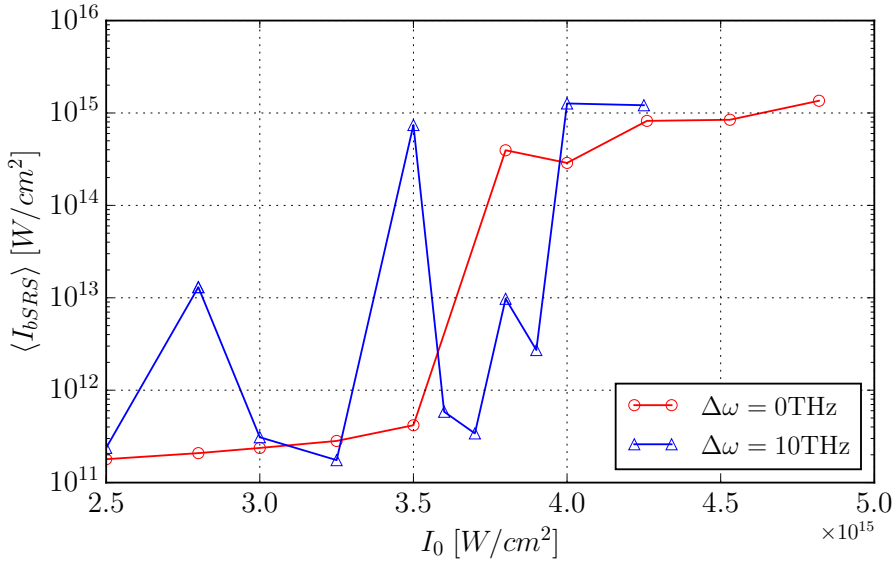

Figure 5.12: $\lambda_0 = 193$nm. Intensity of SRS-scattered light averaged over all simulation time, for simulations with and without bandwidth.

5.6 Conclusion

Referring back to Table 5.1, we can see that this chapter has looked at two of the open questions about the effect of broadband on inflationary SRS, and has provided an answer for one. The first question we sought to answer was: can a decoupled broadband laser (as defined by Zhao et al. [2017a]) be constructed that will suppress inflationary SRS in a shock-ignition coronal plasma? We found that such a DBL can be constructed, if the bandwidth between any two beamlets is at least the difference between the minimum and maximum resonant EPW frequencies plus the non-linear frequency shift from electron trapping. We then went on to consider if the prediction of Wen et al. [2021], that a laser with SSD-type bandwidth can be constructed such that the threshold for inflationary SRS increases, was correct for realistic bandwidth on 351nm laser systems. We were not able to increase the inflationary SRS threshold in our simulations using the bandwidth prescribed in Wen et al. [2021]. Computational limitations mean that this study is somewhat incomplete. In order to prepare this work for publication, we would like to run more simulations which record high-frequency electric and magnetic field data throughout the plasma to allow detailed analysis of the competing scattering processes, as is done in Chapter 6. Finally, we examined the effect of 10THz random phase bandwidth on inflationary SRS in the context of shock-ignition on a 193nm argon fluoride laser. For the base-case with zero bandwidth, we estimated a threshold intensity for inflationary SRS of approximately 3.5×10^{15}W/cm^2. However, with the addition of bandwidth, we could not define a comparable threshold.

In mid September 2021, as this thesis was being prepared, a paper by Ma et al. [2021] proposed the development of "sunlight-like" broadband lasers, which are shown

to increase the threshold for absolute SRS in 1D and 2D homogeneous PIC simulations. These lasers have a flat-top frequency spectrum; a random frequency spectrum and variations in amplitude as a function of time. It would be interesting to investigate the potential of these "sunlight-like" lasers to suppress inflationary SRS.

Chapter 6

Effects of an External Magnetic Field on Stimulated Raman Scattering

In this chapter, we present work performed by the author while employed as a Junior Specialist at the University of California, San Diego between January and April 2020. The project was supervised by Professor Farhat Beg, and lead by Adam Higginson (ORCID: 0000-0002-2727-8075). The work presented (including data generated and data analysis) was carried out by the author, except in the case outlined below:

- Figure 6.2 was produced by M. Bailly-Grandvaux (ORCID: 0000-0001-7529-4013).

The chapter begins with a review of the literature which discusses the effect of a magnetic field on stimulated Raman scattering. We then present modelling, performed by the author, of an experiment performed at the Laboratoire pour l'Utilisation des Lasers Intenses (France) by: J. R. Marquès, P. Loiseau, J. Béard, A. Castan, B. Coleman, T. Gangolf, L. Lancia, A. Soloviev, O. Portugall, and J. Fuchs. Analysis of the SRS diagnostics was performed by J. R. Marquès, and (revisited) by M. Bailly-Grandvaux. The experiment showed a small increase in SRS with an applied magnetic field, and this is recreated in our simulations.

We then go on to investigate how the effect of the magnetic field depends on $k_{\mathrm{EPW}}\lambda_D$ of the SRS electron plasma wave. This work was performed in collaboration with Ben Winjum (University of California, Los Angeles) and Simon Bolaños (ORCID: 0000-0002-9234-1210).

6.1 Motivation and literature review

In the previous two chapters, we looked at stimulated Raman scattering (SRS) in the hot and long density scale-length plasmas of the shock-ignition corona. In this chapter however, we consider low-density, homogeneous plasmas relevant to our collaboration's

laser direct-drive gas-jet experiments. As in the previous two chapters, we would like to understand how stimulated Raman scattering (SRS) behaves in the plasmas of interest, in order to mitigate or enhance it to suit our requirements.

The following literature review is divided into two sections: firstly, we consider results from PIC simulations which show that an external magnetic field can suppress SRS in the kinetic regime. Secondly, we consider results from fluid theory which suggest that magnetic fields can increase reflectivity due to SRS by changing the balance between stimulated Raman and Brillouin scattering in laser-produced coronal plasmas.

In Chapters 4 and 5, our simulations were set-up such that the SRS EPW was always in the kinetic regime (characterised in this thesis by $k_{\mathrm{EPW}}\lambda_D \geq 0.25$). This meant that the most important contributions to the non-linear evolution of the EPW, and therefore the SRS instability, were the kinetic non-linear frequency shift and the non-linear reduction in Landau damping [Kline et al., 2006]. In this chapter, we consider a wide range of $k_{\mathrm{EPW}}\lambda_D$ values, such that the dominant non-linear effect is different in each case. Referring to Figure 2.5, we see that, as we move to a regime where $k_{\mathrm{EPW}}\lambda_D < 0.25$, the decay of the SRS EPW into another EPW and an IAW, via the Langmuir decay instability (LDI), becomes important.

Before beginning our literature review proper, we revise the theory of an electron trapped in an electron plasma wave under the influence of a perpendicular magnetic field. It is this basic idea which underlies the effects of a magnetic field on kinetic SRS. Following Dawson et al. [1983], consider an electron trapped in an electron plasma wave of the form $\vec{E} = E_0 \sin(kx - \omega t)\hat{x}$, propagating perpendicular to an external magnetic field $\vec{B} = B_0\hat{z}$. In the wave frame, the electron has velocity $\vec{v} = (v_x + v_{ph})\hat{x} + v_y\hat{y} + v_z\hat{z}$ and equations of motion

$$\frac{dv_x}{dt} = -\frac{eE_0}{m_e}\sin(kx) - \omega_c v_y, \tag{6.1}$$

$$\frac{dv_y}{dt} = \omega_c(v_x + v_{ph}). \tag{6.2}$$

Where $\omega_c = eB_0/m_e$ is the cyclotron frequency and $v_{ph} = \omega/k$ is the EPW phase velocity. Taking the derivative with respect to time of Equation 6.1, and substituting in Equation 6.2 gives

$$\frac{d^2v_x}{dt^2} = -\left[\omega_c^2 + \frac{eE_0k}{m_e}\cos(kx)\right]v_x - \omega_c^2 v_{ph}. \tag{6.3}$$

This describes the oscillation of v_x, at a spatially-dependent frequency

$$\omega_B(x) = \left[\omega_c^2 + \frac{eE_0k}{m_e}\cos(kx)\right]^{1/2}, \tag{6.4}$$

around an average value

$$\langle v_x \rangle_{1/\omega_B} = -\frac{\omega_c^2}{\omega_B^2} v_{ph}. \tag{6.5}$$

Since the average v_x is non-zero and negative, in the wave frame, the electron will fall behind the wave and eventually become de-trapped. In the case of stimulated Raman scattering, the electrons interact with two electromagnetic waves as well as many electron plasma waves, which makes their behaviour more complicated.

6.1.1 Magnetic fields suppress kinetic SRS

In a 2018 paper, Winjum et al. [2018] showed that applying a magnetic field perpendicularly to SRS EPWs can "quench" the SRS instability in the kinetic regime. They consider parameters where $\omega_c/\omega_{pe} \ll 1$, and the EPW Landau damping rate is less than the trapped-electron bounce frequency. Furthermore, all of their simulations are performed in the kinetic regime where trapped particles in the EPW modify the electron plasma wave dispersion such that the damping rate tends to zero. Winjum et al. [2018] use 1D and 2D PIC simulations to show that applied magnetic fields can increase the inflationary SRS threshold, and suppress the reflectivity due to iSRS which is driven significantly above threshold.

A 2021 paper by Zhou et al. [2021] uses 1D and 2D PIC simulations to show that a moderate ($\omega_c \ll \omega_{pe}$) external magnetic field can suppress inflationary SRS, so that the SRS reflectivity stays at its convective saturation level from fluid theory. They consider $k_{\mathrm{EPW}}\lambda_D$ in the range $[0.28, 0.46]$, driven by an incident laser intensity of $I_0 = 2 - 5 \times 10^{15}\mathrm{W/cm}^2$, for an external magnetic field between zero and 90T. They force the SRS to grow from a fixed resonance point by firing in an electromagnetic seed wave from the right-hand boundary, with $I_s/I_0 = 2 \times 10^3$. They find that the SRS-reflectivity approaches zero asymptotically for $B_{\mathrm{ext}} > 60\mathrm{T}$, this is explained in terms of a shutting-off of the autoresonance since the non-linear frequency shift is suppressed, and cannot compensate for the wave-number shift arising from amplification up the density gradient Zhou et al. [2021].

The first step of this research project was to replicate the results of Winjum et al. [2018], in order to benchmark the EPOCH code against the results from OSIRIS and to understand the relevant diagnostics. Figure 6.1 demonstrates the main results of replicating Winjum et al. [2018]. The 1D PIC simulations summarised in Figure 6.1 model homogeneous convective SRS in the kinetic regime, with and without a 30T magnetic field perpendicular to the EMW and EPW propagation. By comparing the left ($B_{\mathrm{ext}} = 0\mathrm{T}$) and right ($B_{\mathrm{ext}} = 30\mathrm{T}$) columns of Figure 6.1, we see two key features of the simulation: sub-figures (a) and (b) show that the convective growth of SRS EPWs is suppressed by the magnetic field; sub-figures (c) and (d) show that the population of electrons trapped in the SRS EPWs becomes de-trapped by the magnetic field. Examination of the time-resolved p_x, p_y distribution functions (not included here) shows that the magnetic field introduces a *periodic* disturbance to the electron trapping.

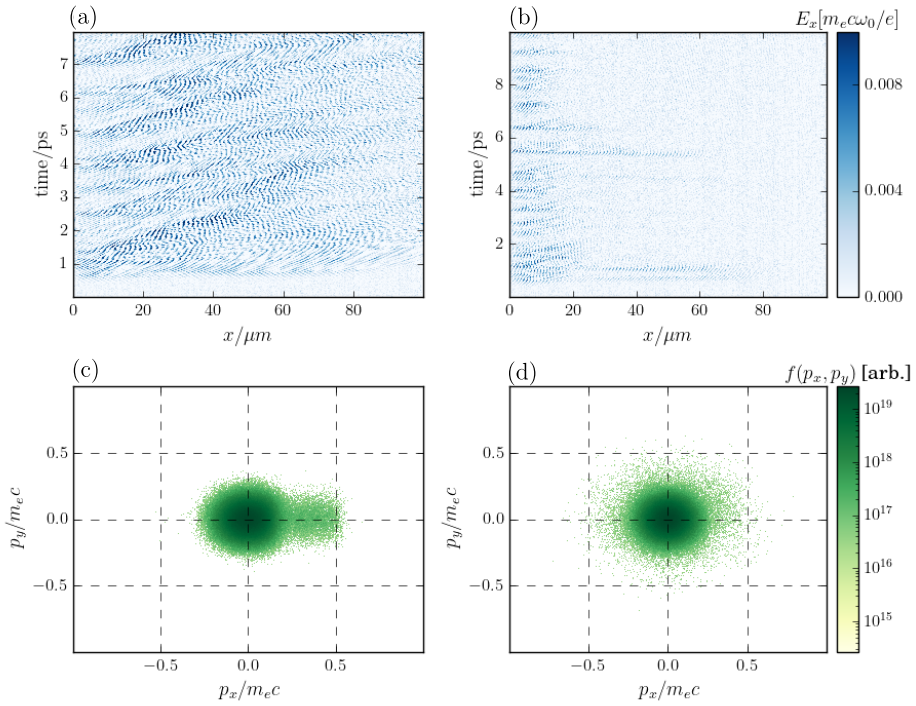

Figure 6.1: The first row (sub-figures a,b) shows the electrostatic (E_x) fields as a function of space and time. The second row (sub-figures c,d) shows the p_x, p_y distribution functions averaged over space, at $t = T_{\text{end}}$. Simulation parameters chosen for comparison with Figure 2b of Winjum et al. [2018].

6.1.2 Magnetic fields affect SRS/SBS balance.

Using a five-wave interaction model, Vyas et al. [2016] find that the back-reflectivity of stimulated Raman or Brillouin scattering is significantly affected by the presence of the other instability in a magnetic field. They consider the case of an extraordinary electromagnetic wave ($\vec{E}_l \perp \vec{B}_0$) propagating perpendicular to the static background magnetic field. Using the hydrodynamic equations of motion, they derive gain coefficients for the pump wave (laser), SRS scattered EMW, and the SBS scattered EMW. They consider a laser intensity of $I_0 = 5 \times 10^{15}\text{W/cm}^2$ and magnetic fields of $0, 50, 100$T and find that as the strength of the magnetic field increases, the back-reflectivity of SBS decreases, while the back-reflectivity of SRS increases [Vyas et al., 2016].

The decrease in SBS back-reflectivity is not explained in Vyas et al. [2016], and is not clearly explained elsewhere in the literature. In fact, Bawa'aneh [2006] find that, for a fixed laser intensity, the SBS growth rate of an extraordinary mode in a homogeneous, magnetised plasma is *increased* above the non-magnetised growth rate (Equation 2.33) for magnetic fields and plasma densities satisfying $\omega_c \leq 0.25\omega_{pe}$.

6.2 Modelling SRS on LULI

At the time of writing, the results of the following experiment have not been published in any peer-reviewed journal. They were, however, described at the 42nd EPS Conference on Plasma Physics by Marquès et al. [2015]. Briefly, the experiment aimed to investigate high-power laser propagation and plasma coupling in low-density magnetized plasmas. In the experiment, the interaction beam interacts with a pre-ionised hydrogen gas jet which is contained within a homogeneous and steady (compared to plasma scales) 20T magnetic field. In this section, we focus on work performed by the author which attempts to explain the SRS signals measured in the experiment.

6.2.1 Experimental results

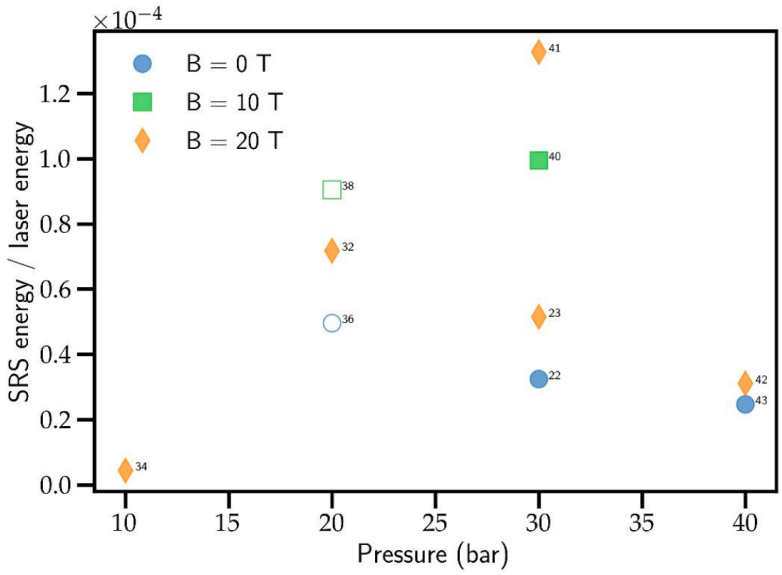

Figure 6.2: **Figure produced by M. Bailly-Grandvaux.** Experimentally-measured SRS energy at different gas jet pressures, with and without magnetic fields. The solid-coloured markers represent shots with the vertical laser polarisation and the un-filled markers represent horizontal polarisation of the laser. The external magnetic field has vertical orientation.

Figure 6.2 shows the energy in backward SRS scattered light as a fraction of the incident laser energy, as a function of the gas-jet pressure. Each datapoint represents a different shot (shot numbers appear next to the marker), and the dataset is rather incomplete. This reflects the fact that SRS and SBS measurements were a secondary objective of the experiment. Two key things to note are that the SRS level is very low (on the order of $10^{-4} I_0$), and that there appears to be a trend of increased SRS scattered light with the external magnetic field compared to the shots without, for shots with horizontal and vertical laser polarisations. This is in apparent contradiction to Winjum et al. [2018], which shows that an external magnetic field should act to suppress SRS in

the kinetic regime. It was this apparent contradiction which inspired us to re-examine the SRS signals collected in the experiment.

In order to study these results using PIC, we required first that the gas jet pressures be converted into plasma densities. This proved not to be straightforward, as the quoted plasma densities from pre-shot calibration were a factor of 10 higher than those inferred from analysis of interferometry performed on each shot. As such, we chose to simulate plasma densities across one order of magnitude, choosing $n_e \in \{0.01, 0.025, 0.05, 0.10, 0.15\}\, n_{\mathrm{cr}}$, based on a combination of the interferomtry and FLASH simulations performed by Adam Higginson (without an external magnetic field). Electron temperatures in the fully ionised portion of the jet were also taken from Higginson's FLASH simulations. The ionic species was chosen to be protons, in order to reduce the simulation time, and their temperature was one-third of the electron temperature for all densities.

6.2.2 Simulation results

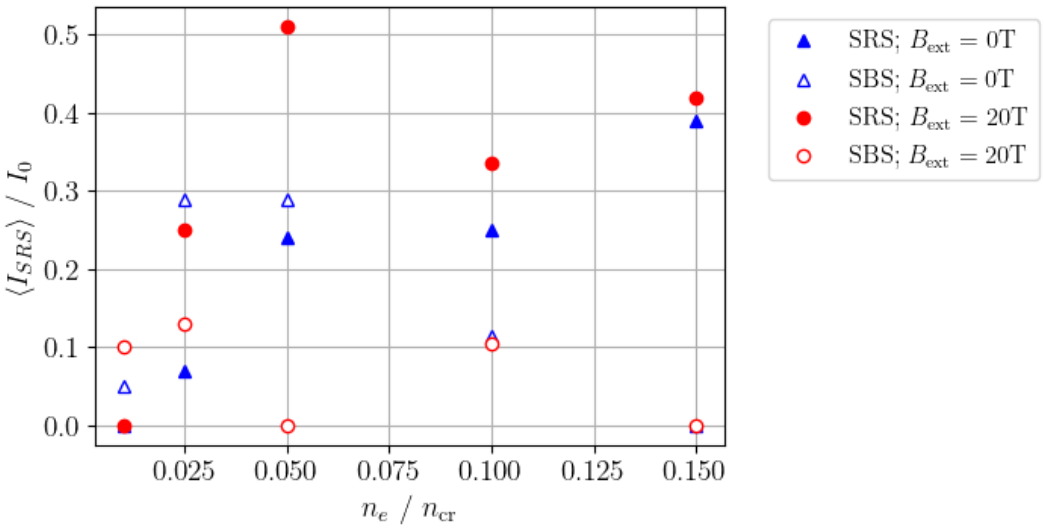

Figure 6.3: Reflected light from SRS and SBS (averaged over full simulation time) as a function of the initial homogeneous plasma density. Plasma densities and temperatures taken from FLASH simulations of single-beam shots without magnetic fields.

We used the EPOCH PIC code to simulate the interaction between the laser, an externally applied magnetic field, and the plasma. The simulation parameters common to all simulations are: $\lambda_0 = 1053$nm ($\omega_c/\omega_0 = 0.002$); $L_x = 1000$µm; $I_0 = 0.9\times10^{15}$W/cm^2; $T_{\mathrm{end}} = 10$ps; 1000 PPC (from convergence testing on $\langle I_{\mathrm{SRS}} \rangle_{t>0}$); $\vec{B}_{\mathrm{ext}} = 20\mathrm{T}\hat{z}$. The laser is polarised in the y direction, so has its magnetic component parallel to the background magnetic field. Table 6.1 shows the plasma density and temperature for the five LULI-inspired simulations, as well as $k_{\mathrm{EPW}}\lambda_D$ for primary and secondary backward SRS in each case. There is significant uncertainty in how well the chosen simulation

parameters actually reflect the experimental conditions, due to circumstances outside of this author's control.

n_e / n_{cr}	T_e / eV	ω_c / ω_{pe}	$k_{\mathrm{EPW}}\lambda_D$ (1)	$k_{\mathrm{EPW}}\lambda_D$ (2)
0.01	180	0.019	0.36	0.30
0.025	450	0.011	0.34	0.26
0.05	600	0.008	0.27	0.18
0.10	900	0.006	0.21	0.10
0.15	1100	0.005	0.18	n/a

Table 6.1: Plasma conditions taken from FLASH simulations performed by Adam Higginson, without external magnetic fields. For all simulations, the electron and ion densities are equal and the ion temperature is one-third of the electron temperature. $k_{\mathrm{EPW}}\lambda_D$ (1) refers to SRS backscatter, and is calculated from fluid theory without considering the effect of the magnetic field on the EPW dispersion. $k_{\mathrm{EPW}}\lambda_D$ (2) is calculated for re-scatter SRS under the same assumptions.

Figure 6.3 shows the time-averaged reflectivity from SRS and SBS as a function of the simulation plasma density. Focussing first on the SRS measurements (filled-in markers) we see increases on the order of 100% in the reflectivity with the 20T field for the $0.025, 0.50, 0.10 n_{\mathrm{cr}}$ densities. From this point on, we will consider only these three densities. By comparing these three cases in detail, we find that the effect of the magnetic field on the backward-SRS reflected light in one dimension depends on a combination of four factors:

1. Decreased stimulated Brillouin scattering (SBS) leaves more laser energy to undergo SRS (as in Vyas et al. [2016]).
2. Decreased non-linear frequency shift of electron plasma waves enhances the SRS resonance (as proposed in Winjum et al. [2021]).
3. Decreased re-scatter of SRS means that more SRS-scattered light reaches the left boundary where reflectivity is calculated (as proposed by Lee et al. [2021]).
4. Decreased forward-scatter SRS (fSRS) leaves more laser energy to undergo backward SRS.

Table 6.2 includes a description of how each of these factors changes for the 2.5%, 5%, and 10% critical density simulations. We now examine each of these factors in turn, in order to explain the increased reflectivity measured in our simulations.

Reduced SBS

Examining the SBS data (un-filled markers on Figure 6.3), we see that for the $0.025 n_{\mathrm{cr}}$ and $0.50 n_{\mathrm{cr}}$ cases the increase in SRS with the applied magnetic field is accompanied by

	$n_e = 2.5\% n_{cr}$	$n_e = 5\% n_{cr}$	$n_e = 10\% n_{cr}$
bSRS	250% increase with B	75% increase with B	35% increase with B
SBS	Decrease with B	Decrease with B	No change
fSRS	Decrease with B	Decrease with B	Decrease with B
Re-scatter	n/a	Decrease with B	No change
$\delta\omega_{NL}$	Decrease with B	Decrease with B	Decrease with B

Table 6.2: Changes to behaviour of SBS, forward-SRS, re-scatter SRS, and the non-linear EPW frequency shift for the LULI-inspired simulations which showed *increased* backward SRS with an applied magnetic field.

a decrease in the level of SBS. Inspection of the time-resolved reflectivities in Figure 6.4 (b) shows this result more starkly. The initial linear growth of SRS is the same for the cases with (red line) and without (blue line) the magnetic field. However, the growth of SBS is greatly suppressed by the applied magnetic field (red dashed line). This reduced SBS scattering leaves more laser energy available to undergo SRS. This is particularly evident in sub-figure (a) for times greater than 8ps, where the increase in SBS for the un-magnetised case is accompanied by a *decrease* in the amount of SRS. This finding is an extension of the result found using a fluid-theory five-wave interaction model by Vyas et al. [2016], as it shows that the effect of the magnetic field on co-existing SRS and SBS is qualitatively the same in the kinetic regime.

Reduced non-linear frequency shift

In the previous two Chapters, the nonlinear frequency shift of electron plasma waves arising from kinetic effects was responsible for enhanced growth of SRS, above the level predicted by fluid theory, via autoresonance. However, in these simulations the nonlinear frequency shift seems to work to de-tune the SRS resonance and limits its convective gain. When the magnetic field is applied, it reduces the nonlinear frequency shift by de-trapping electrons from the EPW. Figure 6.6 shows the effect of the magnetic field on the non-linear frequency shift of the SRS EPWs. The sub-figures in the left (right) column show two-dimensional Fourier transforms of the E_y (E_x) fields averaged over k-space and normalised to their maximum value. The plasma density and temperature parameters, which are inherited from modelling of the LULI experiment, are such that the forward and backward scattered EMWs have very similar frequencies for all three simulations.

Figure 6.6 sub-figure (a) is the E_y spectrum for the simulation with $n_e = 0.025 n_{cr}$, which sees a 200% increase in the SRS-reflectivity with a 20T magnetic field. Looking at the red line ($B_0 = 0$T), the spectral feature at 1 is the laser, and the feature in the range $0.8 - 0.9\omega_0$ is backward-scattered SRS light. We can see the corresponding SRS electron plasma waves in sub-figure (b) in the range $0.1 - 0.19\omega_0$. From fluid theory, we expect to see backward and forward SRS EPW signals in the range $0.16 - 0.19\omega_0$, so it is clear that

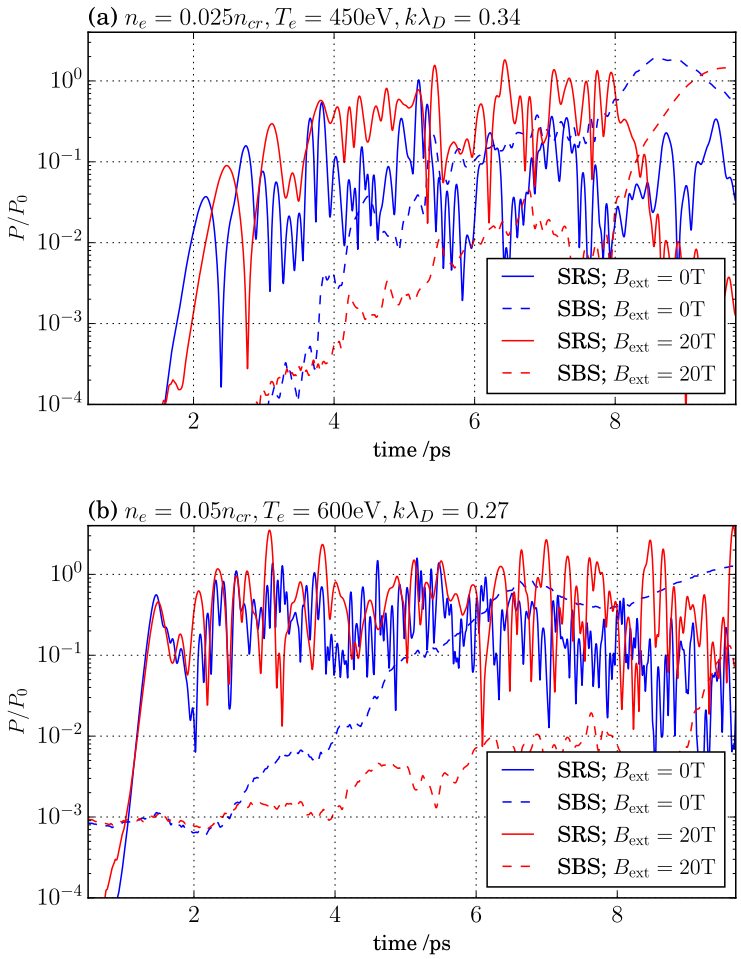

Figure 6.4: Time-resolved reflectivities ($I_0 = 0.9 \times 10^{15}\text{W/cm}^2$) from SBS (dashed lines) and backward SRS (solid lines) with external magnetic fields $B = 0\text{T}$ (blue), and $B = 20\text{T}$ (red).

the electron plasma waves have undergone significant non-linear frequency downshift in the case with zero magnetic field. The corresponding up-shift can be seen in Figure (a), for the simulation with no external magnetic field. The black lines on sub-figures (a) and (b) show significantly narrower frequency spectra for the same simulation with a 20T magnetic field applied. This result supports the finding of Winjum et al. [2021] that an external magnetic field reduces the non-linear kinetic frequency shift of EPWs.

Since these simulations are driven very near the threshold for iSRS, the relative importance of the decreased frequency shift and the decreased SBS is difficult to untangle. Future work will include repeating the simulations without mobile ions, in order to unpick these two effects for the $2.5\%n_{cr}$ case.

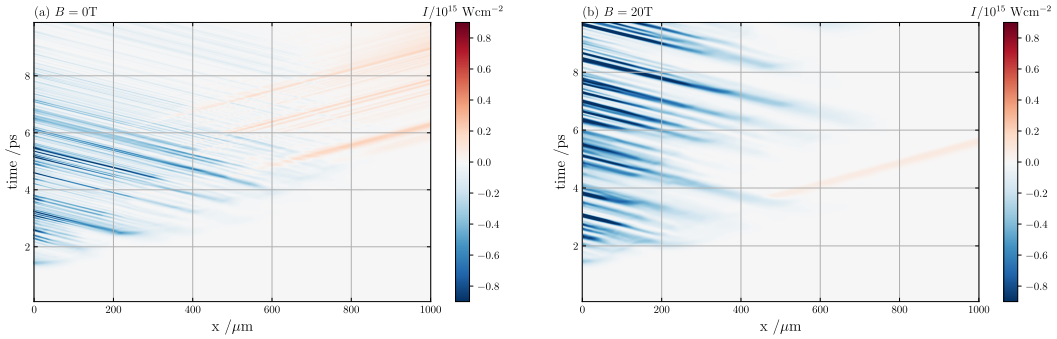

Figure 6.5: Poynting flux of scattered light as a function of space and time. Backward-travelling signal represents light scattered by backward SRS of the laser. Forward-travelling signal represents secondary back-scatter (re-scatter) of the primary backward-scattered light. Simulation parameters: $n_e = 0.05 n_{cr}$; $T_e = 600$eV; $k_{\text{EPW}}\lambda_D = 0.27$ for primary back-scatter SRS EPW.

Reduced re-scatter

In this thesis, re-scatter SRS refers to the phenomenon of backward-scattered SRS light which undergoes backward SRS. It satisfies the following matching conditions in 1D:

$$\begin{aligned} \omega_0 &= \omega_{s1} + \omega_{EPW1}, k_0 = -k_{s1} + k_{EPW1} \\ \omega_{s1} &= \omega_{s2} + \omega_{EPW2}, -k_{s1} = +k_{s2} - k_{EPW2}, \end{aligned} \tag{6.6}$$

where the first row is the primary backward SRS of the incident laser (ω_0, k_0) and the second row is backward SRS of the scattered primary light wave $(\omega_{s1}, -k_{s1})$. The effects of re-scatter SRS in ICF have been examined in works by Winjum et al. [2013] and Ji et al. [2021], which used 1D and 2D PIC simulations to show that backward-SRS (bSRS) of backward-SRS scattered light can generate suprathermal electrons with energies greater than 100keV. Ji et al. [2021] also suggest that re-scattering of the backward-scattered SRS light might lead to artificially low measurements of bSRS in simulations and experiments.

Inspection of Figure 6.5 shows that forward-scattered light from rescatter is greatly suppressed by the magnetic field. This means that more of the light scattered by primary bSRS is able to reach the left boundary where it is measured.

Reduced forward scatter SRS

Inspection of Figure 6.6 sub-figures (b), (d) and (f) shows that the largest EPW signal for all three simulations without the magnetic field is double-peaked. The lower frequency (left-most) peak corresponds to forward-scatter SRS, and the higher frequency peak corresponds to backward-scatter SRS (based on the matching conditions from fluid theory). For the simulations with an applied 20T magnetic field, however, the largest EPW signal has only one peak, which is at the frequency corresponding to backward SRS ($0.19, 0.25, 0.34\omega_0$ for the $2.5\%, 5\%, 10\% n_{cr}$ cases, respectively).

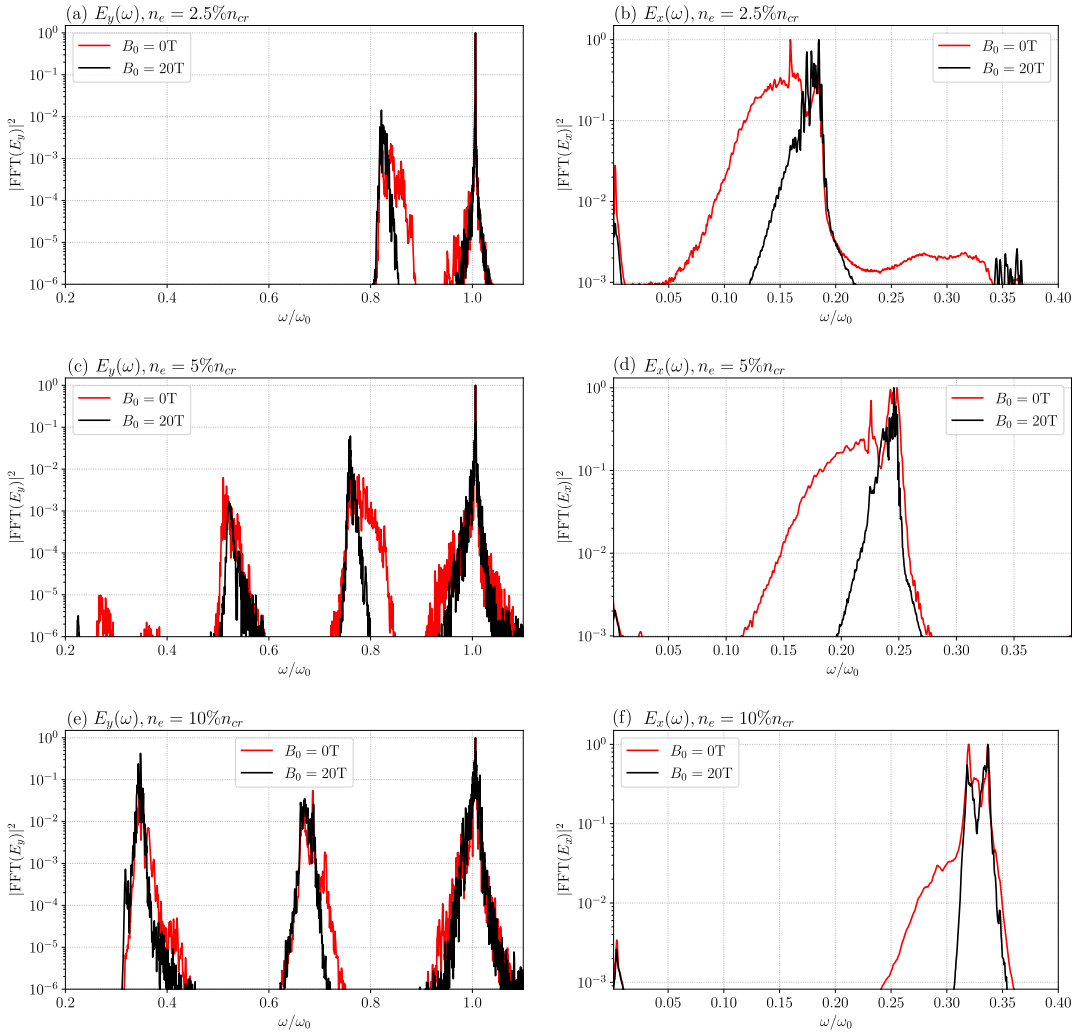

Figure 6.6: 2D Fourier transforms of E_x, E_y fields, averaged over k-space, for three densities which show the largest increase in time-integrated SRS-reflectivity with the addition of the external magnetic field. Each signal is normalised to its own maximum value.

6.2.3 Conclusion

In this section we reported the results of simulations performed by the author while employed as a Junior Specialist at the University of San Diego. They were responsible for PIC modelling of the SRS behaviour in pre-ionised, homogeneous, externally magnetised plasmas from an experiment performed at LULI. The experiment showed an increase in the measured back-scattered light from SRS with an applied magnetic field, and this is recreated in our simulations. Several potential explanations for the increased back-scattered SRS light are observed in the simulations, including: a change in the balance between stimulated Raman and Brillouin scatterings; decreased non-linear frequency shift of EPWs; decrease re-scatter SRS; decreased forward-scatter SRS. It is clear that, while these simulations are limited to one dimension, they nonetheless contain

a wide range of interacting scattering phenomena which all contribute to the measured backward-SRS behaviour. In a real experiment, the contribution of the magnetic field to the SRS behaviour is even harder to unpick, and may include factors such as: increased electron temperature; disrupted inter-speckle communication [Yin et al., 2013]; and changes to the Langmuir decay instability (which could not be sufficiently resolved in these simulations).

While the SRS observed in the experiment was never considered significant enough for publication, it did lead to a second project of more fundamental interest: the problem of how the effect of the magnetic field varies with $k_{\mathrm{EPW}}\lambda_D$. This question is considered in the next section.

6.3 Magnetic field effect varies with plasma debye length

This investigation is an extension of the author's research project at UCSD, inspired by the accidental scan over $k_{\mathrm{EPW}}\lambda_D$ performed while modelling the LULI experiment. In this work, we examine, via a more granular parameter scan, how the effect of the external magnetic field on SRS depends on $k_{\mathrm{EPW}}\lambda_D$.

This work was performed in collaboration with Ben Winjum (University of California, Los Angeles) and Simon Bolaños (University of California, San Diego), and will be presented by Ben Winjum at the APS DPP meeting in November 2021 [Winjum et al., 2021]. Spencer, Winjum and Bolaños designed the parameter space together, and each performed parameter scans at different laser intensities and with different PIC codes. This section presents Spencer's preliminary investigation into the parameter space.

6.3.1 Simulation parameters

Electron temperatures are chosen in the range $0.5 - 3.0$keV and $k_{\mathrm{EPW}}\lambda_D$ in the range $0.20 - 0.40$. Densities are calculated from these two values, such that the matching conditions with fluid dispersion relations are satisfied. The density profile has a slight linear density gradient, between $0.98n_0$ and $1.02n_0$, in order to suppress the growth of forward-SRS. This is equivalent to a density scale length of 2500µm at the centre of the box. We model a 351nm laser, polarised in the y-direction. We compare two incident laser intensities: $I_0 = 1 \times 10^{15}\mathrm{W/cm^2}$ and $I_0 = 3 \times 10^{15}\mathrm{W/cm^2}$, which sit near the threshold for inflationary SRS estimated from Vu et al. [2007]. We use 512 particles per cell and the simulations run to 5ps. The simulation domain was approximately the length of the central portion of an $f/8$ speckle, $5f^2\lambda_0 \simeq 100$µm. For this preliminary investigation, we treated the ions as an immobile neutralising background, in order to remove the complicating factors of stimulated Brillouin scattering and the Langmuir decay instability.

6.3.2 Results

We begin by considering the lower intensity case, where $I_0 = 1 \times 10^{15}\text{W/cm}^2$. Figure 6.7 shows three heat-maps; sub-figures (a) and (b) are the time-averaged intensity of light back-scattered through SRS, as a percentage of the constant incident laser intensity. The black stepped line separates the domain into two regions: above the black line the electron density satisfies $n_e > 0.11$, and below it $n_e \leq 0.11$. In this lower section of the domain, the matching conditions for re-scatter SRS can be satisfied ($n_e < n_{cr}/9$). Sub-figure (c) shows the percentage difference $\left(\langle I_{SRS}\rangle_{40\text{T}} - \langle I_{SRS}\rangle_{0\text{T}}\right)/\langle I_{SRS}\rangle_{0\text{T}}$, so that negative values represent decreased SRS after applying the magnetic field. Inspection of Figure 6.7 (c) shows that applying the 40T magnetic field leads to at least 15% decrease in bSRS reflectivity for $0.25 \leq k_{\text{EPW}}\lambda_D \leq 0.3$. The effect is most dramatic for the simulations with $k_{\text{EPW}}\lambda_D = 0.30$, where the magnetic field leads to almost complete suppression of bSRS, regardless of the electron temperature. This is in good agreement with Winjum et al. [2018]. There are several simulations with $k_{\text{EPW}}\lambda_D > 0.325$ and $n_e < n_{cr}/9$ which have large ($> 15\%$) positive changes to the bSRS reflectivity with an applied field. We do not consider these cases to be robust examples of enhancement, since the absolute levels of bSRS scattered light reported in sub-figures (a) and (b) are on the level of noise ($\langle I_{SRS}\rangle \simeq 10^{-4} I_0$). This parameter scan showed no evidence of the enhanced SRS measured in the LULI experiment or our modelling of it, as seen in the the previous section.

We decided to perform the scan again, this time driven with an incident laser intensity of $I_0 = 3 \times 10^{15}\text{W/cm}^2$, in order to see whether we could identify a regime where the enhancing effects identified in the previous section (reduced re-scatter; reduced forward SRS; and reduced non-linear frequency shift) came into effect. Figure 6.8 shows the results of this scan, presented in the same manner as Figure 6.7. Examining Figure 6.8 sub-figure (c), we notice two immediate differences from the case with a lower laser intensity. Firstly, the region which sees maximum suppression of SRS with the magnetic field has shifted to $k_{\text{EPW}}\lambda_D = 0.35$ from $k_{\text{EPW}}\lambda_D = 0.3$ in the Figure 6.7. This can be attributed to the fact that SRS is growing in the strongly kinetic regime, and is driven *well above* the threshold for inflationary SRS, leading to higher levels of SRS when $B_0 = 0\text{T}, I_0 = 3.0 \times 10^{15}\text{W/cm}^2$. This inflationary SRS is strongly suppressed by the application of the magnetic field, since it de-traps the electrons which are responsible for the kinetic inflation [Winjum et al., 2018]. Secondly, we notice that there are several simulations with $k_{\text{EPW}}\lambda_D \leq 0.25$ where the magnetic fields leads to a large *enhancement* of SRS. All of these cases sit below the re-scatter line, and as such this could be attributed to reduced re-scatter, as we saw in some of the LULI simulations.

6.4 Conclusion

In this chapter we considered stimulated Raman scattering, in homogeneous plasmas well below quarter critical density, which develops under the influence of a perpendicular magnetic field. Previous simulations in the strongly kinetic regime ($k_{\mathrm{EPW}}\lambda_D \geq 0.3$) had found that applying a magnetic field perpendicular to the SRS electron plasma waves could suppress the growth of iSRS to the level predicted from fluid theory [Winjum et al., 2018; Zhou et al., 2021]. In Section 6.2, we performed simulations which appeared to contradict this theory, measuring a 250% increase in the reflectivity from backward SRS for the simulation with $k_{\mathrm{EPW}}\lambda_D = 0.34$. A simulation in the weakly kinetic regime ($k_{\mathrm{EPW}}\lambda_D = 0.27$) showed a 75% increase in the light reflected by bSRS with an applied magnetic field. These results do not contradict the literature, rather they extend it to the case of kinetic SRS which competes with SBS; backwards re-scatter; and forward SRS. We performed a parameter scan of 1D SRS simulations with fixed ions which examined the effect of an applied perpendicular magnetic field on backward SRS for $0.2 \leq< k_{\mathrm{EPW}}\lambda_D \leq 0.4$ and with immobile ions. We found that, in most of the parameter space, a perpendicular magnetic field acts to suppress backward SRS. However, in the lower end of the $k_{\mathrm{EPW}}\lambda_D$ range, there were cases where SRS was enhanced above its non-magnetised value. The next step would be to repeat these scans with mobile ions, to see how SBS and LDI affect the measured backward SRS.

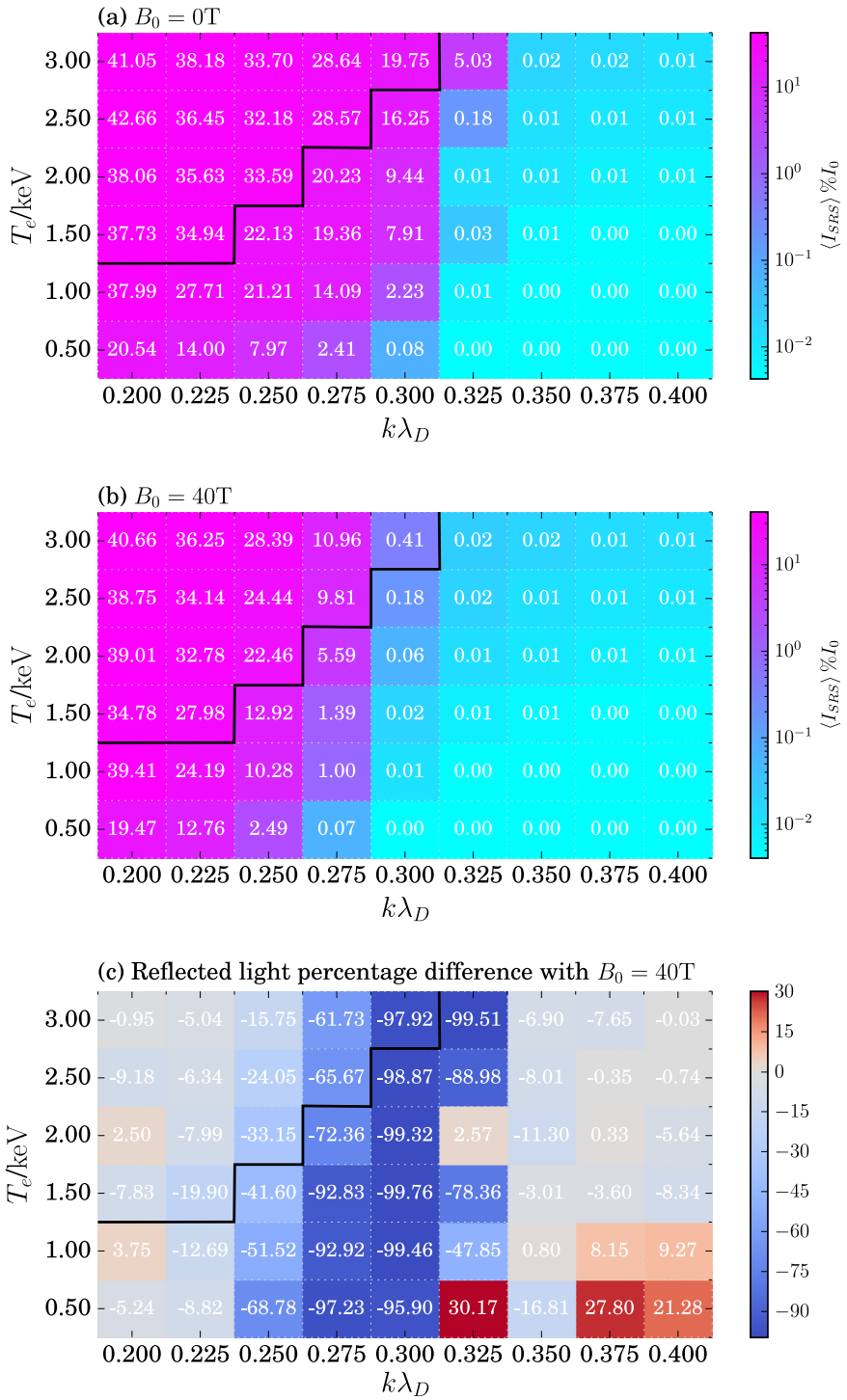

Figure 6.7: Sub-figures (a) and (b) show the time-averaged intensity of backward SRS-scattered light, as a function of electron temperature and $k_{\mathrm{EPW}}\lambda_D$ for the primary SRS electron plasma wave, for the scans without (a) and with (b) a 40T applied magnetic field. Time-averaged intensity is reported as a percentage of the incident laser intensity $I_0 = 1.0 \times 10^{15}\mathrm{W/cm^2}$. Sub-figure (c) shows the difference between the reflected light without an external magnetic field and the reflected light with the applied field, as a percentage of the un-magnetised result.

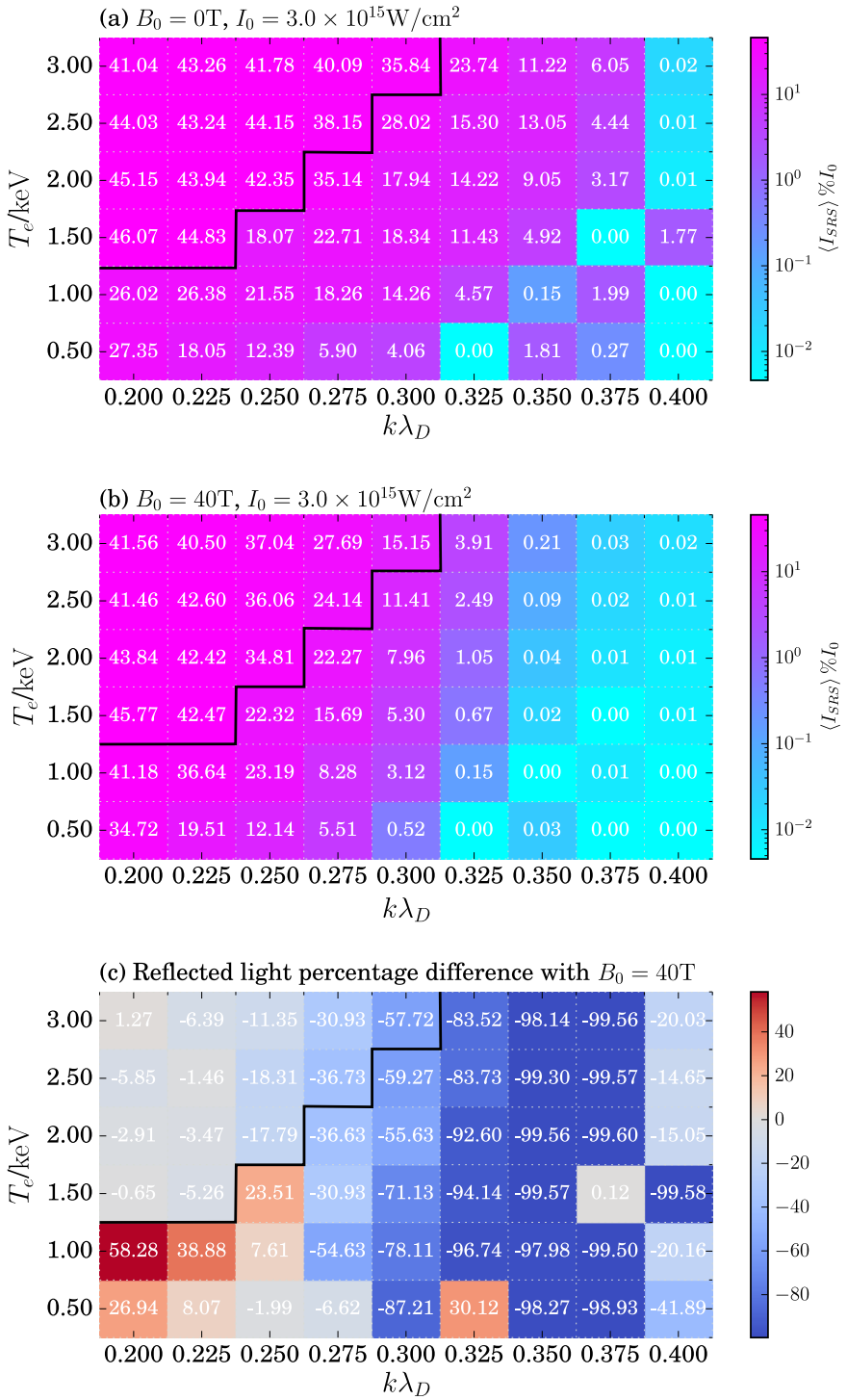

Figure 6.8: Sub-figures (a) and (b) show the time-averaged intensity of backward SRS-scattered light, as a function of electron temperature and $k_{\mathrm{EPW}}\lambda_D$ for the primary SRS electron plasma wave, for the scans without (a) and with (b) a 40T applied magnetic field. Time-averaged intensity is reported as a percentage of the incident laser intensity $I_0 = 3.0 \times 10^{15}\mathrm{W/cm}^2$. Sub-figure (c) shows the difference between the reflected light without an external magnetic field and the reflected light with the applied field, as a percentage of the un-magnetised result.

Chapter 7

Conclusions and Future Work

In this thesis, we presented particle-in-cell simulations of inflationary SRS relevant to direct-drive inertial confinement fusion. The three pieces of original work considered iSRS first in isolation from other instabilities (Chapter 4); then in realistic plasma profiles with competition from re-scatter and forward-SRS (Chapter 5); and finally in magnetised plasmas with mobile ions, where the iSRS instability was in competition with re-scatter SRS, forward-SRS, and stimulated Brillouin scattering (Chapter 6).

7.1 Conclusions

In Chapter 4, we isolated inflationary SRS in 100µm long sections of representative shock-ignition plasma coronas. By calculating the intensity of backward-scattered light, and comparing the level to that predicted from fluid convective growth theory, we studied how the iSRS threshold varied with the density scale length of the plasma, and with the density at which iSRS was excited. The paper resulting from this work ([Spencer et al., 2020]) has received citations which use many different results of the work, including: the dependence of the SRS threshold on the PNRG seed in a PIC code; the simple fluid model used to define the threshold; and the evidence of iSRS across various SI density scale-lengths.

In Chapter 5, we aimed to extend the results of Spencer et al. [2020] to look at how the inflationary SRS threshold changes when driven by realistic broadband lasers. We first extended the results of Zhao et al. [2019], and showed that a decoupled broadband laser can be constructed to suppress the growth of inflationary SRS, if the non-linear frequency shift of the scattered waves is taken into account. We then applied the theory of Wen et al. [2021] to inflationary SRS in a shock-ignition coronal plasma driven by a laser with 1THz of SSD-type bandwidth. We found no increase in the threshold, compared to the monochromatic laser driver. Finally, we simulated the inflationary SRS threshold for shock-ignition on the argon fluoride laser currently under development at the Naval Research Laboratory. We found that, for a monochromatic driver, the intensity threshold for iSRS was between $3.5-4\times10^{15}\mathrm{W/cm^2}$. However, when we added

10THz of bandwidth to the driver, we could not define a threshold to compare with. Currently, no conclusions can be drawn about the effects of realistic laser bandwidth on inflationary SRS in shock-ignition.

In Chapter 6 we presented modelling inspired by a magnetised LPI experiment performed on the LULI laser system. The experiment measured increased levels of backward SRS with the application of a perpendicular magnetic field. This increase was recreated in 1D PIC simulations, and explained in terms of a changing energy balance between: backward SRS; forward SRS; stimulated Brillouin scattering and re-scattered backwards SRS. These simulations ranged from SRS behaviour which was dominated by kinetic effects (inflationary SRS) to SRS dominated by fluid effects. This informed the second part of the study, which simulated backward SRS with electron plasma waves satisfying $0.2 \leq k_{\mathrm{EPW}}\lambda_D \leq 0.4$ and electron temperatures $0.5 \leq T_e \leq 3\mathrm{keV}$; this time with immobile ions to reduce the number of scattering phenomena in each simulation. This preliminary investigation identified a region of that parameter space where the magnetic field enhances backward SRS.

As we laid out in the Introduction, inflationary SRS is now becoming recognised as a major threat to shock-ignition ICF. It has been identified in experiments [Cristoforetti et al., 2021; Scott et al., 2021] and in particle-in-cell simulations [Seaton and Arber, 2020; Spencer et al., 2020] as the main source of back-scattered SRS light when the incident laser intensity is near the iSRS threshold. The simulations presented in this thesis contribute to our understanding of SRS in shock-ignition and other directly-driven ICF schemes, and suggest some interesting avenues for further study.

7.2 Future Work

There are several avenues that this research could be taken down, depending on the desired application of the final results. For example, if one wished to really unpick the effect of different types of broadband on inflationary SRS in shock-ignition plasma corona, this thesis has shown that it would be best to *reduce* the realism of the simulation, perhaps by using a seed EMW. In this case, one could examine in detail the effect of different broadband light structures on the evolution of a single autoresonant mode. These results could then be added onto a fluid LPI model (which we know can model the effect of broadband on fluid-convective and absolute SRS) as in Tran et al. [2020].

On the other hand, there are many cases where *more* realistic modelling of inflationary SRS would be interesting. For example, the scaling of the iSRS threshold with collisions, and an attempt to derive a predictive model for the iSRS threshold in an inhomogeneous plasma, similar to Vu et al. [2007]'s result for homogeneous coronal plasmas. Realistic collisions would change the iSRS threshold for shock-ignition in two ways: firstly, collisional damping of the electromagnetic waves, would change the transition from fluid-convective to inflationary growth; and secondly, collisions could act to de-trap electrons from the SRS electron plasma waves.

As more full-scale shock-ignition experiments are performed, modelling inflationary SRS in two dimensions, with realistic laser speckle patterns will become more important. These simulations will include many more effects which contribute to measured iSRS in experiments, such as: side-scatter SRS (inflationary or fluid-convective) and inter-speckle seeding.

Finally, as more magnetised LPI experiments are performed, PIC simulations of kinetic SRS will be able to contribute towards unpicking the energy balance between various scattering instabilities. The magnetised behaviour of stimulated Brillouin scattering, forward SRS, and re-scatter SRS are not well-understood or even considered in the literature. The work presented in Chapter 6 of this thesis, will contribute to at least two new papers on the topic of magnetised stimulated Raman scattering, prepared in collaboration with UCSD and UCLA, which will hopefully inspire increased interest in this problem.

Appendix A

License Agreements

SPRINGER NATURE LICENSE
TERMS AND CONDITIONS

Aug 12, 2021

This Agreement between SJ Spencer ("You") and Springer Nature ("Springer Nature") consists of your license details and the terms and conditions provided by Springer Nature and Copyright Clearance Center.

License Number	5126540383962
License date	Aug 12, 2021
Licensed Content Publisher	Springer Nature
Licensed Content Publication	Nature Physics
Licensed Content Title	Inertial-confinement fusion with lasers
Licensed Content Author	R. Betti et al
Licensed Content Date	May 3, 2016
Type of Use	Thesis/Dissertation
Requestor type	academic/university or research institute
Format	print and electronic
Portion	figures/tables/illustrations
Number of figures/tables /illustrations	1
High-res required	no
Will you be translating?	no
Circulation/distribution	1 - 29
Author of this Springer Nature content	no
Title	Particle-in-cell simulations of stimulated Raman scattering in the kinetic regime for direct-drive inertial confinement fusion
Institution name	University of Warwick
Expected presentation date	Sep 2021
Portions	Figure 1 and caption (to be adapted).
Requestor Location	SJ Spencer 480 Banbury Road Oxford, OX2 8EN United Kingdom Attn: SJ Spencer
Total	0.00 GBP

Terms and Conditions

Springer Nature Customer Service Centre GmbH
Terms and Conditions

This agreement sets out the terms and conditions of the licence (the **Licence**) between you and **Springer Nature Customer Service Centre GmbH** (the **Licensor**). By clicking 'accept' and completing the transaction for the material (**Licensed Material**), you also confirm your acceptance of these terms and conditions.

1. Grant of License

1. 1. The Licensor grants you a personal, non-exclusive, non-transferable, world-wide licence to reproduce the Licensed Material for the purpose specified in your order only. Licences are granted for the specific use requested in the order and for no other use, subject to the conditions below.

1. 2. The Licensor warrants that it has, to the best of its knowledge, the rights to license reuse of the Licensed Material. However, you should ensure that the material you are requesting is original to the Licensor and does not carry the copyright of another entity (as credited in the published version).

1. 3. If the credit line on any part of the material you have requested indicates that it was reprinted or adapted with permission from another source, then you should also seek permission from that source to reuse the material.

2. Scope of Licence

2. 1. You may only use the Licensed Content in the manner and to the extent permitted by these Ts&Cs and any applicable laws.

2. 2. A separate licence may be required for any additional use of the Licensed Material, e.g. where a licence has been purchased for print only use, separate permission must be obtained for electronic re-use. Similarly, a licence is only valid in the language selected and does not apply for editions in other languages unless additional translation rights have been granted separately in the licence. Any content owned by third parties are expressly excluded from the licence.

2. 3. Similarly, rights for additional components such as custom editions and derivatives require additional permission and may be subject to an additional fee. Please apply to Journalpermissions@springernature.com/bookpermissions@springernature.com for these rights.

2. 4. Where permission has been granted **free of charge** for material in print, permission may also be granted for any electronic version of that work, provided that the material is incidental to your work as a whole and that the electronic version is essentially equivalent to, or substitutes for, the print version.

2. 5. An alternative scope of licence may apply to signatories of the STM Permissions Guidelines, as amended from time to time.

3. Duration of Licence

3. 1. A licence for is valid from the date of purchase ('Licence Date') at the end of the relevant period in the below table:

Scope of Licence	**Duration of Licence**
Post on a website	12 months
Presentations	12 months
Books and journals	Lifetime of the edition in the language purchased

4. Acknowledgement

4. 1. The Licensor's permission must be acknowledged next to the Licenced Material in print. In electronic form, this acknowledgement must be visible at the same time as the figures/tables/illustrations or abstract, and must be hyperlinked to the journal/book's homepage. Our required acknowledgement format is in the Appendix below.

5. Restrictions on use

5. 1. Use of the Licensed Material may be permitted for incidental promotional use and minor editing privileges e.g. minor adaptations of single figures, changes of format, colour and/or style where the adaptation is credited as set out in Appendix 1 below. Any other changes including but not limited to, cropping, adapting, omitting material that affect the meaning, intention or moral rights of the author are strictly prohibited.

5. 2. You must not use any Licensed Material as part of any design or trademark.

5. 3. Licensed Material may be used in Open Access Publications (OAP) before publication by Springer Nature, but any Licensed Material must be removed from OAP sites prior to final publication.

6. Ownership of Rights

6. 1. Licensed Material remains the property of either Licensor or the relevant third party and any rights not explicitly granted herein are expressly reserved.

7. Warranty

IN NO EVENT SHALL LICENSOR BE LIABLE TO YOU OR ANY OTHER PARTY OR ANY OTHER PERSON OR FOR ANY SPECIAL, CONSEQUENTIAL, INCIDENTAL OR INDIRECT DAMAGES, HOWEVER CAUSED, ARISING OUT OF OR IN CONNECTION WITH THE DOWNLOADING, VIEWING OR USE OF THE MATERIALS REGARDLESS OF THE FORM OF ACTION, WHETHER FOR BREACH OF CONTRACT, BREACH OF WARRANTY, TORT, NEGLIGENCE, INFRINGEMENT OR OTHERWISE (INCLUDING, WITHOUT LIMITATION, DAMAGES BASED ON LOSS OF PROFITS, DATA, FILES, USE, BUSINESS OPPORTUNITY OR CLAIMS OF THIRD PARTIES), AND
WHETHER OR NOT THE PARTY HAS BEEN ADVISED OF THE POSSIBILITY OF SUCH DAMAGES. THIS LIMITATION SHALL APPLY NOTWITHSTANDING ANY FAILURE OF ESSENTIAL PURPOSE OF ANY LIMITED REMEDY PROVIDED HEREIN.

8. Limitations

8. 1. ***BOOKS ONLY:*** Where **'reuse in a dissertation/thesis'** has been selected the following terms apply: Print rights of the final author's accepted manuscript (for clarity, NOT the published version) for up to 100 copies, electronic rights for use only on a personal website or institutional repository as defined by the Sherpa guideline (www.sherpa.ac.uk/romeo/).

8. 2. For content reuse requests that qualify for permission under the STM Permissions Guidelines, which may be updated from time to time, the STM Permissions Guidelines supersede the terms and conditions contained in this licence.

9. Termination and Cancellation

9. 1. Licences will expire after the period shown in Clause 3 (above).

9. 2. Licensee reserves the right to terminate the Licence in the event that payment is not received in full or if there has been a breach of this agreement by you.

Appendix 1 — Acknowledgements:

For Journal Content:
Reprinted by permission from [**the Licensor**]: [**Journal Publisher** (e.g. Nature/Springer/Palgrave)] [**JOURNAL NAME**] [**REFERENCE CITATION** (Article name, Author(s) Name), [**COPYRIGHT**] (year of publication)

For **Advance Online Publication papers:**
Reprinted by permission from [**the Licensor**]: [**Journal Publisher** (e.g. Nature/Springer/Palgrave)] [**JOURNAL NAME**] [**REFERENCE CITATION** (Article name, Author(s) Name), [**COPYRIGHT**] (year of publication), advance online publication, day month year (doi: 10.1038/sj.[JOURNAL ACRONYM].)

For Adaptations/Translations:
Adapted/Translated by permission from [**the Licensor**]: [**Journal Publisher** (e.g. Nature/Springer/Palgrave)] [**JOURNAL NAME**] [**REFERENCE CITATION** (Article name, Author(s) Name), [**COPYRIGHT**] (year of publication)

Note: For any republication from the British Journal of Cancer, the following credit line style applies:

Reprinted/adapted/translated by permission from [**the Licensor**]: on behalf of Cancer Research UK: : [**Journal Publisher** (e.g. Nature/Springer/Palgrave)] [**JOURNAL NAME**] [**REFERENCE CITATION** (Article name, Author(s) Name), [**COPYRIGHT**] (year of publication)

For **Advance Online Publication** papers:
Reprinted by permission from The [**the Licensor**]: on behalf of Cancer Research UK: [**Journal Publisher** (e.g. Nature/Springer/Palgrave)] [**JOURNAL NAME**] [**REFERENCE CITATION** (Article name, Author(s) Name), [**COPYRIGHT**] (year of publication), advance online publication, day month year (doi: 10.1038/sj.[JOURNAL ACRONYM])

For Book content:
Reprinted/adapted by permission from [**the Licensor**]: [**Book Publisher** (e.g. Palgrave Macmillan, Springer etc) [**Book Title**] by [**Book author**(s)] [**COPYRIGHT**] (year of publication)

Other Conditions:

Version 1.3

Questions? customercare@copyright.com or +1-855-239-3415 (toll free in the US) or +1-978-646-2777.

American Physical Society
Reuse and Permissions License

04-Feb-2021

This license agreement between the American Physical Society ("APS") and SJ Spencer ("You") consists of your license details and the terms and conditions provided by the American Physical Society and SciPris.

Licensed Content Information

License Number:	**RNP/21/FEB/036065**
License date:	04-Feb-2021
DOI:	10.1103/PhysRevLett.103.045004
Title:	Shock Ignition: A New Approach to High Gain Inertial Confinement Fusion on the National Ignition Facility
Author:	L. J. Perkins et al.
Publication:	Physical Review Letters
Publisher:	American Physical Society
Cost:	USD $ 0.00

Request Details

Does your reuse require significant modifications: No

Specify intended distribution locations:	Worldwide
Reuse Category:	Reuse in a thesis/dissertation
Requestor Type:	Student
Items for Reuse:	Figures/Tables
Number of Figure/Tables:	1
Figure/Tables Details:	Figure 1 parts a and b, caption text to be adapted.
Format for Reuse:	Print and Electronic
Total number of print copies:	Up to 1000

Information about New Publication:

University/Publisher:	University of Warwick, Coventry
Title of dissertation/thesis:	Particle-in-cell simulations of stimulated Raman scattering in the kinetic regime for direct-drive inertial confinement fusion
Author(s):	SJ Spencer
Expected completion date:	Sep. 2021

License Requestor Information

Name:	SJ Spencer
Affiliation:	Individual
Email Id:	sj_spencer@outlook.com
Country:	United Kingdom

American Physical Society
Reuse and Permissions License

TERMS AND CONDITIONS

The American Physical Society (APS) is pleased to grant the Requestor of this license a non-exclusive, non-transferable permission, limited to Print and Electronic format, provided all criteria outlined below are followed.

1. You must also obtain permission from at least one of the lead authors for each separate work, if you haven't done so already. The author's name and affiliation can be found on the first page of the published Article.
2. For electronic format permissions, Requestor agrees to provide a hyperlink from the reprinted APS material using the source material's DOI on the web page where the work appears. The hyperlink should use the standard DOI resolution URL, http://dx.doi.org/{DOI}. The hyperlink may be embedded in the copyright credit line.
3. For print format permissions, Requestor agrees to print the required copyright credit line on the first page where the material appears: "Reprinted (abstract/excerpt/figure) with permission from [(FULL REFERENCE CITATION) as follows: Author's Names, APS Journal Title, Volume Number, Page Number and Year of Publication.] Copyright (YEAR) by the American Physical Society."
4. Permission granted in this license is for a one-time use and does not include permission for any future editions, updates, databases, formats or other matters. Permission must be sought for any additional use.
5. Use of the material does not and must not imply any endorsement by APS.
6. APS does not imply, purport or intend to grant permission to reuse materials to which it does not hold copyright. It is the requestor's sole responsibility to ensure the licensed material is original to APS and does not contain the copyright of another entity, and that the copyright notice of the figure, photograph, cover or table does not indicate it was reprinted by APS with permission from another source.
7. The permission granted herein is personal to the Requestor for the use specified and is not transferable or assignable without express written permission of APS. This license may not be amended except in writing by APS.
8. You may not alter, edit or modify the material in any manner.
9. You may translate the materials only when translation rights have been granted.
10. APS is not responsible for any errors or omissions due to translation.
11. You may not use the material for promotional, sales, advertising or marketing purposes.
12. The foregoing license shall not take effect unless and until APS or its agent, Aptara, receives payment in full in accordance with Aptara Billing and Payment Terms and Conditions, which are incorporated herein by reference.
13. Should the terms of this license be violated at any time, APS or Aptara may revoke the license with no refund to you and seek relief to the fullest extent of the laws of the USA. Official written notice will be made using the contact information provided with the permission request. Failure to receive such notice will not nullify revocation of the permission.
14. APS reserves all rights not specifically granted herein.
15. This document, including the Aptara Billing and Payment Terms and Conditions, shall be the entire agreement between the parties relating to the subject matter hereof.

AIP PUBLISHING LICENSE
TERMS AND CONDITIONS

Jul 22, 2021

This Agreement between SJ Spencer ("You") and AIP Publishing ("AIP Publishing") consists of your license details and the terms and conditions provided by AIP Publishing and Copyright Clearance Center.

License Number	5114160676677
License date	Jul 22, 2021
Licensed Content Publisher	AIP Publishing
Licensed Content Publication	Physics of Plasmas
Licensed Content Title	Two decades of progress in understanding and control of laser plasma instabilities in indirect drive inertial fusion
Licensed Content Author	David S. Montgomery
Licensed Content Date	May 1, 2016
Licensed Content Volume	23
Licensed Content Issue	5
Type of Use	Thesis/Dissertation
Requestor type	Author (original article)
Format	Print and electronic

Oxford, OX2 8EN
United Kingdom
Attn: SJ Spencer

Total 0.00 GBP

Terms and Conditions

AIP Publishing -- Terms and Conditions: Permissions Uses

AIP Publishing hereby grants to you the non-exclusive right and license to use and/or distribute the Material according to the use specified in your order, on a one-time basis, for the specified term, with a maximum distribution equal to the number that you have ordered. Any links or other content accompanying the Material are not the subject of this license.

1. You agree to include the following copyright and permission notice with the reproduction of the Material:"Reprinted from [FULL CITATION], with the permission of AIP Publishing." For an article, the credit line and permission notice must be printed on the first page of the article or book chapter. For photographs, covers, or tables, the notice may appear with the Material, in a footnote, or in the reference list.
2. If you have licensed reuse of a figure, photograph, cover, or table, it is your responsibility to ensure that the material is original to AIP Publishing and does not contain the copyright of another entity, and that the copyright notice of the figure, photograph, cover, or table does not indicate that it was reprinted by AIP Publishing, with permission, from another source. Under no circumstances does AIP Publishing purport or intend to grant permission to reuse material to which it does not hold appropriate rights.
   You may not alter or modify the Material in any manner. You may translate the Material into another language only if you have licensed translation rights. You may not use the Material for promotional purposes.
3. The foregoing license shall not take effect unless and until AIP Publishing or its agent, Copyright Clearance Center, receives the Payment in accordance with Copyright Clearance Center Billing and Payment Terms and Conditions, which are incorporated herein by reference.
4. AIP Publishing or Copyright Clearance Center may, within two business days of granting this license, revoke the license for any reason whatsoever, with a full refund payable to you. Should you violate the terms of this license at any time, AIP Publishing, or Copyright Clearance Center may revoke the license with no refund to you. Notice of such revocation will be made using the contact information provided by you. Failure to receive such notice will not nullify the revocation.
5. AIP Publishing makes no representations or warranties with respect to the Material. You agree to indemnify and hold harmless AIP Publishing, and their officers, directors, employees or agents

AIP PUBLISHING LICENSE
TERMS AND CONDITIONS

Aug 26, 2021

This Agreement between SJ Spencer ("You") and AIP Publishing ("AIP Publishing") consists of your license details and the terms and conditions provided by AIP Publishing and Copyright Clearance Center.

License Number	5136510435582
License date	Aug 26, 2021
Licensed Content Publisher	AIP Publishing
Licensed Content Publication	Physics of Plasmas
Licensed Content Title	Two decades of progress in understanding and control of laser plasma instabilities in indirect drive inertial fusion
Licensed Content Author	David S. Montgomery
Licensed Content Date	May 1, 2016
Licensed Content Volume	23
Licensed Content Issue	5
Type of Use	Thesis/Dissertation
Requestor type	Student
Format	Print and electronic
Portion	Figure/Table
Number of figures/tables	1
Will you be translating?	No
Title	Particle-in-cell simulations of stimulated Raman scattering in the kinetic regime for direct-drive inertial confinement fusion
Institution name	University of Warwick
Expected presentation date	Sep 2021
Portions	Figure 4 parts b,c,d and caption to be adapted.

SJ Spencer
480 Banbury Road

Requestor Location

Oxford, OX2 8EN
United Kingdom
Attn: SJ Spencer

Total 0.00 GBP

Terms and Conditions

AIP Publishing -- Terms and Conditions: Permissions Uses

AIP Publishing hereby grants to you the non-exclusive right and license to use and/or distribute the Material according to the use specified in your order, on a one-time basis, for the specified term, with a maximum distribution equal to the number that you have ordered. Any links or other content accompanying the Material are not the subject of this license.

1. You agree to include the following copyright and permission notice with the reproduction of the Material:"Reprinted from [FULL CITATION], with the permission of AIP Publishing." For an article, the credit line and permission notice must be printed on the first page of the article or book chapter. For photographs, covers, or tables, the notice may appear with the Material, in a footnote, or in the reference list.
2. If you have licensed reuse of a figure, photograph, cover, or table, it is your responsibility to ensure that the material is original to AIP Publishing and does not contain the copyright of another entity, and that the copyright notice of the figure, photograph, cover, or table does not indicate that it was reprinted by AIP Publishing, with permission, from another source. Under no circumstances does AIP Publishing purport or intend to grant permission to reuse material to which it does not hold appropriate rights.
   You may not alter or modify the Material in any manner. You may translate the Material into another language only if you have licensed translation rights. You may not use the Material for promotional purposes.
3. The foregoing license shall not take effect unless and until AIP Publishing or its agent, Copyright Clearance Center, receives the Payment in accordance with Copyright Clearance Center Billing and Payment Terms and Conditions, which are incorporated herein by reference.
4. AIP Publishing or Copyright Clearance Center may, within two business days of granting this license, revoke the license for any reason whatsoever, with a full refund payable to you. Should you violate the terms of this license at any time, AIP Publishing, or Copyright Clearance Center may revoke the license with no refund to you. Notice of such revocation will be made using the contact information provided by you. Failure to receive such notice will not nullify the revocation.
5. AIP Publishing makes no representations or warranties with respect to the Material. You agree to indemnify and hold harmless AIP Publishing, and their officers, directors, employees or agents from and against any and all claims arising out of your use of the Material other than as specifically authorized herein.
6. The permission granted herein is personal to you and is not transferable or assignable without the prior written permission of AIP Publishing. This license may not be amended except in a writing signed by the party to be charged.
7. If purchase orders, acknowledgments or check endorsements are issued on any forms containing terms and conditions which are inconsistent with these provisions, such inconsistent terms and conditions shall be of no force and effect. This document, including the CCC Billing and Payment Terms and Conditions, shall be the entire agreement between the parties relating to the subject matter hereof.

This Agreement shall be governed by and construed in accordance with the laws of the State of New York. Both parties hereby submit to the jurisdiction of the courts of New York County for purposes of resolving any disputes that may arise hereunder.

V1.2

AIP PUBLISHING LICENSE
TERMS AND CONDITIONS

Jul 13, 2021

This Agreement between SJ Spencer ("You") and AIP Publishing ("AIP Publishing") consists of your license details and the terms and conditions provided by AIP Publishing and Copyright Clearance Center.

License Number	5107091150935
License date	Jul 13, 2021
Licensed Content Publisher	AIP Publishing
Licensed Content Publication	Physics of Plasmas
Licensed Content Title	Different kλD regimes for nonlinear effects on Langmuir waves
Licensed Content Author	J. L. Kline, D. S. Montgomery, L. Yin, et al
Licensed Content Date	May 1, 2006
Licensed Content Volume	13
Licensed Content Issue	5
Type of Use	Thesis/Dissertation
Requestor type	Student

Format	Print and electronic
Portion	Figure/Table
Number of figures/tables	1
Will you be translating?	No
Title	Particle-in-cell simulations of stimulated Raman scattering in the kinetic regime for direct-drive inertial confinement fusion
Institution name	University of Warwick
Expected presentation date	Sep 2021
Portions	Figure 1, caption to be adapted by author
Requestor Location	SJ Spencer 480 Banbury Road Oxford, OX2 8EN United Kingdom Attn: SJ Spencer
Total	0.00 GBP

Terms and Conditions

AIP Publishing -- Terms and Conditions: Permissions Uses

AIP Publishing hereby grants to you the non-exclusive right and license to use and/or distribute the Material according to the use specified in your order, on a one-time basis, for the specified term, with a maximum distribution equal to the number that you have ordered. Any links or other content accompanying the Material are not the subject of this license.

1. You agree to include the following copyright and permission notice with the reproduction of the Material:"Reprinted from [FULL CITATION], with the permission of AIP Publishing." For an article, the credit line and permission notice must be printed on the first page of the article or book chapter. For photographs, covers, or tables, the notice may appear with the Material, in a footnote, or in the reference list.
2. If you have licensed reuse of a figure, photograph, cover, or table, it is your responsibility to ensure that the material is original to AIP Publishing and does not contain the copyright of another entity, and that the copyright notice of the figure, photograph, cover, or table does not indicate that it was reprinted by AIP Publishing, with permission, from another source. Under no circumstances does AIP Publishing purport or intend to grant permission to reuse material to which it does not hold appropriate rights.
   You may not alter or modify the Material in any manner. You may translate the Material into another language only if you have licensed translation rights. You may not use the Material for promotional purposes.
3. The foregoing license shall not take effect unless and until AIP Publishing or its agent, Copyright Clearance Center, receives the Payment in accordance with Copyright Clearance Center Billing and Payment Terms and Conditions, which are incorporated herein by reference.
4. AIP Publishing or Copyright Clearance Center may, within two business days of granting this license, revoke the license for any reason whatsoever, with a full refund payable to you. Should you violate the terms of this license at any time, AIP Publishing, or Copyright Clearance Center may revoke the license with no refund to you. Notice of such revocation will be made using the contact information provided by you. Failure to receive such notice will not nullify the revocation.
5. AIP Publishing makes no representations or warranties with respect to the Material. You agree to indemnify and hold harmless AIP Publishing, and their officers, directors, employees or agents from and against any and all claims arising out of your use of the Material other than as specifically authorized herein.
6. The permission granted herein is personal to you and is not transferable or assignable without the prior written permission of AIP Publishing. This license may not be amended except in a writing signed by the party to be charged.
7. If purchase orders, acknowledgments or check endorsements are issued on any forms containing terms and conditions which are inconsistent with these provisions, such inconsistent terms and conditions shall be of no force and effect. This document, including the CCC Billing and Payment Terms and Conditions, shall be the entire agreement between the parties relating to the subject matter hereof.

This Agreement shall be governed by and construed in accordance with the laws of the State of New York. Both parties hereby submit to the jurisdiction of the courts of New York County for purposes of resolving

any disputes that may arise hereunder.

V1.2

Questions? customercare@copyright.com or +1-855-239-3415 (toll free in the US) or +1-978-646-2777.

SPRINGER NATURE LICENSE
TERMS AND CONDITIONS

Sep 19, 2021

This Agreement between SJ Spencer ("You") and Springer Nature ("Springer Nature") consists of your license details and the terms and conditions provided by Springer Nature and Copyright Clearance Center.

License Number	5152651294315
License date	Sep 19, 2021
Licensed Content Publisher	Springer Nature
Licensed Content Publication	Springer eBook
Licensed Content Title	The Particle-in-Cell Method
Licensed Content Author	David Tskhakaya
Licensed Content Date	Jan 1, 2008
Type of Use	Thesis/Dissertation
Requestor type	academic/university or research institute
Format	print and electronic
Portion	figures/tables/illustrations
Number of figures/tables/illustrations	1
Will you be translating?	no
Circulation/distribution	30 - 99
Author of this Springer Nature content	no
Title	Particle-in-cell simulations of stimulated Raman scattering in the kinetic regime for direct-drive inertial confinement fusion
Institution name	University of Warwick
Expected presentation	Sep 2021

date

Portions	Figure 6.1
Requestor Location	SJ Spencer 480 Banbury Road Oxford, OX2 8EN United Kingdom Attn: SJ Spencer
Total	0.00 GBP

Terms and Conditions

Springer Nature Customer Service Centre GmbH
Terms and Conditions

This agreement sets out the terms and conditions of the licence (the **Licence**) between you and **Springer Nature Customer Service Centre GmbH** (the **Licensor**). By clicking 'accept' and completing the transaction for the material (**Licensed Material**), you also confirm your acceptance of these terms and conditions.

1. Grant of License

1. 1. The Licensor grants you a personal, non-exclusive, non-transferable, world-wide licence to reproduce the Licensed Material for the purpose specified in your order only. Licences are granted for the specific use requested in the order and for no other use, subject to the conditions below.

1. 2. The Licensor warrants that it has, to the best of its knowledge, the rights to license reuse of the Licensed Material. However, you should ensure that the material you are requesting is original to the Licensor and does not carry the copyright of another entity (as credited in the published version).

1. 3. If the credit line on any part of the material you have requested indicates that it was reprinted or adapted with permission from another source, then you should also seek permission from that source to reuse the material.

2. Scope of Licence

2. 1. You may only use the Licensed Content in the manner and to the extent permitted by these Ts&Cs and any applicable laws.

2. 2. A separate licence may be required for any additional use of the Licensed Material, e.g. where a licence has been purchased for print only use, separate permission must be obtained for electronic re-use. Similarly, a licence is only valid in the language selected and does not apply for editions in other languages unless additional translation rights have been granted separately in the licence. Any content owned by third parties are expressly excluded from the licence.

2. 3. Similarly, rights for additional components such as custom editions and derivatives require additional permission and may be subject to an additional fee. Please apply to Journalpermissions@springernature.com/bookpermissions@springernature.com for these rights.

2. 4. Where permission has been granted **free of charge** for material in print, permission may also be granted for any electronic version of that work, provided that the material is incidental to your work as a whole and that the electronic version is essentially equivalent to, or substitutes for, the print version.

2. 5. An alternative scope of licence may apply to signatories of the STM Permissions Guidelines, as amended from time to time.

3. Duration of Licence

3. 1. A licence for is valid from the date of purchase ('Licence Date') at the end of the relevant period in the below table:

Scope of Licence	Duration of Licence
Post on a website	12 months
Presentations	12 months
Books and journals	Lifetime of the edition in the language purchased

4. Acknowledgement

4. 1. The Licensor's permission must be acknowledged next to the Licenced Material in print. In electronic form, this acknowledgement must be visible at the same time as the figures/tables/illustrations or abstract, and must be hyperlinked to the journal/book's homepage. Our required acknowledgement format is in the Appendix below.

5. Restrictions on use

5. 1. Use of the Licensed Material may be permitted for incidental promotional use and minor editing privileges e.g. minor adaptations of single figures, changes of format, colour and/or style where the adaptation is credited as set out in Appendix 1 below. Any other changes including but not limited to, cropping, adapting, omitting material that affect the meaning, intention or moral rights of the author are strictly prohibited.

5. 2. You must not use any Licensed Material as part of any design or trademark.

5. 3. Licensed Material may be used in Open Access Publications (OAP) before publication by Springer Nature, but any Licensed Material must be removed from OAP sites prior to final publication.

6. Ownership of Rights

6. 1. Licensed Material remains the property of either Licensor or the relevant third party and any rights not explicitly granted herein are expressly reserved.

7. Warranty

IN NO EVENT SHALL LICENSOR BE LIABLE TO YOU OR ANY OTHER PARTY OR ANY OTHER PERSON OR FOR ANY SPECIAL, CONSEQUENTIAL, INCIDENTAL OR INDIRECT DAMAGES, HOWEVER CAUSED, ARISING OUT OF OR IN CONNECTION WITH THE DOWNLOADING, VIEWING OR USE OF THE MATERIALS REGARDLESS OF THE FORM OF ACTION, WHETHER FOR BREACH OF CONTRACT, BREACH OF WARRANTY, TORT, NEGLIGENCE, INFRINGEMENT OR OTHERWISE (INCLUDING, WITHOUT LIMITATION, DAMAGES BASED ON LOSS OF PROFITS, DATA, FILES, USE, BUSINESS OPPORTUNITY OR CLAIMS OF THIRD PARTIES), AND
WHETHER OR NOT THE PARTY HAS BEEN ADVISED OF THE POSSIBILITY OF SUCH DAMAGES. THIS LIMITATION SHALL APPLY NOTWITHSTANDING ANY FAILURE OF ESSENTIAL PURPOSE OF ANY LIMITED REMEDY PROVIDED HEREIN.

8. Limitations

8. 1. ***BOOKS ONLY:***Where **'reuse in a dissertation/thesis'** has been selected the following terms apply: Print rights of the final author's accepted manuscript (for clarity, NOT the published version) for up to 100 copies, electronic rights for use only on a personal website or institutional repository as defined by the Sherpa guideline (www.sherpa.ac.uk/romeo/).

8. 2. For content reuse requests that qualify for permission under the STM Permissions Guidelines, which may be updated from time to time, the STM Permissions Guidelines

supersede the terms and conditions contained in this licence.

9. Termination and Cancellation

9. 1. Licences will expire after the period shown in Clause 3 (above).

9. 2. Licensee reserves the right to terminate the Licence in the event that payment is not received in full or if there has been a breach of this agreement by you.

Appendix 1 — Acknowledgements:

For Journal Content:
Reprinted by permission from [**the Licensor**]: [**Journal Publisher** (e.g. Nature/Springer/Palgrave)] [**JOURNAL NAME**] [**REFERENCE CITATION** (Article name, Author(s) Name), [**COPYRIGHT**] (year of publication)

For **Advance Online Publication papers:**
Reprinted by permission from [**the Licensor**]: [**Journal Publisher** (e.g. Nature/Springer/Palgrave)] [**JOURNAL NAME**] [**REFERENCE CITATION** (Article name, Author(s) Name), [**COPYRIGHT**] (year of publication), advance online publication, day month year (doi: 10.1038/sj.[JOURNAL ACRONYM].)

For Adaptations/Translations:
Adapted/Translated by permission from [**the Licensor**]: [**Journal Publisher** (e.g. Nature/Springer/Palgrave)] [**JOURNAL NAME**] [**REFERENCE CITATION** (Article name, Author(s) Name), [**COPYRIGHT**] (year of publication)

Note: For any republication from the British Journal of Cancer, the following credit line style applies:

Reprinted/adapted/translated by permission from [**the Licensor**]: on behalf of Cancer Research UK: : [**Journal Publisher** (e.g. Nature/Springer/Palgrave)] [**JOURNAL NAME**] [**REFERENCE CITATION** (Article name, Author(s) Name), [**COPYRIGHT]** (year of publication)

For **Advance Online Publication** papers:
Reprinted by permission from The [**the Licensor**]: on behalf of Cancer Research UK: [**Journal Publisher** (e.g. Nature/Springer/Palgrave)] [**JOURNAL NAME**] [**REFERENCE CITATION** (Article name, Author(s) Name), [**COPYRIGHT**] (year of publication), advance online publication, day month year (doi: 10.1038/sj.[JOURNAL ACRONYM])

For Book content:
Reprinted/adapted by permission from [**the Licensor**]: [**Book Publisher** (e.g. Palgrave Macmillan, Springer etc) [**Book Title**] by [**Book author**(s)] [**COPYRIGHT**] (year of publication)

Other Conditions:

Version 1.3

Questions? customercare@copyright.com or +1-855-239-3415 (toll free in the US) or +1-978-646-2777.

AIP PUBLISHING LICENSE
TERMS AND CONDITIONS

Jan 06, 2021

This Agreement between SJ Spencer ("You") and AIP Publishing ("AIP Publishing") consists of your license details and the terms and conditions provided by AIP Publishing and Copyright Clearance Center.

License Number	4982981039259
License date	Jan 06, 2021
Licensed Content Publisher	AIP Publishing
Licensed Content Publication	Physics of Plasmas
Licensed Content Title	Inflationary stimulated Raman scattering in shock-ignition plasmas
Licensed Content Author	S. J. Spencer, A. G. Seaton, T. Goffrey, et al
Licensed Content Date	Dec 1, 2020
Licensed Content Volume	27
Licensed Content Issue	12
Type of Use	Thesis/Dissertation
Requestor type	Author (original article)
Format	Print and electronic
Portion	Excerpt (> 800 words)
Will you be translating?	No
Title	Particle-in-cell simulations of stimulated Raman scattering in the kinetic regime for direct-drive inertial confinement fusion
Institution name	University of Warwick
Expected presentation date	Sep 2021
Portions	All figures and their captions; paragraphs 5-9; Table 1; all of section 2; derivation presented in section 3; all of Section 4
Requestor Location	SJ Spencer 480 Banbury Road Oxford, OX2 8EN United Kingdom Attn: SJ Spencer

Total 0.00 GBP

Terms and Conditions

AIP Publishing -- Terms and Conditions: Permissions Uses

AIP Publishing hereby grants to you the non-exclusive right and license to use and/or distribute the Material according to the use specified in your order, on a one-time basis, for the specified term, with a maximum distribution equal to the number that you have ordered. Any links or other content accompanying the Material are not the subject of this license.

1. You agree to include the following copyright and permission notice with the reproduction of the Material:"Reprinted from [FULL CITATION], with the permission of AIP Publishing." For an article, the credit line and permission notice must be printed on the first page of the article or book chapter. For photographs, covers, or tables, the notice may appear with the Material, in a footnote, or in the reference list.
2. If you have licensed reuse of a figure, photograph, cover, or table, it is your responsibility to ensure that the material is original to AIP Publishing and does not contain the copyright of another entity, and that the copyright notice of the figure, photograph, cover, or table does not indicate that it was reprinted by AIP Publishing, with permission, from another source. Under no circumstances does AIP Publishing purport or intend to grant permission to reuse material to which it does not hold appropriate rights.
   You may not alter or modify the Material in any manner. You may translate the Material into another language only if you have licensed translation rights. You may not use the Material for promotional purposes.
3. The foregoing license shall not take effect unless and until AIP Publishing or its agent, Copyright Clearance Center, receives the Payment in accordance with Copyright Clearance Center Billing and Payment Terms and Conditions, which are incorporated herein by reference.
4. AIP Publishing or Copyright Clearance Center may, within two business days of granting this license, revoke the license for any reason whatsoever, with a full refund payable to you. Should you violate the terms of this license at any time, AIP Publishing, or Copyright Clearance Center may revoke the license with no refund to you. Notice of such revocation will be made using the contact information provided by you. Failure to receive such notice will not nullify the revocation.
5. AIP Publishing makes no representations or warranties with respect to the Material. You agree to indemnify and hold harmless AIP Publishing, and their officers, directors, employees or agents from and against any and all claims arising out of your use of the Material other than as specifically authorized herein.
6. The permission granted herein is personal to you and is not transferable or assignable without the prior written permission of AIP Publishing. This license may not be amended except in a writing signed by the party to be charged.
7. If purchase orders, acknowledgments or check endorsements are issued on any forms containing terms and conditions which are inconsistent with these provisions, such inconsistent terms and conditions shall be of no force and effect. This document, including the CCC Billing and Payment Terms and Conditions, shall be the entire agreement between the parties relating to the subject matter hereof.

This Agreement shall be governed by and construed in accordance with the laws of the State of New York. Both parties hereby submit to the jurisdiction of the courts of New York County for purposes of resolving any disputes that may arise hereunder.

V1.2

Questions? customercare@copyright.com or +1-855-239-3415 (toll free in the US) or +1-978-646-2777.

Bibliography

T. D. Arber, K. Bennet, C. S. Brady, A. Lawrence-Douglas, M. G. Ramsay, N. J. Sircombe, P. Gillies, R. G. Evans, H. Schmitz, A. R. Bell, and C. P. Ridgers. Contemporary particle-in-cell approach to laser-plasma modeling. *Plasma Physics and Controlled Fusion*, 57:113001, 2015. doi: 10.1088/0741-3335/57/11/113001. URL https://doi.org/10.1088/0741-3335/57/11/113001.

J.W. Bates, R.K. Follett, J.G. Shaw, S.P. Obenschain, R.H. Lehmberg, J.F. Myatt, J.L. Weaver, D.M. Kehne, M.F. Wolford, M.C. Myers, and T.J. Kessler. Suppressing cross-beam energy transfer with broadband lasers. *High Energy Density Physics*, 36:100772, 2020. ISSN 1574-1818. doi: https://doi.org/10.1016/j.hedp.2020.100772. URL https://www.sciencedirect.com/science/article/pii/S1574181820300501.

S. D. Baton, A. Colaïtis, C. Rousseaux, G. Boutoux, S. Brygoo, L. Jacquet, M. Koenig, D. Batani, A. Casner, E. Le Bel, D. Raffestin, A. Tentori, V. Tikhonchuk, J. Trela, C. Reverdin, L. Lederoff, W. Theobald, G. Cristoforetti, L. A. Gizzi, P. Koester, L. Labate, and K. Shigemori. Preliminary results from the LMJ-PETAL experiment on hot electrons characterization in the context of shock ignition. *High Energy Density Physics*, 36(March):100796, 2020. ISSN 15741818. doi: 10.1016/j.hedp.2020.100796. URL https://doi.org/10.1016/j.hedp.2020.100796.

M. S. Bawa'aneh. Stimulated brillouin scattering of x-waves in magnetized plasma. *Journal of Plasma Physics*, 72(5):687–697, 2006. doi: 10.1017/S0022377805004307. URL https://doi.org/10.1017/S0022377805004307.

R. Betti and O. A. Hurricane. Inertial-confinement fusion with lasers. *Nature Physics*, 12(5): 435–448, May 2016. doi: 10.1038/nphys3736. URL https://doi.org/10.1038/nphys3736.

R. Betti, C. D. Zhou, K. S. Anderson, L. J. Perkins, W. Theobald, and A. A. Solodov. Shock ignition of thermonuclear fuel with high areal density. *Phys. Rev. Lett.*, 98:155001, Apr 2007. doi: 10.1103/PhysRevLett.98.155001. URL https://link.aps.org/doi/10.1103/PhysRevLett.98.155001.

C.K. Birdsall and A.B. Langdon. *Plasma Physics via Computer Simulation*. Series in Plasma Physics and Fluid Dynamics. Taylor & Francis, 1st edition, 1991. ISBN 0-07-005371-5. URL https://doi.org/10.1201/9781315275048.

J.P. Boris and R.A. Shanny. *Relativistic plasma simulation-optimization of a hybrid code*. Naval Research Laboratory, 1973. URL https://books.google.co.uk/books?id=uYIuAAAAIAAJ.

N. Carpintero-Santamaría and G. Velarde. The pioneers' legacy of inertial confinement nuclear fusion. *Progress in Nuclear Energy*, 78:349 – 354, 2015. ISSN 0149-1970. doi: 10.1016/j.pnucene.2013.10.019. URL https://doi.org/10.1016/j.pnucene.2013.10.019.

P. Y. Chang, G. Fiksel, M. Hohenberger, J. P. Knauer, R. Betti, F. J. Marshall, D. D. Meyerhofer, F. H. Séguin, and R. D. Petrasso. Fusion yield enhancement in magnetized laser-driven implosions. *Phys. Rev. Lett.*, 107:035006, Jul 2011. doi: 10.1103/PhysRevLett.107.035006. URL https://0-link-aps-org.pugwash.lib.warwick.ac.uk/doi/10.1103/PhysRevLett.107.035006.

T. Chapman, S. Hüller, P. E. Masson-Laborde, W. Rozmus, and D. Pesme. Spatially autoresonant stimulated Raman scattering in inhomogeneous plasmas in the kinetic regime. *Physics of Plasmas*, 17(12), 2010. ISSN 1070664X. doi: 10.1063/1.3529362. URL https://doi.org/10.1063/1.3529362.

T. Chapman, S. Hüller, P. E. Masson-Laborde, A. Heron, D. Pesme, and W. Rozmus. Driven spatially autoresonant stimulated raman scattering in the kinetic regime. *Phys. Rev. Lett.*, 108:145003, Apr 2012. URL https://doi.org/10.1103/PhysRevLett.108.145003.

G. Cristoforetti, A. Colaïtis, L. Antonelli, S. Atzeni, F. Baffigi, D. Batani, F. Barbato, G. Boutoux, R. Dudzak, P. Koester, E. Krousky, L. Labate, Ph Nicolaï, O. Renner, M. Skoric, V. Tikhonchuk, and L. A. Gizzi. Experimental observation of parametric instabilities at laser intensities relevant for shock ignition. *EPL*, 117(3), 2017. ISSN 12864854. URL https://doi.org/10.1209/0295-5075/117/35001.

G. Cristoforetti, S. Huller, P. Koester, L. Antonelli, S. Atzeni, F. Baffigi, D. Batani, C. Baird, N. Booth, M. Galimberti, K. Glize, A. Heron, M. Khan, P. Loiseau, D. Mancelli, M. Notley, P. Oliveira, O. Renner, M. Smid, A. Schiavi, G. Tran, N. C. Woolsey, and L. A. Gizzi. Observation and modelling of Stimulated Raman Scattering driven by an optically smoothed laser beam in experimental conditions relevant for Shock Ignition. *arXiv:2108.13485 [physics]*, August 2021. URL http://arxiv.org/abs/2108.13485. arXiv: 2108.13485.

J. M. Dawson, V. K. Decyk, Robert W. Huff, I. Jechart, T. Katsouleas, J. N. Leboeuf, B. Lembege, R. M. Martinez, Y. Ohsawa, and S. T. Ratliff. Damping of large-amplitude plasma waves propagating perpendicular to the magnetic field. *Phys. Rev. Lett.*, 50:1455–1458, May 1983. doi: 10.1103/PhysRevLett.50.1455. URL https://link.aps.org/doi/10.1103/PhysRevLett.50.1455.

P. Dellar and A. Schekochihin. Lectures on kinetic theory and magnetohydrodynamics of plasmas. URL http://www-thphys.physics.ox.ac.uk/people/AlexanderSchekochihin/KT/.

J. Derouillat, A. Beck, F. Pérez, T. Vinci, M. Chiaramello, A. Grassi, M. Flé, G. Bouchard, I. Plotnikov, N. Aunai, J. Dargent, C. Riconda, and M. Grech. Smilei : A collaborative, open-source, multi-purpose particle-in-cell code for plasma simulation. *Computer Physics Communications*, 222:351–373, 2018. ISSN 0010-4655. doi: https://doi.org/10.1016/j.cpc.2017.09.024. URL https://www.sciencedirect.com/science/article/pii/S0010465517303314.

M. E. Dieckmann, S. J. Spencer, M. Falk, and G. Rowlands. Preferential acceleration of positrons by a filamentation instability between an electron–proton beam and a pair plasma beam. *Physics of Plasmas*, 27(12):122102, 2020. doi: 10.1063/5.0021257. URL https://doi.org/10.1063/5.0021257.

I. N. Ellis, D. J. Strozzi, B. J. Winjum, F. S. Tsung, T. Grismayer, W. B. Mori, J. E. Fahlen, and E. A. Williams. Convective raman amplification of light pulses causing kinetic inflation in inertial fusion plasmas. *Physics of Plasmas*, 19(11):112704, November 2012. URL https://doi.org/10.1063/1.4762853.

T.Zh. Esirkepov. Exact charge conservation scheme for particle-in-cell simulation with an arbitrary form-factor. *Computer Physics Communications*, 135(2):144–153, 2001. ISSN 0010-4655. doi: https://doi.org/10.1016/S0010-4655(00)00228-9. URL https://www.sciencedirect.com/science/article/pii/S0010465500002289.

Juan C. Fernández, J. A. Cobble, D. S. Montgomery, M. D. Wilke, and B. B. Afeyan. Observed insensitivity of stimulated Raman scattering on electron density. *Physics of Plasmas*, 7(9): 3743–3750, 2000. ISSN 1070664X. doi: 10.1063/1.1287134. URL https://doi.org/10.1063/1.1287134.

R. K. Follett, J. G. Shaw, J. F. Myatt, C. Dorrer, D. H. Froula, and J. P. Palastro. Thresholds of absolute instabilities driven by a broadband laser. *Physics of Plasmas*, 26(6):062111, 2019. doi: 10.1063/1.5098479. URL https://doi.org/10.1063/1.5098479.

R. K. Follett, J. G. Shaw, J. F. Myatt, H. Wen, D. H. Froula, and J. P. Palastro. Thresholds of absolute two-plasmon-decay and stimulated raman scattering instabilities driven by multiple broadband lasers. *Physics of Plasmas*, 28(3):032103, 2021. doi: 10.1063/5.0037869. URL https://doi.org/10.1063/5.0037869.

R. A. Fonseca, L. O. Silva, F. S. Tsung, V. K. Decyk, W. Lu, C. Ren, W. B. Mori, S. Deng, S. Lee, T. Katsouleas, and J. C. Adam. Osiris: A three-dimensional, fully relativistic particle in cell code for modeling plasma based accelerators. In Peter M. A. Sloot, Alfons G. Hoekstra, C. J. Kenneth Tan, and Jack J. Dongarra, editors, *Computational Science — ICCS 2002*, pages 342–351, Berlin, Heidelberg, 2002. Springer Berlin Heidelberg. ISBN 978-3-540-47789-1.

D. W. Forslund, J. M. Kindel, and E. L. Lindman. Nonlinear behavior of stimulated brillouin and raman scattering in laser-irradiated plasmas. *Phys. Rev. Lett.*, 30:739–743, Apr 1973. doi: 10.1103/PhysRevLett.30.739. URL https://0-link-aps-org.pugwash.lib.warwick.ac.uk/doi/10.1103/PhysRevLett.30.739.

D W Forslund, J M Kindel, and E L Lindman. Theory of stimulated scattering processes in laser-irradiated plasmas. *Physics of Fluids*, 18(8):1002–1016, 1975. doi: 10.1063/1.861248.

Matthias Geissel, T. J. Awe, D. E. Bliss, M. E. Campbell, M. R. Gomez, E. Harding, A. J. Harvey-Thompson, S. B. Hansen, C. Jennings, M. W. Kimmel, P. Knapp, S. M. Lewis, R. D. McBride, K. Peterson, M. Schollmeier, D. J. Scoglietti, A. B. Sefkow, J. E. Shores, D. B. Sinars, S. A. Slutz, I. C. Smith, C. S. Speas, R. A. Vesey, and J. L. Porter. Nonlinear laser-plasma interaction in magnetized liner inertial fusion. In Konstantin L. Vodopyanov and Kenneth L. Schepler, editors, *Nonlinear Frequency Generation and Conversion: Materials, Devices, and Applications XV*, volume 9731, pages 100 – 106. International Society for Optics and Photonics, SPIE, 2016. URL https://doi.org/10.1117/12.2218577.

O. V. Gotchev, J. P. Knauer, P. Y. Chang, N. W. Jang, M. J. Shoup, D. D. Meyerhofer, and R. Betti. Seeding magnetic fields for laser-driven flux compression in high-energy-density plasmas. *Review of Scientific Instruments*, 80(4):043504, 2009. doi: 10.1063/1.3115983. URL https://doi.org/10.1063/1.3115983.

P. N. Guzdar, C. S. Liu, and R. H. Lehmberg. The effect of bandwidth on the convective Raman instability in inhomogeneous plasmas. *Physics of Fluids B: Plasma Physics*, 3(10):2882–2888, October 1991. ISSN 0899-8221. doi: 10.1063/1.859921. URL http://aip.scitation.org/doi/10.1063/1.859921.

A. Higginson, S. Zhang, M. Bailly-Grandvaux, C. McGuffey, K. Bhutwala, B. J. Winjum, J. Strehlow, B. Edghill, M. Dozieres, F. S. Tsung, R. Lee, S. Andrews, S. J. Spencer, N. Lemos, F. Albert, P. King, M. S. Wei, W. B. Mori, M. J.-E Manuel, and F. N. Beg. Electron acceleration at oblique angles via stimulated raman scattering at laser irradiance $> 10^{16}\mathrm{Wcm}^{-2}\mu\mathrm{m}^2$. *Phys. Rev. E*, 103:033203, Mar 2021. doi: 10.1103/PhysRevE.103.033203. URL https://link.aps.org/doi/10.1103/PhysRevE.103.033203.

M. Hohenberger, A. Shvydky, J. A. Marozas, G. Fiksel, M. J. Bonino, D. Canning, T. J. B. Collins, C. Dorrer, T. J. Kessler, B. E. Kruschwitz, P. W. McKenty, D. D. Meyerhofer, S. P. Regan, T. C. Sangster, and J. D. Zuegel. Optical smoothing of laser imprinting in planar-target experiments on omega ep using multi-fm 1-d smoothing by spectral dispersion. *Physics of Plasmas*, 23(9): 092702, 2016. doi: 10.1063/1.4962185. URL https://doi.org/10.1063/1.4962185.

Yu Ji, Chang-Wang Lian, Rui Yan, Chuang Ren, Dong Yang, Zhen-Hua Wan, Bin Zhao, Chen Wang, Zhi-Heng Fang, and Jian Zheng. Convective amplification of stimulated raman rescattering in a picosecond laser plasma interaction regime. *Matter and Radiation at Extremes*, 6(1):015901, 2021. doi: 10.1063/5.0026379. URL https://doi.org/10.1063/5.0026379.

W. D. Jones, H. J. Doucet, and J. M. Buzzi. *An Introduction to the Linear Theories and MEthods of Electrosatic Waves in Plasmas*. Plenum Press, 1st edition, 1985.

Seppo J. Karttunen. Ion fluctuation effects on the two-plasmon decay and stimulated raman scattering. *Phys. Rev. A*, 23:2006–2010, Apr 1981. doi: 10.1103/PhysRevA.23.2006. URL https://link.aps.org/doi/10.1103/PhysRevA.23.2006.

J. H. Kelly, A. Shvydky, J. A. Marozas, M. J. Guardalben, B. E. Kruschwitz, L. J. Waxer, C. Dorrer, E. Hill, A. V. Okishev, and J.-M. Di Nicola. Simulations of the propagation of multiple-fm smoothing by spectral dispersion on omega ep. *Proceedings of SPIE - The International Society for Optical Engineering*, 8602, 2 2013. doi: 10.1117/12.2003209. URL https://doi.org/10.1117/12.2003209.

O. Klimo, J. Psikal, V. T. Tikhonchuk, and S. Weber. Two-dimensional simulations of laser-plasma interaction and hot electron generation in the context of shock-ignition research. *Plasma Physics and Controlled Fusion*, 56(5), 2014. ISSN 13616587. doi: 10.1088/0741-3335/56/5/055010. URL https://doi.org/10.1088/0741-3335/56/5/055010.

J. L. Kline, D. S. Montgomery, L. Yin, D. F. DuBois, B. J. Albright, B. Bezzerides, J. A. Cobble, E. S. Dodd, D. F. DuBois, J. C. Fernández, R. P. Johnson, J. M. Kindel, H. A. Rose, H. X. Vu, and W. Daughton. Different kλ D regimes for nonlinear effects on Langmuir waves. *Physics of Plasmas*, 13(5), 2006. ISSN 1070664X. URL https://doi.org/10.1063/1.2178777.

David Kramer. Lawrence livermore claims a milestone in laser fusion. *Physics Today*, 2021. doi: 10.1063/PT.6.2.20210817a. URL https://physicstoday.scitation.org/do/10.1063/PT.6.2.20210817a/full/.

W. L. Kruer. *The Physics of Laser Plasma Interations*. Addison-Wesley Publishing Company, 1996.

W.L. Kruer. *The Physics of Laser Plasma Interactions*. CRC Press, 1st edition edition, 2003. ISBN 9781003003243. URL https://doi.org/10.1201/9781003003243.

W.L. Kruer, K.G. Estabook, and K.H. Sinz. Instability-generated laser reflection in plasmas. *Nuclear Fusion*, 13(6):952–955, December 1973. doi: 10.1088/0029-5515/13/6/024. URL https://doi.org/10.1088/0029-5515/13/6/024.

L. Landau. On the vibrations of the electronic plasma. *Journal of Physics*, X:445–460, 1946.

R. Lee, B. J. Winjum, S. J. Spencer, F. S. Tsung, W. B. Mori, and S. Bolanos. Effect of small normalized magnetic fields on rescatter of SRS in the kinetic regime. In *APS Division of Plasma Physics Meeting Abstracts*, volume 2021 of *APS Meeting Abstracts*, page NP11.148, 2021.

R. H. Lehmberg, M. F. Wolford, J. L. Weaver, D. Kehne, S. P. Obenschain, D. Eimerl, and J. P. Palastro. Stimulated rotational raman scattering of arbitrarily polarized broadband light. *Phys. Rev. A*, 102:063530, Dec 2020. doi: 10.1103/PhysRevA.102.063530. URL https://link.aps.org/doi/10.1103/PhysRevA.102.063530.

John Lindl, Otto Landen, John Edwards, and Ed Moses. Review of the national ignition campaign 2009-2012. *Physics of Plasmas*, 21(2):020501, 2014. doi: 10.1063/1.4865400. URL https://doi.org/10.1063/1.4865400.

C. S. Liu and Marshall N. Rosenbluth. Parametric decay of electromagnetic waves into two plasmons and its consequences. *Physics of Fluids*, 19(7):967–971, 1976. ISSN 10706631. doi: 10.1063/1.861591.

C S Liu and V K Tripathi. *Interaction of Electromagnetic Waves with Electron Beams and Plasmas*. World Scientific, 1994. doi: 10.1142/2189. URL https://www.worldscientific.com/doi/abs/10.1142/2189.

C. S. Liu, Marshall N. Rosenbluth, and Roscoe B. White. Raman and Brillouin scattering of electromagnetic waves in inhomogeneous plasmas. *Physics of Fluids*, 17(6):1211–1219, 1974. ISSN 10706631. doi: 10.1063/1.1694867. URL https://doi.org/10.1063/1.1694867.

H. H. Ma, X. F. Li, S. M. Weng, S. H. Yew, S. Kawata, P. Gibbon, Z. M. Sheng, and J. Zhang. Mitigating parametric instabilities in plasmas by sunlight-like lasers. *Matter and Radiation at Extremes*, 6(5):055902, 2021. doi: 10.1063/5.0054653. URL https://doi.org/10.1063/5.0054653.

T. H. Maiman. Stimulated optical radiation in ruby. *Nature*, 187(4736):493–494, August 1960. doi: 10.1038/187493a0. URL https://doi.org/10.1038/187493a0.

J.R. Marquès, P. Loiseau, J. Béard, A. Castan, B. Coleman, T. Gangolg, L. Lancia, O. Portugall, and J. Fuchs. Laboratory and numerical investigation of high-power laser propagation in magnetized plasmas of interest for icf physics. 42nd EPS Conference on Plasma Physics, 2015. URL ocs.ciemat.es/EPS2015PAP/pdf/P2.203.pdf.

D. S. Montgomery, R. J. Focia, H. A. Rose, D. A. Russell, J. A. Cobble, J. C. Fernández, and R. P. Johnson. Observation of stimulated electron-acoustic-wave scattering. *Phys. Rev. Lett.*, 87:155001, Sep 2001. doi: 10.1103/PhysRevLett.87.155001. URL https://link.aps.org/doi/10.1103/PhysRevLett.87.155001.

D. S. Montgomery, J. A. Cobble, J. C. Fernández, R. J. Focia, R. P. Johnson, N. Renard-Legalloudec, H. A. Rose, and D. A. Russell. Recent Trident single hot spot experiments: Evidence for kinetic effects, and observation of Langmuir decay instability cascade. *Physics of Plasmas*, 9(5):2311–2320, 2002. doi: 10.1063/1.1468857. URL https://doi.org/10.1063/1.1468857.

David S. Montgomery. Two decades of progress in understanding and control of laser plasma instabilities in indirect drive inertial fusion. *Physics of Plasmas*, 23(5):055601, 2016. doi: 10.1063/1.4946016. URL https://doi.org/10.1063/1.4946016.

G. J. Morales and T. M. O'Neil. Nonlinear frequency shift of an electron plasma wave. *Phys. Rev. Lett.*, 28:417–420, Feb 1972. doi: 10.1103/PhysRevLett.28.417. URL https://link.aps.org/doi/10.1103/PhysRevLett.28.417.

Jason F. Myatt, John G. Shaw, Russell K. Follett, Dana H. Edgell, Dustin H. Froula, John P. Palastro, and Valeri N. Goncharov. Lpse: A 3-d wave-based model of cross-beam energy transfer in laser-irradiated plasmas. *Journal of Computational Physics*, 399: 108916, 2019. ISSN 0021-9991. doi: https://doi.org/10.1016/j.jcp.2019.108916. URL https://www.sciencedirect.com/science/article/pii/S0021999119306217.

K. Nishikawa and C. S. Liu. *General formalism of parametric excitation*, volume 6, pages 3–81. John Wiley and Sons, 1976.

Kyoji Nishikawa. Parametric excitation of coupled waves i. general formulation. *Journal of the Physical Society of Japan*, 24(4):916–922, 1968. doi: 10.1143/JPSJ.24.916. URL https://doi.org/10.1143/JPSJ.24.916.

J. Nuckolls, L. Wood, A. Thiessen, and G. Zimmerman. Laser compression of matter to super-high densities: Thermonuclear (CTR) applications. *Nature*, 239(5368):139–142, September 1972. doi: 10.1038/239139a0. URL https://doi.org/10.1038/239139a0.

S. P. Obenschain, A. J. Schmitt, J. W. Bates, M. F. Wolford, M. C. Myers, M. W. McGeoch, M. Karasik, and J. L. Weaver. Direct drive with the argon fluoride laser as a path to high fusion gain with sub-megajoule laser energy. *Philosophical Transactions of the Royal Society A: Mathematical, Physical and Engineering Sciences*, 378(2184):20200031, 2020. doi: 10.1098/rsta.2020.0031. URL https://royalsocietypublishing.org/doi/abs/10.1098/rsta.2020.0031.

Stephen Obenschain, Robert Lehmberg, David Kehne, Frank Hegeler, Matthew Wolford, John Sethian, James Weaver, and Max Karasik. High-energy krypton fluoride lasers for inertial fusion. *Appl. Opt.*, 54(31):F103–F122, Nov 2015. doi: 10.1364/AO.54.00F103. URL http://ao.osa.org/abstract.cfm?URI=ao-54-31-F103.

T. O'Neil. Collisionless damping of nonlinear plasma oscillations. *Physics of Fluids*, 12(8), 1965. URL https://doi.org/10.1063/1.1761193.

L. J. Perkins, R. Betti, K. N. LaFortune, and W. H. Williams. Shock ignition: A new approach to high gain inertial confinement fusion on the national ignition facility. *Phys. Rev. Lett.*, 103: 045004, Jul 2009. doi: 10.1103/PhysRevLett.103.045004. URL https://link.aps.org/doi/10.1103/PhysRevLett.103.045004.

L. J. Perkins, D. D.-M Ho, B. G. Logan, G. B. Zimmerman, M. A. Rhodes, D. J. Strozzi, D. T. Blackfield, and S. A. Hawkins. The potential of imposed magnetic fields for enhancing ignition probability and fusion energy yield in indirect-drive inertial confinement fusion. *Physics of Plasmas*, 24(6):062708, 2017. doi: 10.1063/1.4985150. URL https://doi.org/10.1063/1.4985150.

M. G. Raymer, J. Mostowski, and J. L. Carlsten. Theory of stimulated Raman scattering with broad-band lasers. *Physical Review A*, 19(6):2304–2316, June 1979. ISSN 0556-2791. doi: 10.1103/PhysRevA.19.2304. URL https://link.aps.org/doi/10.1103/PhysRevA.19.2304.

Sean P. Regan, John A. Marozas, R. Stephen Craxton, John H. Kelly, William R. Donaldson, Paul A. Jaanimagi, Douglas Jacobs-Perkins, Robert L. Keck, Terrance J. Kessler, David D. Meyerhofer, T. Craig Sangster, Wolf Seka, Vladimir A. Smalyuk, Stanley Skupsky, and Jonathan D. Zuegel. Performance of 1-thz-bandwidth, two-dimensional smoothing by spectral dispersion and polarization smoothing of high-power, solid-state laser beams. *J. Opt. Soc. Am. B*, 22(5):998–1002, May 2005. doi: 10.1364/JOSAB.22.000998. URL http://josab.osa.org/abstract.cfm?URI=josab-22-5-998.

X Ribeyre, G Schurtz, M Lafon, S Galera, and S Weber. Shock ignition: an alternative scheme for HiPER. *Plasma Physics and Controlled Fusion*, 51(1):015013, dec 2009. URL https://iopscience.iop.org/article/10.1088/0741-3335/51/1/015013/meta.

C. Riconda, S. Weber, V. T. Tikhonchuk, and A. Héron. Kinetic simulations of stimulated Raman backscattering and related processes for the shock-ignition approach to inertial confinement fusion. *Physics of Plasmas*, 18(9), 2011. ISSN 1070664X. doi: 10.1063/1.3630937. URL https://doi.org/10.1063/1.3630937.

Harvey A. Rose. Trapped particle bounds on stimulated scatter in the large $k\lambda_D$ regime. *Physics of Plasmas*, 10(5):1468–1482, 2003. doi: 10.1063/1.1566029. URL https://doi.org/10.1063/1.1566029.

M. J. Rosenberg, A. A. Solodov, W. Seka, R. K. Follett, J. F. Myatt, A. V. Maximov, C. Ren, S. Cao, P. Michel, M. Hohenberger, J. P. Palastro, C. Goyon, T. Chapman, J. E. Ralph, J. D. Moody, R. H. H. Scott, K. Glize, and S. P. Regan. Stimulated raman scattering mechanisms and scaling behavior in planar direct-drive experiments at the national ignition facility. *Physics of Plasmas*, 27(4):042705, 2020. doi: 10.1063/1.5139226. URL https://doi.org/10.1063/1.5139226.

M. N. Rosenbluth. Parametric Instabilities in Inhomogeneous Media. *Physical Review Letters*, 29(9):565, 1972. doi: 10.1103/PhysRevLett.29.565. URL https://doi.org/10.1103/PhysRevLett.29.565.

C. Rousseaux, L. Gremillet, M. Casanova, P. Loiseau, M. Rabec Le Gloahec, S. D. Baton, F. Amiranoff, J. C. Adam, and A. Héron. Transient development of backward stimulated Raman and Brillouin scattering on a picosecond time scale measured by subpicosecond

thomson diagnostic. *Physical Review Letters*, 97(1):1–4, 2006. ISSN 10797114. URL https://doi.org/10.1103/PhysRevLett.108.145003.

A. L. Schawlow and C. H. Townes. Infrared and optical masers. *Phys. Rev.*, 112:1940–1949, Dec 1958. doi: 10.1103/PhysRev.112.1940. URL https://link.aps.org/doi/10.1103/PhysRev.112.1940.

R. H. H. Scott, K. Glize, L. Antonelli, M. Khan, W. Theobald, M. Wei, R. Betti, C. Stoeckl, A. G. Seaton, T. D. Arber, D. Barlow, T. Goffrey, K. Bennett, W. Garbett, S. Atzeni, A. Casner, D. Batani, C. Li, and N. Woolsey. Shock ignition laser-plasma interactions in ignition-scale plasmas. *Phys. Rev. Lett.*, 127:065001, Aug 2021. doi: 10.1103/PhysRevLett.127.065001. URL https://link.aps.org/doi/10.1103/PhysRevLett.127.065001.

A. G. Seaton. *Particle-in-cell simulations of laser-plasma instabilities in shock-ignition*. PhD thesis, University of Warwick, 2019.

A. G. Seaton and T. D. Arber. Laser-plasma instabilities in long scale-length plasmas relevant to shock-ignition. *Physics of Plasmas*, 27(8):082704, 2020. doi: 10.1063/5.0010920. URL https://doi.org/10.1063/5.0010920.

Stanley Skupsky, Terrance J Kessler, Robert W Short, Stephen Craxton, Samuel A Letzring, and John Soures. System for obtaining smooth laser beams where intensity variations are reduced by spectral dispersion of the laser light (ssd), 1 1991.

Steven W. Smith. *The Scientist and Engineer's Guide to Digital Signal Processing*. California Technical Publishing, USA, 1997. ISBN 0966017633. URL http://www.dspguide.com/pdfbook.htm.

S. J. Spencer, T. Goffrey, and T. D. Arber. Thresholds for inflationary stimulated Raman scattering driven by broadband lasers in shock-ignition. In *APS Division of Plasma Physics Meeting Abstracts*, volume 2020 of *APS Meeting Abstracts*, page TO08.008, January 2020.

S. J. Spencer, A. G. Seaton, T. Goffrey, and T. D. Arber. Inflationary stimulated Raman scattering in shock-ignition plasmas. *Physics of Plasmas*, 27(12):122705, 2020. doi: 10.1063/5.0022901. URL https://doi.org/10.1063/5.0022901.

D. J. Strozzi, E. A. Williams, A. B. Langdon, and A. Bers. Kinetic enhancement of raman backscatter, and electron acoustic thomson scatter. *Physics of Plasmas*, 14(1):013104, January 2007. doi: 10.1063/1.2431161. URL https://doi.org/10.1063/1.2431161.

J. J. Thomson and Jack I. Karush. Effects of finite-bandwidth driver on the parametric instability. *The Physics of Fluids*, 17(8):1608–1613, 1974. doi: 10.1063/1.1694940. URL https://aip.scitation.org/doi/abs/10.1063/1.1694940.

V.T. Tikhonchuk. Physics of laser plasma interaction and particle transport in the context of inertial confinement fusion. *Nuclear Fusion*, 59(3):032001, dec 2018. doi: 10.1088/1741-4326/aab21a. URL https://doi.org/10.1088/1741-4326/aab21a.

G. Tran, P. Loiseau, A. Fusaro, A. Héron, S. Hüller, L. Maëder, P.-E. Masson-Laborde, D. Penninckx, and G. Riazuelo. Fluid modeling of stimulated raman scattering accounting for trapped particles benchmarked against fully kinetic simulations. *Physics of Plasmas*, 27(12):122707, 2020. doi: 10.1063/5.0018669. URL https://doi.org/10.1063/5.0018669.

David Tskhakaya. *The Particle-in-Cell Method*, pages 161–189. Springer Berlin Heidelberg, Berlin, Heidelberg, 2008. ISBN 978-3-540-74686-7. doi: 10.1007/978-3-540-74686-7_6. URL https://doi.org/10.1007/978-3-540-74686-7_6.

H. X. Vu, D F Dubois, and B Bezzerides. Transient Enhancement and Detuning of Laser-Driven Parametric Instabilities by Particle Trapping. *Physical Review Letters*, (June), 2001. doi: 10.1103/PhysRevLett.86.4306. URL https://doi.org/10.1103/PhysRevLett.86.4306.

H. X. Vu, D. F. DuBois, and B. Bezzerides. Kinetic inflation of stimulated raman backscatter in regimes of high linear landau damping. *Physics of Plasmas*, 9(5):1745–1763, 2002. doi: 10.1063/1.1471235. URL https://doi.org/10.1063/1.1471235.

H. X. Vu, D. F. DuBois, and B. Bezzerides. Inflation threshold : A nonlinear trapping- induced threshold for the rapid onset of stimulated Raman scattering from a single laser speckle. *Physics of Plasmas*, 2007. doi: 10.1063/1.2426918. URL https://doi.org/10.1063/1.2426918.

A. Vyas, R. K. Singh, and R. P. Sharma. Effect of the magnetic field on coexisting stimulated raman and brillouin backscattering of an extraordinary mode. *Physics of Plasmas*, 23(1): 012107, 2016. doi: 10.1063/1.4939886. URL https://doi.org/10.1063/1.4939886.

Y. X. Wang, Q. Wang, C. Y. Zheng, Z. J. Liu, C. S. Liu, and X. T. He. Nonlinear transition from convective to absolute Raman instability with trapped electrons and inflationary growth of reflectivity. *Physics of Plasmas*, 25(10), 2018. ISSN 10897674. doi: 10.1063/1.5040095. URL https://doi.org/10.1063/1.5040095.

H. Wen, R. K. Follett, A. V. Maximov, D. H. Froula, F. S. Tsung, and J. P. Palastro. Suppressing the enhancement of stimulated raman scattering in inhomogeneous plasmas by tuning the modulation frequency of a broadband laser. *Physics of Plasmas*, 28(4):042109, 2021. doi: 10.1063/5.0036768. URL https://doi.org/10.1063/5.0036768.

E. A. Williams. Convective growth of parametrically unstable modes in inhomogeneous media. *Physics of Fluids B: Plasma Physics*, 3(6):1504–1506, 1991. doi: 10.1063/1.859719. URL https://doi.org/10.1063/1.859719.

B. J. Winjum, J. E. Fahlen, F. S. Tsung, and W. B. Mori. Anomalously hot electrons due to rescatter of stimulated raman scattering in the kinetic regime. *Phys. Rev. Lett.*, 110:165001, Apr 2013. doi: 10.1103/PhysRevLett.110.165001. URL https://link.aps.org/doi/10.1103/PhysRevLett.110.165001.

B. J. Winjum, F. S. Tsung, and W. B. Mori. Mitigation of stimulated Raman scattering in the kinetic regime by external magnetic fields. *Physical Review E*, 98(4):1–5, 2018. ISSN 24700053. doi: 10.1103/PhysRevE.98.043208. URL https://link.aps.org/doi/10.1103/PhysRevE.98.043208.

B. J. Winjum, A. Tableman, F. S. Tsung, and W. B. Mori. Interactions of laser speckles due to kinetic stimulated raman scattering. *Physics of Plasmas*, 26(11):112701, 2019. doi: 10.1063/1.5110513. URL https://doi.org/10.1063/1.5110513.

B. J. Winjum, R. Lee, S. J. Spencer, S. Bolanos, F. S. Tsung, and W. B. Mori. Parameter scan of stimulated Raman scattering in magnetic fields. In *APS Division of Plasma Physics Meeting Abstracts*, volume 2021 of *APS Meeting Abstracts*, page TO04.00007, 2021.

G. A. Wurden, S. C. Hsu, T. P. Intrator, T. C. Grabowski, J. H. Degnan, M. Domonkos, P. J. Turchi, E. M. Campbell, D. B. Sinars, M. C. Herrmann, R. Betti, B. S. Bauer, I. R. Lindemuth, R. E. Siemon, R. L. Miller, M. Laberge, and M. Delage. Magneto-inertial fusion. *Journal of Fusion Energy*, 35(1):69–77, November 2015. doi: 10.1007/s10894-015-0038-x. URL https://doi.org/10.1007/s10894-015-0038-x.

Kane Yee. Numerical solution of initial boundary value problems involving maxwell's equations in isotropic media. *IEEE Transactions on Antennas and Propagation*, 14(3):302–307, 1966. doi: 10.1109/TAP.1966.1138693.

L. Yin, W. Daughton, B. J. Albright, K. J. Bowers, D. S. Montgomery, J. L. Kline, J. C. Fernández, and Q. Roper. Nonlinear backward stimulated Raman scattering from electron beam acoustic modes in the kinetic regime. *Physics of Plasmas*, 13(7), 2006. ISSN 1070664X. URL https://doi.org/10.1063/1.2210929.

L. Yin, B. J. Albright, K. J. Bowers, W. Daughton, and H. A. Rose. Saturation of backward stimulated scattering of a laser beam in the kinetic regime. *Phys. Rev. Lett.*, 99:265004, Dec 2007. doi: 10.1103/PhysRevLett.99.265004. URL https://link.aps.org/doi/10.1103/PhysRevLett.99.265004.

L. Yin, B. J. Albright, K. J. Bowers, W. Daughton, and H. A. Rose. Saturation of backward stimulated scattering of laser in kinetic regime: Wavefront bowing, trapped particle modulational instability, and trapped particle self-focusing of plasma waves. *Physics of Plasmas*, 15 (1), 2008. ISSN 1070664X. URL https://doi.org/10.1063/1.2825663.

L. Yin, B. J. Albright, H. A. Rose, K. J. Bowers, B. Bergen, D. S. Montgomery, J. L. Kline, and J. C. Fernández. Onset and saturation of backward stimulated raman scattering of laser in trapping regime in three spatial dimensions. *Physics of Plasmas*, 16(11):113101, 2009. doi: 10.1063/1.3250928. URL https://doi.org/10.1063/1.3250928.

L. Yin, B. J. Albright, H. A. Rose, K. J. Bowers, B. Bergen, R. K. Kirkwood, D. E. Hinkel, A. B. Langdon, P. Michel, D. S. Montgomery, and J. L. Kline. Trapping induced nonlinear behavior of backward stimulated Raman scattering in multi-speckled laser beams. *Physics of Plasmas*, 19(5), 2012. ISSN 1070664X. doi: 10.1063/1.3694673. URL https://doi.org/10.1063/1.3694673.

L. Yin, B. J. Albright, H. A. Rose, D. S. Montgomery, J. L. Kline, R. K. Kirkwood, P. Michel, K. J. Bowers, and B. Bergen. Self-organized coherent bursts of stimulated raman scattering and speckle interaction in multi-speckled laser beams. *Physics of Plasmas*, 20(1):012702, 2013. doi: 10.1063/1.4774964. URL https://doi.org/10.1063/1.4774964.

Y. Zhao, L.-L. Yu, J. Zheng, S. Weng, C. Ren, C.-S. Liu, and Z.-M. Sheng. Effects of large laser bandwidth on stimulated raman scattering instability in underdense plasma. *Physics of Plasmas*, 22(5):052119, 2015. doi: 10.1063/1.4921659. URL https://aip.scitation.org/doi/abs/10.1063/1.4921659.

Y. Zhao, S. Weng, M. Chen, J. Zheng, H. Zhuo, C. Ren, Z. Sheng, and J. Zhang. Effective suppression of parametric instabilities with decoupled broadband lasers in plasma. *Physics of Plasmas*, 24(11):112102, 2017a. doi: 10.1063/1.5003420. URL https://doi.org/10.1063/1.5003420.

Y. Zhao, S. Weng, M. Chen, J. Zheng, H. Zhuo, and Z. Sheng. Stimulated raman scattering excited by incoherent light in plasma. *Matter and Radiation at Extremes*, 2(4):190–196, July 2017b. doi: 10.1016/j.mre.2017.06.001. URL https://aip.scitation.org/doi/abs/10.1016/j.mre.2017.06.001.

Yao Zhao, Suming Weng, Zhengming Sheng, and Jianqiang Zhu. Suppression of parametric instabilities in inhomogeneous plasma with multi-frequency light. *Plasma Physics and Controlled Fusion*, 61(11):115008, oct 2019. doi: 10.1088/1361-6587/ab4691. URL https://doi.org/10.1088/1361-6587/ab4691.

H. Y. Zhou, C. Z. Xiao, D. B. Zou, X. Z. Li, Y. Yin, F. Q. Shao, and H. B. Zhuo. Numerical study of bandwidth effect on stimulated raman backscattering in nonlinear regime. *Physics of Plasmas*, 25(6):062703, 2018. doi: 10.1063/1.5030153. URL https://doi.org/10.1063/1.5030153.

Y. Z. Zhou, C. Y. Zheng, Z. K. Liu, and L. H. Cao. Suppression of autoresonant stimulated raman scattering in transversely weakly magnetized plasmas. *Plasma Physics and Controlled Fusion*, 63(5):055015, 2021. doi: 10.1088/1361-6587/abf253. URL https://iopscience.iop.org/article/10.1088/1361-6587/abf253.